Alma Mater Studiorum - Università di Bologna

DOTTORATO DI RICERCA IN

GEOFISICA

Ciclo 34

Settore Concorsuale: 02/C1 - ASTRONOMIA, ASTROFISICA, FISICA DELLA TERRA E DEI PIANETI

Settore Scientifico Disciplinare: FIS/06 - FISICA PER IL SISTEMA TERRA E IL MEZZO CIRCUMTERRESTRE

THE ROLE OF THE ROCKY MOUNTAINS IN SHAPING THE ATMOSPHERIC MEAN STATE AND THE RESPONSE TO TROPICAL FORCING IN IDEALISED SIMULATIONS.

Presentata da: Emanuele Di Carlo

Coordinatore Dottorato

Nadia Pinardi

Supervisore

Susanna Corti

Co-supervisore

Silvana Di Sabatino

Esame finale anno 2022

Abstract

Understanding the natural and forced variability of the general circulation of the atmosphere and its drivers is one of the grand challenges in climate science. In particular, it is of paramount importance to understand to what extent the systematic error of global climate models affects the processes driving such variability. This is done by performing a set of simulations (ROCK experiments) with an intermediate complexity atmospheric model (SPEEDY), in which the Rocky Mountains orography is modified (increased or decreased) to influence the structure of the North Pacific jet stream. For each of these modified-orography experiments, the climatic response to idealized sea surface temperature (SST) anomalies of varying intensity in the El Niño Southern Oscillation (ENSO) region is studied. ROCK experiments are characterized by variations in the Pacific jet stream intensity whose extension encompasses the spread of the systematic error found in state-of-the-art climate models. When forced with ENSO-like idealised anomalies, they exhibit a non-negligible sensitivity in the response pattern over the Pacific North American region, indicating that a change/bias in the model mean state can affect the model response to ENSO. It is found that the classical Rossby wave train response generated by ENSO is more meridionally oriented when the Pacific jet stream is weaker, while it exhibits a more zonal structure when the jet is stronger. Rossby wave linear theory, used here to interpret the results, suggests that a stronger jet implies a stronger waveguide, which traps Rossby waves at a lower latitude, favouring a more zonally oriented propagation of the tropically induced Rossby waves. The shape of the dynamical response to ENSO, determined by changes in the intensity of the Pacific Jet, affects in turn the ENSO impacts on surface temperature and precipitation over Central and North America. Furthermore, a comparison of the SPEEDY results with Coupled Model Intercomparison Project (CMIP6) models behaviour suggests a wider applicability of the results to more resources-demanding, complete climate general circulation models (GCMs), opening up to future works focusing on the relationship between Pacific jet misrepresentation and response to external forcing in fully-fledged GCMs.

Contents

1 Introduction **13**

1.1 Objective and thesis structure 13
1.2 General circulation models 14
1.3 History of GCM 14
1.4 CMIP project 16
  1.4.1 AMIP 17
  1.4.2 CMIP history 17
  1.4.3 CMIP6 biases 18

2 Literature **21**

2.1 Orography introduction 21
  2.1.1 Orography and stationary waves 21
  2.1.2 Orography and mean zonal wind 22
2.2 ENSO introduction 22
  2.2.1 ENSO mechanism 23
  2.2.2 ENSO teleconnections 24
2.3 Rossby stationary waves 26

3 Model and methodology **29**

3.1 SPEEDY 29
  3.1.1 SPEEDY parameterizations 31
  3.1.2 Boundary conditions: 34
  3.1.3 SPEEDY climatology 34
  3.1.4 SPEEDY literature 35
3.2 Methodology 36
  3.2.1 Modified orography experiments (ROCK) 36
  3.2.2 Idealized tropical forcing (ENSO forcing) 38
3.3 Reanalysis and fully-fledged general circulation models 40
3.4 Metrics: Jet Indices 40
  3.4.1 Metrics: turning latitude 41

4 ROCK experiments **43**
4.1 Jet indices 43
4.1.1 Pacific Jet 43
4.1.2 Atlantic jet 44
4.1.3 SPEEDY vs CMIP6 44
4.2 The Climatology 47
4.2.1 The mean state 47
4.2.2 Rossby stationary wavenumber 61
4.3 Summary and discussion 62

5 ENSO sensitivity experiments **65**
5.1 ENSO results 65
5.1.1 ENSO response: teleconnection 67
5.2 ENSO response: impacts 70
5.2.1 ENSO response: Rossby waves propagation and the Rossby stationary wavenumber. 76
5.3 Summary and discussion 77

6 Conclusions **83**
6.1 Summary of the main conclusions 83
6.2 Future perspectives 84

List of Figures

2.1 ENSO mechanism. a) Neutral condition and b) El Niño condition. Figure from Meteorology today (Ahrens, D. 2009, pp 277[2]) 23

2.2 Schematic El Niño rossby wave train from Horel and Wallace (1981)[57]. . 25

2.3 Velocity field (dashed arrows) generated by vorticity conservation due to a sinusoidal displacement. The bold line represents the initial perturbation, the thin line is the position, at the time t, due to the velocity field. 27

3.1 Topography for the ROCK experiments (m). a) standard topography, b) meridional profile at 110W and c) longitudinal profile at 40N. 38

3.2 SPEEDY zonal wind at 850 hPa mean state for the winter season(DJF). Boxes indicate the regions where the PJ and AJ indices are calculated. 41

4.1 Winter season Pacific Jet indices. a) PJS index, b) PJL index, c) PJW index. 45

4.2 Winter season Atlantic Jet indices. a) AJS index, b) AJL index, c) AJW index 46

4.3 DJF PJL index vs PJS index. Orange diamonds are models from CMIP6, blue dots are ROCK experiments with reduced orography, red dots are ROCK experiments with increased orography, the black dot is the ROCK-0 experiment and the black star is ERA-Interim. 47

4.4 DJF AJL index vs AJS index. Orange diamonds are models from CMIP6, blue dots are ROCK experiments with reduced orography, red dots are ROCK experiments with increased orography, the black dot is the ROCK-0 experiment and the black star is ERA-Interim 48

4.5 DJF 850 hPa zonal wind (m/s). (a,c) Differences between the modified orography experiments (ROCK-60 and ROCK+60) and ROCK-0 (shading). (b) linear regression of the zonal wind from all ROCK experiments on the PJS index. Contours are the full field from the ROCK-0 (the step of the contours is 2.5 m/s). Stippling shows regions where the values are statistically significant (two-tailed t-test, α=0.05). 49

4.6 as Fig.4.5, but for 300 hPa zonal wind (m/s), the step of the contours is 10 m/s. 50

4.7 as Fig.4.5, but for 30 hPa zonal wind (m/s), the step of the contours is 10 m/s. 51

4.8 DJF zonal wind latitude-height cross-section (m/s). (a,c) Differences between the modified orography experiments (ROCK-60 and ROCK+60) and ROCK-0 (shading). (b) linear regression of the geopotential height from all ROCK experiments on the PJS index. Contours are the full field from the ROCK-0 (the step is 2.5 m/s). Stippling shows regions where the values are statistically significant (two-tailed t-test, α=0.05). 52

4.9 DJF 850 hPa meridional component of the wind (m/s). (a,c) Differences between the modified orography experiments (ROCK-60 and ROCK+60) and ROCK-0 (shading). (b) linear regression of the zonal wind from all ROCK experiments on the PJS index. Contours are the full field from the ROCK-0 (the step of the contour is 2.5 m/s). Stippling shows regions where the values are statistically significant (two-tailed t-test, α=0.05). 53

4.10 as Fig.4.9, but for meridional wind (m/s) at 300 hPa. 54

4.11 DJF 500 hPa geopotential height (m). (a,c) Differences between the modified orography experiments (ROCK-60 and ROCK+60) and ROCK-0 (shading). (b) linear regression of the zonal wind from all ROCK experiments on the PJS index. Contours are the full field from the ROCK-0 (the step of the contour is 100 m starting from 5100m). Stippling shows regions where the values are statistically significant (two-tailed t-test, α=0.05). 55

4.12 as Fig.4.11, but for 100 hPa geopotential height (m), the step of the contour is 500m starting from 15000m. 56

4.13 DJF total precipitation (mm/day). (a,c) Differences between the modified orography experiments (ROCK-60 and ROCK+60) and ROCK-0 (shading). (b) linear regression of the zonal wind from all ROCK experiments on the PJS index. Contours are the full field from the ROCK-0 (the step of the contour is 1 mm/day). Stippling shows regions where the values are statistically significant (two-tailed t-test, α=0.05). 57

4.14 DJF near surface air temperature (K). (a,c) Differences between the modified orography experiments (ROCK-60 and ROCK+60) and ROCK-0 (shading). (b) linear regression of the zonal wind from all ROCK experiments on the PJS index. Contours are the full field from the ROCK-0 (contours start from 250K and increase with a step of 10K). Stippling shows regions where the values are statistically significant (two-tailed t-test, α=0.05). 58

4.15 as Fig.4.14 but without the temperature signal associated with changes in orography (i.e., height change multiplied by the reference lapse rate). 58

4.16 DJF zonal air temperature cross section (K). (a,c) Differences between the modified orography experiments (ROCK-60 and ROCK+60) and ROCK-0 (shading). (b) linear regression of the geopotential height from all ROCK experiments on the PJS index. Contours are the full field from the ROCK-0 (the step is K). Stippling shows regions where the values are statistically significant (two-tailed t-test, α=0.05). 59

4.17 DJF eddy height (m) at 500hPa. (a,c) Differences between the modified orography experiments (ROCK-60 and ROCK+60) and ROCK-0 (shading). (b) linear regression of the geopotential height from all ROCK experiments on the PJS index. Contours are the full field from the ROCK-0 (the step is m/s). Stippling shows regions where the values are statistically significant (two-tailed t-test, α=0.05). 60

4.18 as Fig.4.17, but for eddy height at 100hPa (m). 61

4.19 DJF meridional profile of Rossby stationary wavenumber at 300 hPa. Ks is calculated by averaging the zonal wind at 300 hPa over a region between 170-110W. The black dashed line represents ERA-Interim, the black line is the ROCK-0 simulation, reds are ROCK experiments with increased orography, and blues ROCK experiments with reduced orography. 63

5.1 JFM response to El Niño in geopotential height at 500 hPa for ERA-Interim (a) and SPEEDY (NINO-0 minus ROCK-0,b). Contours are the respective climatological geopotential height and colours are the responses to El Niño. Stippling shows regions where the signals are statistically significant (two tailed t-test, α=0.05) 66

5.2 JFM response to La Niña in geopotential height at 500 hPa for ERA-Interim (a) and SPEEDY (NINA-0 minus ROCK-0, shadings) and ERA-Interim (contours). Contours are the climatological geopotential height and colours are the responses to El Niño. Stippling shows regions where the SPEEDY signals are statistically significant (two-tailed t-test, α=0.05). 67

5.3 JFM dipole response to ENSO in the geopotential height at 500 hPa for (a) for NINO-ROCK experiments (b) for NINOx2-ROCK experiments, (c) for NINA-ROCK experiments, and (d) for NINAx2-ROCK experiments. Only one contour for the North Pacific anomaly and only one for North America anomaly are drawn. Contours are chosen arbitrarily in order to highlight displacement of the anomaly. Dots show the positions of the maximum positive response and crosses the position of the minimum negative response. The value for the anomaly over the North American continent for the NINA experiments is about -9m, while the same for NINO reaches 15m. Similarly, NINAx2 shows a maximum signal of about -17m, while NINOx2 gets up to 30m. 68

5.4 JFM 500 hPa geopotential height response to NINO, NINA, NINOx2, and NINAx2 for all ROCK experiments. (a) NINO and NINOx2 latitude of the maximum of the response. (b) NINO and NINOx2 longitude of the maximum of the response. (c) NINO and NINOx2 geopotential height intensity of the maximum of the response. (d,e,f) are the same as (a,b,c) but for the minimum of the response in NINA and NINAx2 experiments. In all the panels the mean is represented by a dot and the standard deviation by the vertical bars. . . . 69

5.5 JFM 500 hPa geopotential height response to NINO, NINA, NINOx2, and NINAx2 for all ROCK experiments as a function of the PJS index calculated at 850 hPa. (a) NINO and NINOx2 latitude of the maximum of the response. (b) NINO and NINOx2 longitude of the maximum of the response. NINO and NINOx2 geopotential height intensity of the minimum of the response. (d,e,f) are the same as (a,b,c) but for the maximum of the response in NINA and NINAx2 experiments. In all the panels the mean is represented by a dot and the standard deviation by the bars. 70

5.6 JFM near surface air temperature response in NINO experiments (NINO - ROCK). (b) Linear regression between the near surface air temperature and the PJS index. (a,c) Two examples of the changes in the response to El Niño (NINO-60 and NINO+60). Stipplings show regions where the values are significant (FDR, $a_{global} = 0.20$, Wilks, 2006[123]). Contours show the near surface air temperature of the relative baseline experiments: (a) ROCK-60 , (b) ROCK-0 and (c) ROCK+60. 71

5.7 as Fig.5.6 but for the NINOx2 experiments. 71

5.8 as Fig.5.6 but for the NINA experiments. 72

5.9 as Fig.5.6 but for the NINAx2 experiments. 72

5.10 JFM total prexipitation response in NINO experiments (NINO - ROCK). (b) Linear regression between the total precipitation and the PJS index. (a,c) Two examples of the changes in the response to El Niño (NINO-60 and NINO+60). Stipplings show regions where the values are significant (FDR, $a_{global} = 0.20$, Wilks, 2006[123]). Contours show the total precipitation of the relative baseline experiments: (a) ROCK-60 , (b) ROCK-0 and (c) ROCK+60. 74
5.11 as Fig.5.10 but for NINOx2 experiments. 74
5.12 as Fig.5.10 but for NINA experiments. 75
5.13 as Fig.5.10 but for NINAx2 experiments. 75
5.14 DJF meridional profile of Rossby stationary wavenumber at 300 hPa. Ks is calculated by averaging the zonal wind at 300 hPa over a region between 170-110W. The black dashed line represents ERA-Interim, the black line is the ROCK-0 simulation, reds are ROCK experiments with increased orography, and blues ROCK experiments with reduced orography. Same as Fig.16.1. . 77
5.15 JFM meridional profile of Rossby stationary wavenumber at 300 hPa. Ks is calculated by averaging the zonal wind at 300 hPa over a region between 170-110W. The black dashed line represents ERA-Interim, the black line is the ROCK-0 simulation, reds are ROCK experiments with increased orography, and blues ROCK experiments with reduced orography. 78
5.16 as Fig.5.15 but for the NINOx2 experiments. 78
5.17 as Fig.5.15 but for the NINA experiments. 79
5.18 as Fig.5.15 but for the NINAx2 experiments. 79
5.19 Schematic representation of the impact of the orography on the ENSO response. 81

Chapter 1

Introduction

1.1 Objective and thesis structure

This work investigates the role of model bias on the response to an external forcing, in particular, the role of the Pacific jet stream on the propagation of El Niño southern Oscillation (ENSO) signals is explored. The orography on the Rocky Mountains region of an Earth system Model of Intermediate Complexity (EMIC) is changed in order to induce a modulation of the climatological mean state of the Pacific Ocean. In a second moment, for each orographic configuration, an idealized ENSO anomaly is imposed over the climatological Sea Surface Temperature (SST) to study the response of the model.[1]

The thesis is divided into six chapters:

- The first (the current one) is an introduction on Atmospheric General Circulation Models (AGCMs) and their biases.
- The second contains three short reviews respectively on the role of orography, the mechanism behind ENSO and the Rossby wave theory.
- Chapter 3 is an explanation of the model and methodology used in this work.
- Chapter 4 reports the results from experiments with different heights for the Rocky mountains, and
- chapter 5 contains the results from experiments forced with ENSO.
- Finally, in chapter 6 is a summary of the main conclusions.

---

[1] The experiments and their results are also contained in the paper submitted to "Climate Dynamics" entitled “ENSO teleconnections and atmospheric mean state in idealised simulations” by Di Carlo et al. (under second revision).

1.2 General circulation models

Atmospheric general circulation models (AGCMs) are powerful tools to investigate many phenomena of global circulation. From the first years of atmospheric numerical simulations to nowadays the complexity of AGCMs has increased relentlessly. The reasons are the continuous need for refinement and the request for more detailed and quantitatively accurate predictions.

The complexity of AGCMs can be divided into three different categories: Conceptual complexity, coupling complexity and numerical complexity. The conceptual complexity represents the intellectual effort, in the sense of physics, mathematics and computer codes, needed to understand their formulation. The coupling complexity takes into account the interaction between all the building blocks that constitute an AGCM. Finally, numerical complexity refers to the increasing spatial and temporal resolution of the models. Simulations have become every day more time and storage space consuming. Despite the improved ability of AGCMs in simulating and predicting weather and climate, these comprehensive very sophisticated models might not be the ideal tools to study physical processes. Their complexity (and computational cost) might in fact limit our capability to realize targeted experiments (long enough or with enough ensemble members) suitable to analyze and possibly explain the reason why fundamental features of atmospheric circulation develop. On the other hand simplified models (e.g. Held, 2005[52]) might depict a too idealized atmospheric circulation. A good compromise between extreme complexity and uttermost simplification is represented by the category of Earth System Models of Intermediate Complexity (EMIC, Claussen et al., 2002[32]). They are sufficiently realistic (because they include the "essential" complexity of atmospheric circulation), yet very convenient from a computational point of view (because their resolution is coarse and they can be installed and run on a desktop computer). These models are sufficiently accurate to be compared with observations, but less complex and computationally cheaper than fully-fledged GCMs. The model used in this study is an intermediate complexity Atmospheric General Circulation Model developed at the Abdus Salam International Center for Theoretical Physics (ICTP), known as SPEEDY (Simplified parameterization PrimitivE Equation DYnamic (Molteni 2003[81], Kucharski et al. 2006[68]).

1.3 History of GCM

The story of AGCM started in the early 20th century when Vilhelm Bjerknes developed seven “primitive equations” describing the behaviour of heat, air and moisture. In 1922, Fry Richardson used a simplified version of the primitive equations to develop the very first numerical system for weather predictions. The idea of Richardson was to divide the domain into a grid of cells, each with its own set of variables, and calculate the wind speed and direction from the difference in pressure between two adjacent cells. Despite Richardson planting the seed of modern numerical models, his first practical test failed after weeks of pencil work. Twenty years after the failure of Richardson, at the end of the second world war, Von Neuman found several similarities between his study on the effects of a nuclear explosion and the weather prediction, so he decided to invite Jule Charney to lead a brand new group of scientists to model the entire atmosphere. One of the most famous experiments and achievements of Charnay's group was the simulation of the effect of a mountain range on airflow. It was the first experiment exploring the role of orography on the mean flow (the first true orography experiment in an AGCM was in 1965 by Mintz et al.[80]). In 1949 the first three-dimensional model for a small region (North America) was developed (Charney, 1949[26]; Charney and Eliasses, 1949[27]). The forecast for only one day took almost one day of calculation. But, results, compared with the first observational data, demonstrated that Charney's model was able to catch several features of how the weather had actually developed (Charney et al.,1950[28]). The first "real" AGCM was the model made by Phillips in 1955 [87]. Phillips, inspired by some experiments with a rotating pan of water, developed simplified equations for a two-layer atmosphere. To reduce the mathematical complexity, he represented the hemisphere as a cylinder and he put the heating in the lower half. This very simple model was able to represent a plausible jet and a realistic-looking weather disturbance (Phillips, 1956[87]). Phillips's promising results inspired Von Neumann to put more effort into model development. He invited the Japanese meteorologist Manabe to join the lab. Manabe, with the help of Smagorinsky (the new director of the Weather Bureau), was able to implement a water cycle and radiative transport in his model. In 1965 their model was ready, it was a three dimensional model with the atmosphere divided into 9 levels. The model was missing ocean, land and orography, and the surface was simplified with a damping layer able to exchange moisture with the atmosphere. This new model was able to show a stratosphere and the formation of Hadley cells (Manabe, Smagorinsky and Strickler, 1965[75]; Smagorinsky, Manabe and Holloway,1965[103]). At the same time, another group composed by Mintz and Arakawa produced a model of the entire globe, with two layers and realistic geography, with rudimental orography, oceans and ice cover (Arakawa, 1970[8]; Mintz,1965[80]). During his work, Arakawa encountered difficulties in simulating the cloud cover, mainly because all the processes involved were on a scale, by far, lower than the model grid resolution, so he spent a good portion of his time in defining some useful "parameterizations" in order to tackle such processes. It was in this period that meteorologists found out the power of sharing information between several research groups.

In the second half of the 1960s GCM improved drastically thanks to the increasing effort in atmospheric measurement. The new data were useful to make better parameterizations up to the point of having good three-day forecasts. In the 1970s, the group led by Hansen developed a model that incorporated a parameterization for the reflection of sunlight by the snow. The implementation of this "albedo" parameterization drastically improved the quality

of the forecasts (Hansen et al.,1983[48]).
In the same period, the analysis of Keeling (1970[61]) led to an interesting discovery: the quantity of CO2 in the atmosphere was rising. This discovery tickled the fantasy of meteorologists that tried to simulate the effects of increasing levels of CO2. In 1975, Manabe and Wetherald published a paper describing the results of their "sensitivity" experiments. They showed that if the CO2 level is doubled, the global temperature would rise roughly 3.5°C. Moreover, the increased evaporation and precipitation lead to changes in the water content of the soil, making some regions drier and some others wetter. Finally, the warming was greater at the poles than in the rest of the globe, mainly because of the melting of the ice and the snow. But at that time, the results were taken not so seriously due to the scarce reliability of model predictions and the lack of consensus among the scientists. In 1979, after pressure from the media, the American National Academy of Science appointed a panel, chaired by Charney. This new study concluded that with a CO2 doubling in the atmosphere, the planet would warm up to three degrees (National Academy of Sciences,1979, pp.2,3[33]).
Manabe's opinion was that the only way to have a realistic model was to put together the atmosphere and the ocean. He collaborated with Bryan, an oceanographer who developed a numerical model for the oceanic circulation, and they built the first coupled model. They were well aware that the atmospheric wind would have developed more realistic oceanic currents, and the ocean sea-surface temperature and evaporation would help the circulation in the atmosphere. In 1969, they published a paper in which Bryan wrote that the experiment was a failure because the ocean was not able to reach equilibrium. Indeed the model was not able to describe the Earth climate, but the result resembled a real planet (Manabe and Bryan, 1969[74]). Years later, with the implementation of a rough but realistic Earth-like geography their model was able to represent many features of the real Earth. During the 1980s, the main modelling groups dedicated most of the time to refine the models in order to make better predictions and check how the models reacted to increasing levels of CO2. The increasing computational power and the implementation of the historical record of aerosol from volcanic explosion made possible the simulation of a realistic "transient response" of the models to increasing values of CO2 (Hansen et al.,1988[47]). Finally, in 1988 global warming was declared an imminent threat. From the early 1990s up to the current generation, the structure of AGCMs has not changed, but the complexity of parameterization and the spatial and temporal resolution has increased exponentially.

1.4 CMIP project

Since the birth of the first GCMs, scientists were well aware of the importance of sharing data and results from their different models. It was and it still is the fastest way to improve the quality of model and simulation. The first organized, multi center, intercomparison project was born in 1989, it was the Atmospheric Model Intercomparison Project (AMIP). AMIP is a standard experimental protocol for atmospheric models. In 1990 almost the entire international climate modeling community participated in this project. In the following years the AMIP protocol was incorporated as an integral part in the wider and more complex Coupled Model Intercomparison Project (CMIP, 1995).

1.4.1 AMIP

AMIP is a standard experimental protocol for global AGCMs initiated in 1989 under the auspices of the World Climate Research Programme (WCRP). It provides a community-based infrastructure in support of climate model diagnosis, validation, intercomparison, documentation and data access. This standard protocol enables a diverse community of scientists to analyze AGCMs in a systematic fashion, a process which serves to facilitate model improvement. The experimental design of AMIP simulations is simple; AGCMs are constrained by realistic sea surface temperature, sea ice from 1979 to near present, and prescribed CO2 concentration and solar constant. The simplified configuration enables scientists to focus on the atmospheric model without the complexity of ocean and ocean-atmosphere interactions.

1.4.2 CMIP history

The Coupled Model Intercomparison Project (CMIP) is the analog of the Atmospheric Model Intercomparison Project (AMIP) for coupled ocean-atmosphere general circulation models. The project was launched in 1995 with the purpose to provide a database of coupled GCM simulations under standardized boundary conditions, and attempt to diagnose model prefromances and investigate models' biases and models' uncertainty (i.e., why different models give different output in response to the same input).

The first phase of the CMIP, CMIP1, had three objectives: to document the mean response of the dynamically coupled climate system to CO2 doubling, to quantify the effects of flux adjustment on climate sensitivity in the coupled simulations and to document features of the simulated time-evolving climate system response to gradually increasing CO2 levels. The program included 18 models from 7 different countries. One year later, the CMIP2 added another experiment in which CO2 increases at the rate of 1% per year (Covey et al., 2003[34]). The main result of the first two CMIP phases was that coupled GCM control runs were nearly as accurate as observational uncertainty. Finally, the CO2 increasing scenarios had different outcomes depending on the model, but the range of model-simulated global mean warming, however, was less than the factor of 3 (1.5 - 4.5°C), the uncertainty commonly cited for equilibrium warming under doubled CO2 (Hansen et al. 1984[48], 1985[47]; Wigley and Schlesinger 1985[122], Covey et al., 2003[34]). The phase 3 of CMIP was carried out during the two years 2005 and 2006. It had 12 different experimental designs in order to explore the past, current and future climate in the most advanced generation of GCMs (for the time). In September 2008, the Working Group on Coupled Modelling (WGCM) decided to promote the phase 5 of CIMP (CMIP5). The program was to provide a framework for coordinated climate change experiments. The aims of simulation were to evaluate how realistically the models simulate the recent past, provide projection for the future on a near term and long term time scales and to understand the factors responsible for differences in model projections. All the experiments were divided in three groups: Decadal Hindcasts and Predictions simulation, long-term simulations and atmosphere only simulations. 20 coupled models from all over the world participated to the project, they were fully-fledged GCM comprehensive of: atmosphere, ocean, sea ice and land-vegetation. The phase lasted five years and a summary of the results was published in the Intergovernmental Panel on Climate Change (IPCC) fifth assessment report (AR5)(Climate Change 2013 – The Physical Science Basis). The most recent coupled model intercomparison project is the CMIP6 (Eyring et al., 2016[42]). It contains 23 experiments covering past, present, and future climate. Among them there are the "classical" Diagnostic, Evaluation and Characterization of Klima experiments (DECK), standard experiments carried out from CMIP2 onward and constituting the core of the CMIP project. These are the control experiment, the AMIP, abrupt increase of CO2 (4x the CO2), and the increase of 1% per year of CO2. The aim of CMIP6 was to give more insight for several scientific questions with a major effort in understanding how the Earth responds to forcings, how future climate can be assessed given internal climate variability, predictability, and uncertainties, and, finally, what are the origins and consequences of systematic model biases. More information on CMIP can be found on the WCRP web page `https://www.wcrp-climate.org/wgcm-cmip`.

1.4.3 CMIP6 biases

One of the main aims of the CMIP experiment is understanding the reasons behind the biases of state-of-the-art models. Despite the high complexity and the everyday increasing spatial and temporal resolution, modern GCM are affected by large bises in the mean state. Understanding the "sources" of these biases and how they affect the simulation of forcing scenarios is of extreme importance. Principal biases are found in the sea surface temperature, sea level pressure (SLP), and zonal wind (Shaffrey et al., 2009[100], Keeley et al., 2012[60]).

In the Atlantic Ocean the larger bias consists in an underestimation of the equatorial Atlantic cold tongue with an SST that is too warm in the eastern Atlantic. At the same time, the western equatorial Atlantic is affected by a cold bias. These two biases make an equatorial

SST gradient, from east to west, that is the opposite of the observed gradient (Richter et al.,2014[89]). The Bjerknes feedback (Bjerknes, 1969[13]) links the SST with the zonal wind resulting in weaker Trades and a westerly wind bias over the equatorial region. Outside of the equator, the SST shows a cold bias in the region south of Greenland (Randall et al. 2007[88]). The bias in midlatitudes SST is generally associated with a too zonal representation of the Gulf stream and the North Atlantic Current in the models (Eden et al., 2004[39]). The SLP shows a dipole bias pattern, very similar to the North Atlantic Oscillation, with a high pressure center over the Azores and a low pressure center over Iceland (Keeley et al., 2012[60]). The zonal wind at 850 hPa also exhibits a positive bias, with westerlies too strong and following a too zonal path crossing the Atlantic Ocean (Hannachi et al., 2013[46]). Models are able to represent the Atlantic jet seasonality, but they do not catch the trimodal structure observed by Woollings (2010[125]). The errors in the zonal wind are reflected into both the blocking frequency, that shows a negative bias with fewer blocking event when compared with observations (Cheung and Zhou 2015[30]; Anstey et al. 2013[7]) and a too zonal storm track that is placed over central Europe rather than over Scandinavia (Ulbrich et al., 2009[111]).

In the Pacific Ocean, the storm track is too strong on both its northeastern and northwestern flanks (Harvey et al., 2020[50]) and the jet stream has an equatorward bias (Ulbrich et al., 2009[111]). The SST bias in the Pacific Ocean is of great importance because it is able to alter the El Niño Southern Oscillation (ENSO) signal (Manganello and Huang, 2009[77], See chapter 3 for a short ENSO review). Usually CMIP models show a cold SST bias in a large region of the tropical pacific (10-40N,130E-120W).

The reasons behind model biases are still not well understood. Usually, atmospheric biases are associated with the low model resolution (e.g., Zappa et al., 2013[126]), the representation of orography (e.g., Berckmans et al., 2013[12]) and SST biases (Keeley et al., 2012[60]). Regarding the model resolution, CMIP6 models proved to have smaller biases and higher resolution when compared with CMIP5 models. But in models of the same phase there is a large spread in model resolution. Some models with a coarse resolution have very little biases and some models with high resolution show larger biases, the reason is that sub grid parameterizations are also relevant in generating biases (Sandu et al., 2019[95]) and not only the model resolution. Finally, it is difficult to assess an order of influence between SST bias and atmospheric bias. Bias in SSTs affect the atmospheric circulation, but the opposite is true as well (Keeley et al., 2012[60]).

Chapter 2

Literature

This chapter contains a short review of the basic concepts used as fundament for this work: orography, El Niño southern oscillation and Rossby waves.

2.1 Orography introduction

Orography plays a relevant role on the Earth climate, it has a large impact on stationary waves, large-scale circulation (Charney and Eliassen 1949[26]; Bolin 1950[16]), surface temperature (Seager et al. 2002[97]) and precipitation (Broccoli and Manabe 1992[22]; Wills and Schneider 2015[124]). The principal mountain chains able to influence the atmospheric flow are the Rocky Mountains(Brayshaw et al.,2009[21]), the Tibetan Plateau (Held et al. 2002[54]) and the Mongolian Plateau (White et al. 2017[119],2018[120]).

2.1.1 Orography and stationary waves

Stationary waves are wave-like features of the atmosphere that manifest at planetary scale. In the northern hemisphere, stationary waves are so relevant, and have a well defined structure that they have been given names: the Aleutian low, the Icelandic low, and the Siberian high. Another, weaker, signature of stationary waves is the Rocky ridge over the Rocky Mountains. Stationary waves are forced by orography and land-sea temperature contrast (Manabe and Tapestra 1974[76]). Strong SST gradients are also able to generate Rossby waves.

Orography represents a barrier for the mean flow and this is the main reason for the generation of Rossby waves; but, it also influences the diabatic heating, and, consequently, the stationary waves indirectly. This makes it difficult to disentangle the relative effects of 'orographic' and 'thermal' forcings to the stationary waves. The contribution of orography to the total amplitude of stationary waves is about 30% (Valdes and Hoskins 1989[112], Chang 2009[25]).

Some works explored the role of orographyby comparing control experiments with a standard representation of the orography with sensitivity experiments in which orography is "”flattened". It was found that, in the troposphere, stationary waves induced by orography have the same intensity of the waves generated by the land-sea contrast (White et al., 2018[120]). On the other hand, in the stratosphere the contribution of the orography is dominant (White et al., 2018[120]). The vertical structure of the orographic stationary waves show a neat difference between the surface and the upper levels. Near the surface, the presence of orography largely affects the stationary wave pattern. Stationary waves change intensity (weaker stationary waves) and wavenumber (higher) from experiment with orography to experiments without the orography (White et al., 2021[121]). While at upper levels, orography modulates the intensity of the baseline stationary waves, but their phase and shape is not affected. This suggests a constructive interference between the orographically forced stationary waves and the stationary waves due to land-sea contrast and SST gradients (Held, 1983[51]; Held et al., 2002[54]; Chang, 2009[25]; White et al., 2021[121]).

2.1.2 Orography and mean zonal wind

The two Hemispheres, Northern and Southern, have similar zonal mean zonal wind ($\overline{U}$) structure in the troposphere. This feature suggest, in former works, a weak effect of the orography on the zonal wind (Manabe and Terpstra, 1974[76]; Held et al., 2002[54]). Conversely, the stratosphere shows an asymmetry between the two hemispheres, and this is a consequence of the differences in the activity of planetary waves due to the orography and the land-sea contrast (Waugh and Polvani, 2010[118]; White et al.,2018[120]). Orography also affects the mean flow through the interactions between orographically generated stationary waves and the flow itself (Eliassen and Palm, 1961[41]; Charney and Drazin,1961[29]).

The principal effect of orography in the mean flow is a reduction of the zonal mean zonal wind both in troposphere and stratosphere. Experiments performed with a model in which the orography is removed completely, show that, despite the weak effect at lower latitudes, from 40N/S the effect of orography on the zonal wind is relevant. The northern hemisphere orography reduces the zonal wind by 50% near the surface, up to 80% in the stratosphere. Due to the limited continentality and very few mountain chains, the Southern Hemisphere is subject to a (smaller) reduction of about 10% (White et al., 2018[120]).

2.2 ENSO introduction

One of the main drivers of both tropical and extratropical variability is the El Niño-Southern Oscillation (ENSO) (Philander 1990[85], Wang 2017[117]), which generates global teleconnections in both the atmosphere and the ocean. ENSO is a quasi-periodic, coupled ocean-atmosphere phenomenon characterized by fluctuations of the sea surface temperature

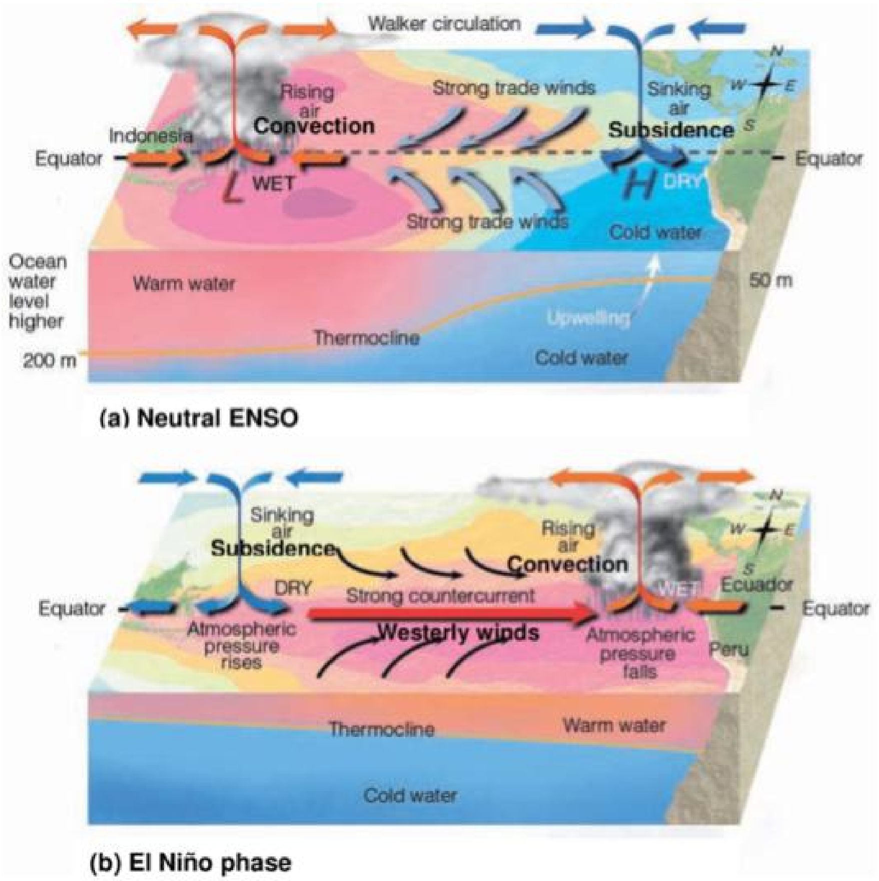
Walker circulation
Rising air
Convection
Strong trade winds
Sinking air
Subsidence
Indonesia
Equator
WET
L
H
DRY
Strong trade winds
Cold water
Ocean water level higher
Warm water
50 m
Upwelling
Thermocline
200 m
Cold water
(a) Neutral ENSO
Sinking air
Subsidence
Rising air
Convection
DRY
Strong countercurrent
WET
Ecuador
Equator
Atmospheric pressure rises
Westerly winds
Atmospheric pressure falls
Peru
Thermocline
Warm water
Cold water
(b) El Niño phase
N
W
E
S

Figure 2.1: ENSO mechanism. a) Neutral condition and b) El Niño condition. Figure from Meteorology today (Ahrens, D. 2009, pp 277[2])

(SST), thermocline depth, and sea level pressure (SLP) across the equatorial Pacific. The word quasi-periodic is used to describe the fluctuation between two extreme phases around a neutral state, which is not an oscillation in the strict sense.

2.2.1 ENSO mechanism

The state of the Tropical Pacific climate with respect to ENSO can be synthetically described as being in one of three conditions: Neutral, El Niño, and La Niña. El Niño is the positive phase of ENSO (associated with a warm SST anomaly) while La Niña is its negative phase (with a cold SST anomaly).

During the Neutral condition (Fig.2.1a), the trade winds blow from east to west, producing a surface westward ocean current and driving superficial water westward. This current creates high sea level and a deep thermocline (the water layer in which temperature changes drastically with depth and that divides the warmer upper mixed layer from the cool deep ocean) in the west, and low sea level and a shallow thermocline in the east. Due to the rotation of the Earth, the second water motion caused by the trades is the displacement of water out of the Equator, this motion causes upwelling (the rise of cool water from deeper levels to upper levels of the ocean). The combination of upwelling and the shallow thermocline produces the equatorial Pacific SST, which is characterized by a cold tongue in the east and a Warm Pool in the West Pacific (WPWP). This SST gradient is associated with a high SLP high on the east and a low SLP in the west. The low SLP in the west is associated with a rising motion of the air, convection and divergence at upper levels. In the eastern equatorial pacific, upper levels are subject to convergence and sinking air. The combination of rising air to the west and sinking air to the east generates, at upper levels, an eastward wind. The complex mechanism described above constitutes an east-west cell known as the Walker circulation. One of the main atmospheric consequences of ENSO is the rearrangement of the atmospheric Walker circulation which leads to a longitudinal shift of the associated convective rainfall patterns (Dai and Wingley 2000[36]).

During an El Niño event (fig.2.1b), a warm SST anomaly takes the place of the usually cold waters in the eastern tropical Pacific. The SST gradient weakens and the trades weakens as well (in strong events trades can also reverse). The atmospheric deep convection of the Walker circulation moves from the WPWP to the central Pacific and eastern tropical Pacific. The SLP pattern is modified and a low-pressure center prevails in the central tropical Pacific. The weaker easterlies reduce upwelling (this is the cause of the warming), and the associated waker SST gradient further weakens the trades, causing the Bjerknes feedback (Bjerknes, 1969[13]).

La Niña events are characterized by an opposite pattern of SST anomalies. The Neutral condition is reinforced, with stronger trades at the surface, increased convergence over the eastern tropical Pacific and reinforced divergence over the western Pacific. The wind-driven adjustment of the thermocline causes the oscillation between El Niño and La Niña events (Zebiak and Cane, 1987[127]).

The trigger mechanism of El Niño and La Niña events is still unclear (Timmermann et al, 2018[107]), the anomalies appear during summer and then they grow till reaching their maximum during the winter. The anomalies persist for periods longer than a year.

2.2.2 ENSO teleconnections

During an El Niño event, the warm SST anomaly, and the related anomalous convection in the eastern Tropical Pacific lead to an increased atmospheric low-level convergence and a corresponding upper-tropospheric divergence, generating an anomalous vorticity source in the tropics. These changes in the tropics influence the global atmospheric circulation via Kelvin and Rossby waves (Trenberth et al. 1998[108]).

The largest extratropical teleconnection generated by ENSO is a large-scale Rossby wave train(Hoskins and Karoli, 1981[59]; Horel and Wallace, 1981[57]). The Rossby wave train

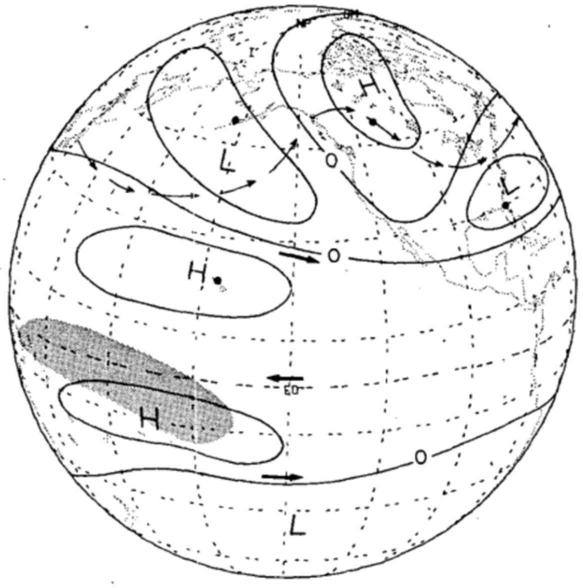

Figure 2.2: Schematic El Niño rossby wave train from Horel and Wallace (1981)[57].

structure consists of three centers of action in the upper tropospheric circulation(Fig.2.2. Starting from the Pacific Ocean, an El Niño event generates a cyclonic center of action that reinforces the climatological Aleutian Low. The second center of action is an anticyclonic center of action over the North American continent. The last one is another cyclonic center of action located on the edge of North America close to the Florida peninsula and the Atlantic Ocean. The position and intensity of these three centers of action affect the North Pacific jet and the Atlantic jet. During an El Niño event, the Pacific jet is stronger and shifted southward. The Atlantic jet is affected only in the entrance region. The position of the three centers of action and the associated changes in the zonal wind influence the weather and climate over Mexico, United States and Canada (Seager et al. 2005a[98],b[99]). During El Niño (La Niña) events, the southern part of North America is usually colder (warmer) and wetter (dryer), while the north-western part is mostly warmer (colder) and dryer (wetter). The Rossby wave train generated by ENSO starts to develop with the SST anomaly, it is fully established in January and persists until spring (Bladé et al. 2008[15], King et al. 2018[64]).

There is an ongoing debate regarding the connection between ENSO and the Pacific North American pattern (PNA). PNA is a characteristic pattern of the Northern Hemisphere internal variability, that includes four main centers of action observed in the 200hPa geopotential height (Wallace and Gutzler 1981[115]) and has significant influence on temperature and precipitation over North America (Gershunov and Cayan 2003[45]). Some authors argue that ENSO can only amplify internal variability and cannot generate new patterns (Molteni et al 1993[82], Lau 1997[71], Blade 1999[14], Palmer 1999[86]). Straus and Shukla (2002[104]), on the other hand, suggest that the external forcing (i.e., ENSO) can lead to patterns that are different from those typical of the internal variability. Lopez and Kirtman (2019[73]) found that ENSO produces response patterns over North America which are different from

PNA in the same region. Considering the limited observational record, the ENSO response is difficult to disentangle from internal atmospheric variability patterns.

2.3 Rossby stationary waves

The above-described ENSO teleconnection can be explained in terms of the linear theory of Rossby wave propagation. Rossby waves are planetary-scale waves that propagate westward with respect to the time-averaged background flow so that they can become stationary if the mean westerly flow presents the opportune conditions; they are capable of transferring energy and momentum across large distances and giving rise to teleconnection patterns (Hoskins and Karoli 1981[59]). Rossby waves can be generated by diabatic heating, a condition which typically occurs in areas of deep convection at tropical latitudes, and by orography. Consequently, anomalous Rossby waves can be produced following the onset of ENSO.

The way Rossby waves propagate in a slowly varying flow is well understood and the conservation of potential vorticity can be used to simplify the notion of Rossby stationary waves. Potential vorticity (PV) combines small scale properties, as the small-scale spin of elements of the fluid, and large scale environmental properties as the spin of the Earth. If friction, heat sources and small scale turbulence are neglected, the equation describing the conservation of PV is the following:

$$\frac{Dq}{Dt} = 0 \; where \; q = \frac{f+\zeta}{h} \tag{2.1}$$

q is the PV, f is the Coriolis frequency (eq2.2, where Ω is the Earth's rotation rate and ϕ is the latitude).

$$f = 2\Omega\cos\phi \tag{2.2}$$

ζ is the relative vorticity, it is twice the average rate of spin of fluid elements and h is the thickness of the fluid. When a fluid element moves north or south, it may trade off its small-scale spin (ζ) for its large scale spin (f). Fixing $\zeta = 0$ at t_0 and calling ∂y the meridional departure from the starting latitude

$$(\zeta + f_{t_1}) = f_0 \tag{2.3}$$

or better

$$\zeta_{t_1} = f_0 - f_{t_1} \tag{2.4}$$

In the case of a fluid with a constant thickness h, it is possible to use the 'beta plane' approximation. The spherical Earth can be approximated, locally, as a plane tangent to it.

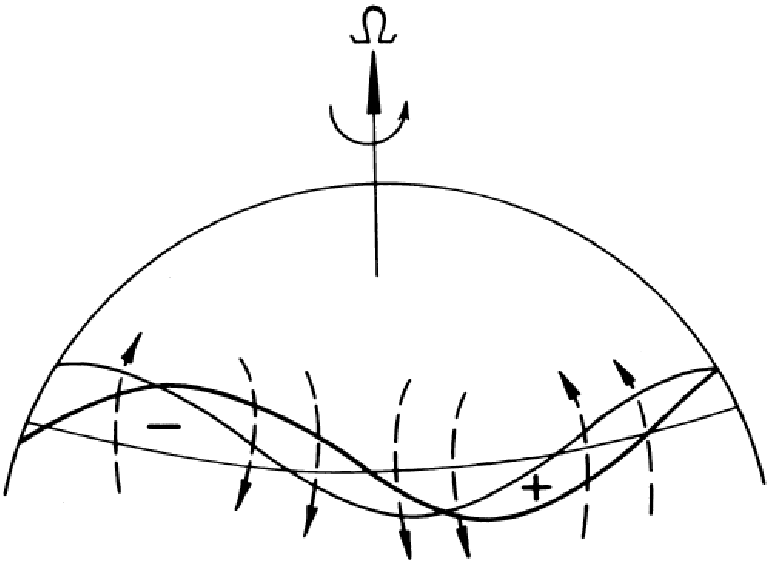

Figure 2.3: Velocity field (dashed arrows) generated by vorticity conservation due to a sinusoidal displacement. The bold line represents the initial perturbation, the thin line is the position, at the time t, due to the velocity field.

With this approximation, the Coriolis parameter can be written as

$$f = 2\Omega \sin\phi = f_0 + \beta \partial y \tag{2.5}$$

β is the following

$$\beta = \frac{df}{dy} = \frac{2\Omega\cos\phi}{a} \tag{2.6}$$

where a is the Earth's radius. In the case of a fluid at rest (without the east-west mean wind), and a meridional sinusoidal perturbation like

$$\partial y = d \sin[k(x - ct)] \tag{2.7}$$

where d is is the maximum northward displacement. The speed is

$$v = \frac{D(\partial y)}{Dt} = -kcd\cos[k(x - ct)] \tag{2.8}$$

and the relative vorticity is

$$\zeta = \frac{\partial v}{\partial x} = k^2 cd \sin[k(x - ct)] \tag{2.9}$$

Substitution for y and ζ in 2.4 leads to

$$k^2 dc \sin[k(x - ct)] = -\beta d \sin[k(x - ct)]. \tag{2.10}$$

The former can be rewritten as

$$c = -\frac{\beta}{k^2} \tag{2.11}$$

and the dispersion relation for Rossby waves is

$$\omega = -\frac{\beta}{\mathbf{k}} \tag{2.12}$$

where ω is the frequency and $\mathbf{k}$ the wavenumber (which is 2π divided by the wavelength). For Rossby waves, the restoring force, driving the acceleration of the wind, is the north-south pressure gradient. From Figure 2.3, an air mass moving northward in a standing wave pattern and conserving the PV, has to develop a negative relative vorticity (ζ), as higher latitudes are characterized by lower values of f. The associated anticyclonic spin matches the northward velocity west of the air parcel and the southward velocity to its east and the result is an enforcement of the basic wave pattern. If the wave propagates along an arbitrary direction, the term $\mathbf{k}$ in the dispersion equation can be divided in its two components k (east-west) and l (north-south). Consequently, the dispersion relation can be written as

$$\omega = \frac{-\beta k}{k^2+l^2} = \frac{-\beta \cos\alpha}{|\mathbf{k}|} \tag{2.13}$$

where α is the direction of k with respect to the east.
In the case of a background flow with an east-west wind U, w can be replaced with $-kU$ giving the following dispersion relation

$$kU = \frac{k\beta}{k^2+l^2} \tag{2.14}$$

or, by taking the square root, multiplying by 2π and and arranging the terms

$$\frac{2\pi}{\sqrt{k^2+l^2}} = 2\pi\sqrt{\frac{U}{\beta}} \tag{2.15}$$

This equation shows that faster winds make longer waves and regions with U<0 prevents the formation of Rossby waves. By considering that the group velocity has magnitude $\beta/|\mathbf{k}|^2$, in the case of standing waves, it is equal to U.
Finally, in the general situation of propagating waves (not stationary waves) on a westerly wind, the dispersion relation is:

$$\omega = Uk - \beta\frac{k}{k^2+l^2} \tag{2.16}$$

with an east-west phase speed

$$c = U - \frac{\beta}{k^2+l^2} \tag{2.17}$$

This is Carl-Gustav Rossby’s ‘trough’ formula.

Chapter 3

Model and methodology

In the last decades, a hierarchy of different GCMs has been developed to tackle a wide variety of scientific questions. Starting from the second half of the '80s, the complexity of GCM has dramatically increased. This has been associated with an increase in computational costs. For academic purposes, however, state-of-the-art GCMs can be too expensive, and here Earth System Models of Intermediate Complexity (EMIC, Claussen, et al. 2002[32]) can come into play. These models are sufficiently accurate to be compared with observations, but less complex and much computationally cheaper than fully-fledged GCMs.

The model used in this study is an intermediate complexity Atmospheric General Circulation known as SPEEDY.

3.1 SPEEDY

SPEEDY (Simplified parameterization PrimitivE Equation DYnamic, Molteni 2003[81], Bracco et al. 2004[19], Kucharski et al. 2006[69]) is an intermediate complexity Atmospheric General Circulation Model developed at the Abdus Salam International Center for Theoretical Physics (ICTP).

The SPEEDY model uses the Held and Suarez hydrostatic spectral dynamical core (Held and Suarez 1994[53]) developed at the Geophysical Fluid Dynamics Laboratory. The model is a hydrostatic, σ- coordinate, spectral transform model expressed in the vorticity-divergence form derived by Bourke (1974[18]). The model treats the gravity waves semi-implicitly. The prognostic variables are vorticity, divergence, absolute temperature, the logarithm of surface pressure, and the specific humidity. A leapfrog scheme associated with a weak time filter integrates the model in time (Robert 1966[91]). The accuracy of the leapfrog integration is increased from the first order to the third order using an additional filter (RAW) introduced by Amezcua et al. (2011[6]). The horizontal hyper-diffusion of vorticity, divergence, temperature and humidity has the form of the fourth power of the Laplacian, applied on σsurfaces. To avoid spurious vertical diffusion of T and Q over steep topography, a corrective term that simulates diffusion on pressure surfaces is used.

SPEEDY can be set to work at different horizontal spectral resolutions; typical triangular spectral truncation numbers are 21, 30 or 47. The version in this work uses the T30 resolution (450 km at the equator) with a standard gaussian grid of 96 by 48 points and 8 vertical layers with boundaries (half levels) at σvalues of 0, 0.05, 0.14, 0.26, 0.42, 0.60, 0.77, 0.90 and 1. All the prognostic variables, apart from $log(p_s)$, are specified at sigma levels intermediate between the upper and lower boundaries (full levels). The top two layers give a representation of the stratosphere and the bottom layer a representation of the planetary boundary layer (PBL). The output data are given on pressure levels at 30, 100, 200, 300, 500, 700, 850, 925 hPa.

A set of parameterizations, based on the same basic principles used in more complex GCMs, but appropriately modified to suit a model with a coarse vertical resolution, takes care of processes such as cloud formation, large-scale condensation, surface fluxes of momentum and energy, vertical diffusion of heat and moisture, convection, short and longwave radiative transfer. All the parameterizations are run as independent modules, the exceptions are the surface fluxes that use the downward radiative flux at the surface as an input.

The model requires appropriate boundary conditions in order to determine the fluxes of momentum, heat and moisture at the surface and the flux of incoming solar radiation at the top of the atmosphere. At the surface, the boundary conditions are the topographic height, land-sea mask, and the climatological field of sea surface temperature (SST), sea ice fraction, soil temperature in the deep soil layer, moisture in the soil top layer and the root-zone layer, snow depth, bare-surface albedo (no snow and no sea ice) and the fraction of land-surface covered by vegetation. Apart from the last two fields that are used as annual mean values, all the other fields are specified as monthly means. To obtain the daily data, the monthly values are linearly interpolated.

The net surface albedo derives from the bare-surface albedo linearly combined with assigned values of snow albedo and sea-ice albedo. Sea-ice fraction and snow cover are used as weights for the calculation. The evaporation over land derives from the linear combination, weighted using the vegetation fraction, of soil top layer moisture and root-zone layer moisture.

All the climatological fields are the monthly averages of the corresponding data from the European Center for Medium-Range Weather Forecast' re-analysis (ECMWF, ERA Interim, Dee et al. 2011[37]) in the period 1979-2008. The incoming flux of solar radiation at the top of the atmosphere is computed daily from astronomical formulae (no daily cycle). Empirical, seasonally varying functions define the absorption of solar radiation by ozone in the stratosphere and the latitudinal variations of optical depth for solar radiation.

The SPEEDY model is computationally advantageous, so it can be integrated over centuries at a minor computational cost. The source code and the documentation of the current version of the model - including information on model development and subsequent releases, can be found at http://users.ictp.it/ kucharsk/speedy-net.html.

3.1.1 SPEEDY parameterizations

This section illustrates all the SPEEDY parameterizations.

Convection: the convection scheme is derived from the mass-flux scheme developed by Tiedke (1993[106]). The scheme describes the upward motion of saturated air from the PBL to a particular "top of convection" (TCN) level in the middle or upper troposphere and the large-scale downward motion. The entrainment is allowed in the lower troposphere above the PBL, and the detrainment is blocked except for the TCN layer. The condition for the activation of the convection scheme is the onset of an unstable region, this happens when the moist static energy (MSS = dry static energy + latent heat x saturation specific humidity) decreases with height and the humidity in both PBL and the layer above exceeds a threshold value. The TNC level is the highest tropospheric level for which the MMS is still decreasing with height. The condensation is calculated only in the TCN layer, where the upward fluxes are set to zero. The effect of smaller non-precipitation convective systems is represented by an additional diffusion of moisture between the PBL and other levels. The effect is activated when, for a certain level, the relative humidity falls below a threshold value.

Large-scale condensation: large-scale condensation is represented as a relaxation of humidity towards a reference value. In the troposphere, the condition is reached when relative humidity exceeds a threshold value that depends on sigma. In the troposphere, the precipitation flux due to large-scale condensation is the vertical integral of humidity tendencies with the opposite sign.

Clouds and short-wave radiation: the radiation scheme in SPEEDY is the most complex parameterization. Clouds exist in layers where the relative humidity and the specific humidity exceed their corresponding thresholds. The lower boundary of clouds is the interface between the lowest two model layers in which the previous conditions are satisfied. The top of the clouds is the upper boundary of the highest model layer in which the same conditions are satisfied. The cloud cover is a function of the total precipitation and relative humidity. If the top layer of precipitation is higher than the top layer of clouds, the top layer of clouds is set to the top layer of precipitation. At the top of PBL, Stratocumulus clouds are parameterized depending on the static stability and exist if the gradient of static energy exceeds a threshold value. After cloud properties are defined, the shortwave radiation is calculated. The incoming solar radiation is calculated from astronomical formulae. The absorption by ozone is defined as an idealized function that depends on the latitude and it is considered as absorbed by the first model layer. To consider the absorption due to upper non resolved stratospheric layers, a small latitudinally-dependent fraction of the incoming radiation is turned into outgoing longwave radiation. The downward radiation that remains after the subtraction of the ozone absorption is divided into two bands, the visible and the near-infrared. For both the bands and for each model layer, the downward propagation of shortwave radiation is computed defining transmissivities as functions of the daily-averaged zenith angle, layer depth, specific humidity, layer mass, and cloud properties. In the cloud top layer, the flux reflected by clouds is removed from the downward radiation. At the surface, another portion of downward radiation is removed to consider the reflection due to stratocumulus clouds. Lastly, at the surface, a climatological albedo is defined as a function of the seasonally varying field of sea ice and snow depth. The upward flux of shortwave radiation is modelled as the flux incident at the lower boundary of the model layer multiplied by the transmissivity. By considering that almost all the near-infrared radiation is absorbed during the downward propagation, the upward part is calculated only for the visible band.

Longwave radiation: the infrared spectrum is divided into four bands:

- the "infrared-window" between 8.5 and 11 μm (1);
- the CO2 band around 15 μm (2);
- the aggregation of regions with moderate absorption by water vapour (3);
- the aggregation of regions with strong absorption by water vapour (4).

The transmissivity is computed for each band and each model layer as a function of layer depth, humidity and cloud properties. The effect of clouds is treated as a strong reduction of transmissivity in the "infrared-window" band. Typically, the values of transmissivity (τ) for each band and in clear-sky conditions are such to have

$$\tau_{k,4}^{LR} < \tau_{k,2}^{LR} < \tau_{k,3}^{LR} < \tau_{k,1}^{LR} \tag{3.1}$$

At the tropics, near the surface, the transmissivity of band 3 is smaller than band 2. In the stratosphere, the CO2 band has the lowest transmissivity.
The downward flux at the upper boundary is set to zero and then, for each level and each band, the downward transmission and emission are computed. At the lower boundary, the black body emission from the Earth surface is multiplied for the surface emissivity and partitioned among the four bands. A small contribution coming from the longwave reflection is added. The upward propagation follows the same equation of the downward propagation, the only exception is the temperature of emission. When the transmissivity is close to zero, the upward and downward emissions are dependent on the temperature at the respective boundaries (upper and lower). When the transmissivity is large, upward and downward emissions approach each other depending on the temperature of the mid-layer. The last correction to the parameterization is the addition of a seasonally varying term in the longwave radiation flux emitted by the stratospheric layers. This term is needed because neither the water vapour nor the ozone is modelled in the stratosphere.

Surface fluxes of momentum and energy: surface fluxes are modelled using standard aerodynamic formulas (chapter 4 in Hartmann 1994[49]). By considering that the PBL is

represented by only one layer, it is not possible to approximate near-surface variables to the lowest model level. Also, PBL stability properties cannot be estimated as the gradients between two model layers. Therefore, near-surface atmospheric values of wind, temperature and humidity are obtained through extrapolations. The near-surface wind is proportional to the wind at the lowest level. Near-surface temperature is extrapolated considering a linear profile in $\log(\sigma)$ for values between the two lowest layers. The near-surface temperature is not allowed to be lower than the temperature of the lowest model layer. The relative humidity is set equal to the lowest-level value. The value for near-surface specific humidity is calculated starting from near-surface temperature and relative humidity. By using all the defined variables , the effective wind speed is obtained as a function of the wind zonal component, the wind meridional component, and a constant that represents the unresolved wind variability.
The water content in the soil top layer and the root layer are expressed by a single climatological index depending on the vegetation fraction and soil moisture value at field capacity (Viterbo and Beljiars 1995[114]). Once the appropriate variables are defined, surface stresses, sensible heat flux and evaporation are computed over the land surface and sea surface. The difference between land and sea is the drag coefficient used for the surface stresses. Over the land, the drag coefficient is a function of the topographic height, over the sea, the drag coefficient is constant.
SPEEDY uses a fractional land-sea mask, in all grid points where the land-fraction is less than one and greater than zero, surface fluxes are obtained as weighted averages of land and sea fluxes.

Skin temperature: skin temperature is derived from the surface energy balance. The skin layer has zero heat capacity (Viterbo and Beljaars 1995[114]). The energy balance is a non linear function of skin temperature, and to avoid time-consuming solutions like iterative solving methods, the function is linearised assuming small skin temperature adjustment with respect to the soil temperature. The error due to linearization is small.

Soil and sea ice temperature: for each soil layer the temperature is calculated using an extended force-restore method (Hirota et al 2002[56]). A similar method calculates the temperature for the sea ice, the only difference is the variation of sea ice thickness. The model calculated the temperature anomalies with respect to the climatology, and the final temperature is given by summing the anomaly to the climatological temperature.

Vertical diffusion: the vertical diffusion module is used for three different processes, shallow convection between the two lowest layers, slow diffusion of moisture in stable conditions, and a fast redistribution of dry static energy. The condition which activates the shallow convection is when the moist static energy in the second layer exceeds the saturation moist static energy of the lowest layer. The moist static energy is used instead of saturation moist static energy to prevent the activation of vertical diffusion in dry regions. In upper levels, the diffusion is activated when the vertical gradient of a variable is outside some reference bounds.

For the diffusion of moisture, the activation variable is the gradient of relative humidity with respect to sigma levels. For dry static energy, the variable is the same but with respect to geopotential.

3.1.2 Boundary conditions:

The model requires several boundary conditions to determine the surface fluxes and the incoming solar radiation at the top of the atmosphere. The surface requires the topographic height, the land-sea mask, sea surface temperature (SST), sea ice fraction, surface temperature in the soil top layer, moisture in the soil top layer and root-zone layer, snow depth, bare-surface albedo and the fraction of land-surface covered by vegetation. All the fields are specified as monthly means and are linearly interpolated to get daily values. The bare-surface albedo and the fraction of land-surface covered by vegetation are two exceptions; these two fields are given as annual-mean values. Boundary conditions are obtained from the 1979-2008 monthly climatology from the ERA-Interim reanalysis (Dee et al. 2011[37]).

3.1.3 SPEEDY climatology

The website http://users.ictp.it/ kucharsk/speedy-net.html provides the descriptions of the model version and a brief overview of the performance of the model in representing the mean climate and variability. A more exhaustive description of the model climatology can be found in Molteni 2003[81], Bracco 2004 [19], and Kucharski 2006 [68]. Here, a summary is reported.

The mean state

The comparison between SPEEDY and ERA data shows that the model reproduces to a good degree of accuracy the meridional temperature gradient with height, the cross-section of zonal-mean zonal wind, the global rainfall distribution, and the 500-hPa geopotential height. The temperature cross-section shows a good tropospheric thermal structure, with a reasonable inversion of the temperature gradient in the stratospheric layer. The systematic error of the model is characterized by a cold bias at 500 hPa in the midlatitude and polar region for both the hemispheres. Conversely, the upper troposphere shows a warm bias in the extratropics of the Northern Hemisphere. Overall, the SPEEDY model bias is comparable with biases from state-of-the-art GCM.

The tropospheric zonal wind vertical structure is realistic, the upper-tropospheric jet maximum has nearly the correct amplitude and position for both the hemispheres. The model also represents well the lower-troposphere easterly maximum. The main bias for the zonal wind is a northward shift of the jet structure. The wind field at 925 hPa shows a good agreement with the reanalysis. The largest difference is located over the North Atlantic. In the jet exit region, the westerlies are too strong and are associated with a zonal storm track that extends too far east. This is a typical error of GCMs. SPEEDY biases in the zonal wind are larger than state-of-the-art models.

With regards to the global rainfall distribution, the SPEEDY model reproduces all major features. In the tropics, the model has stronger precipitation over the Indian and West Pacific Oceans with respect to reanalysis, but the effect is reversed over South America and Africa.

The geopotential height at 500 hPa, in the North Hemisphere, shows an underestimation of the amplitude of stationary eddies. The amplitude of the stationary wave is about half of the reanalysis value.

The capability of SPEEDY in representing the global circulation is season dependent with results that are better during the Boreal Winter and worse during the Summer.

Variability

The SPEEDY model wintertime variability is reasonably good for, at least, three different time scales: the high-frequency, interannual low-frequency and interannual variability.

The high-frequency variability is represented by the standard deviations of departure of the instantaneous field from 5-day means. The model shows a good representation of the storm track regions over the northern oceans. The variability over the Pacific Ocean is underestimated on the eastern side of the ocean, while the variability in the western side is in good agreement with the observations. On the Atlantic Ocean, the variability is always underestimated. The representation of variability is worse in Europe, where the storm track has an incorrect intensity and orientation.

Moving to the intraseasonal low-frequency variability, represented as the deviation of the 5-day means from the running 60-day averages, the discrepancies between the model and the reanalysis are larger. Over both the Pacific and Atlantic oceans, the model low-frequency maxima are displaced southward of the observed location. In the Pacific Ocean, the underestimation is more pronounced in the eastern side of the basin.

The variability of seasonal means shows a good simulation of the position of the Atlantic maximum, while the pacific shows two separate maxima located at the eastern and western sides of the single maximum observed in the reanalysis. Also, for interannual variability, the intensity of the maxima is underestimated.

3.1.4 SPEEDY literature

Despite the limitations of an EMIC, especially true for the vertical resolution, and the simplified parameterizations, since its first release in 2003 the SPEEDY model has been used with satisfactory results for several aspects of the atmospheric climate. The literature regarding SPEEDY is flourishing and the model achieves capability that is on par with state-of-the-art models. For some aspects, the performance of state-of-the-art models can even be exceeded (Kucharski et al 2007[67]). Here are some of the main results. The SPEEDY model proved to have a good representation of the extratropical circulation trends and decadal changes (Kucharski et al. 2006[68]), extratropical planetary-scale variability modes (Molteni et al. 2011[83]), tropical-extratropical teleconnections between the western Pacific and the North Atlantic Oscillation (NAO) (Kucharski et al. 2007[67]), monsoon climate (Kucharski 2013[70]), tropical teleconnection patterns (Brimalala 2012[10]), ENSO teleconnections (Herceg-Bulić et al. 2012,[24]), and a minimal representation of troposphere-stratosphere interactions (Herceg-Bulić et al 2017[55], Ruggieri et al. 2017[93]). An updated and comprehensive list of publications involving SPEEDY can be found in http://users.ictp.it/ kucharsk/speedy-doc.html.

3.2 Methodology

This section illustrates the procedure followed to modify the bias (mean state/climatology) of the SPEEDY model. The control simulation and all the modified orography experiments are illustrated in the following sections.

3.2.1 Modified orography experiments (ROCK)

The chapter 2 has an overview of the role of orography in shaping and modulating the circulation at several levels of the atmosphere. Starting from the present knowledge on the effects of orography, a reasonable way to alter a model Mean State is the modulation of the model topography. A simple but effective approach is to change the orography over the Rocky Mountains region. Indeed, the Rocky Mountains play a relevant role in shaping and modulating the Northern Hemisphere climate (e.g., White et al, 2021[121]).The principal effects of the Rocky Mountains are the weakening of the wind and the storm track in the zonal mean, the strengthening of the stationary wave pattern, a southwest-northeast tilt of the tropospheric eddy-driven jet downstream of the mountains and an increase of baroclinicity in the downstream southward side of the mountains. Associated with the increase of baroclinicity, there is an increase in the strength of the storm track over the downstream basin (Atlantic Ocean) along a southwest-northeast axis. These effects are due to the peculiar topography of the Rocky Mountains, which generates a dipole with an anticyclone on the windward and poleward side of the mountain range (where the wind has to "go over" the mountain) and a cyclone on the leeward and equatorward side (where the flow is more effectively blocked so that it is partially diverted around the mountain) (Brayshaw et al, 2009[21]). These effects are also enhanced by the northwest-southeast elongation of the Rocky Mountains and their extension through the tropics (Brayshaw et al, 2009[21]). By modulating the height of the Rocky Mountains, it is possible to act on the way the circulation interacts with the orographic obstacle and, consequently, change the mean flow over both the Pacific and the Atlantic sectors.

Experiments setup: Control simulation (ROCK-0)

The baseline experiment is the SPEEDY model in the default configuration. The name of this experiment is ROCK-0. The names of the experiments represent the way the model orography is changed and the presence, or absence, of external forcing. In this specific case, the word "ROCK" indicates the absence of external forcings; moreover, the nomenclature makes explicit that the experiment is included in the modified orography group. The number 0 indicates the particular percentage of orographic change, in this particular case, it is no change (0%).

To reduce the model internal variability, the model sea ice and the land modules are switched off. The trade-off of this choice is that the interpretability of the effects of changes in the model increases (there are fewer interactions between modules and/or a decrease in possible non-linear effects) for a bit less accurate description of the climatology. Each experiment is 200 years long and the first year is discarded and considered as spinup time.

The SST and the Sea Ice Concentration (SIC) boundary conditions are obtained from the 1979-2008 monthly climatology from the European Centre for Medium-Range Weather Forecasts reanalysis (ERA-Interim; Dee et al. 2011[37]). Daily SST and SIC forcing data are obtained by linearly interpolating monthly mean values. The radiative parameters for shortwaves and CO2 are set to represent values of the last decades of the 20th century (King et al.,2010[65]). Model integration starts with a standard atmosphere at rest and in hydrostatic equilibrium.

Experiments setup: ROCK experiments

Twelve 200-year long simulations are performed with a set of modified orographies to obtain different mean states of the mid-latitude atmospheric circulation. The twelve modified orography simulations are characterized by an increased or decreased height of the Rocky Mountains in a box spanning 170W-90W and 10N-80N. The North American orography is referred to as Rocky Mountains because, due to its resolution, the SPEEDY model is unable to resolve smaller mountain chains as Sierra Nevada and the Cascades. The changes to the height of the Rocky mountains ranges from -60% to +60% (-60%, -50%, -40%, -30%, -20%, -10%, +10%, +20%, +30%, +40%, +50% and +60%). To avoid discontinuities in the orography field along the edge of the box, a nine grid point smoothing is applied at the borders of the domain. The names of the experiments follow the rules of the ROCK-0 experiment. The twelve simulations with changes in the height of the Rocky Mountains, together with the ROCK-0 control simulation, are hereafter named ROCK experiments. Figure3.1 shows the domain in which the Rocky Mountains are modified. Panel a is the topography of the

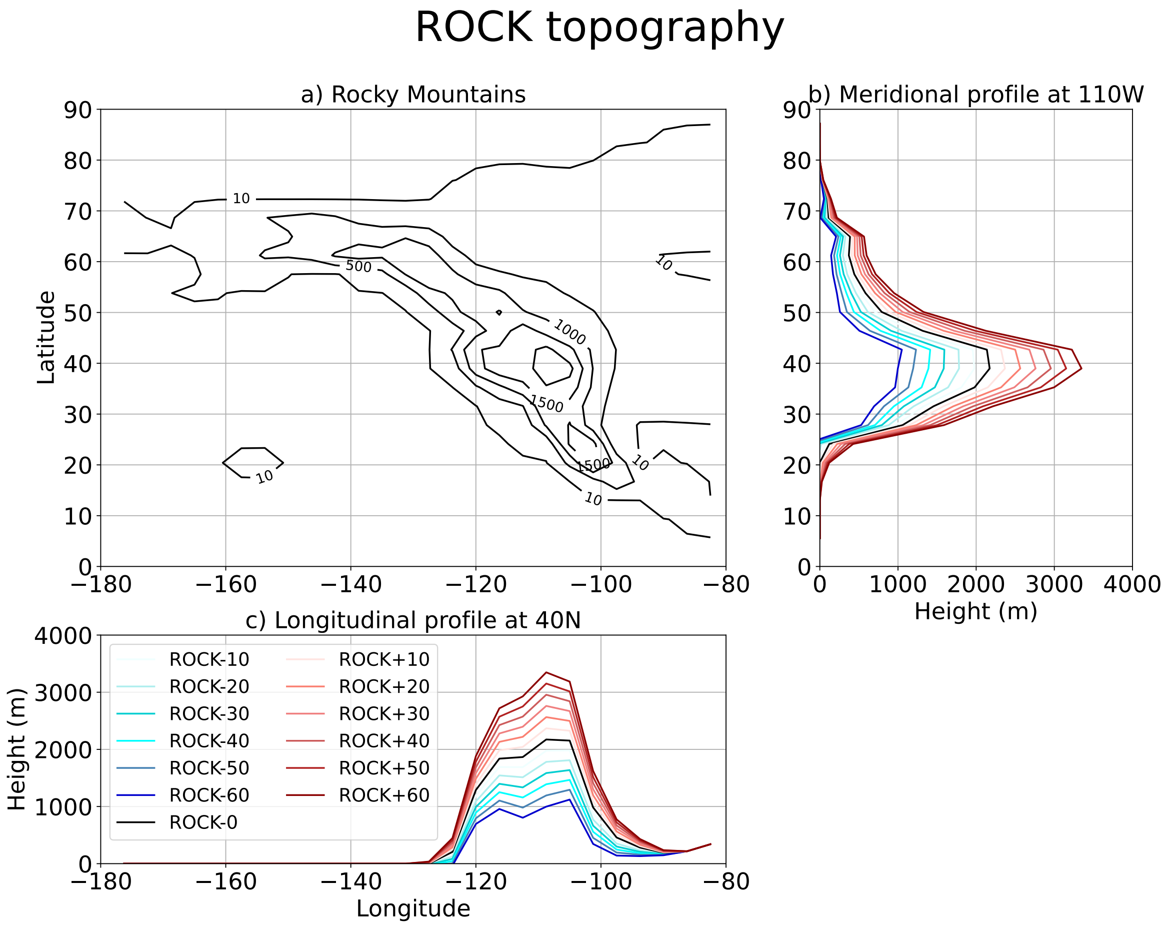

Figure 3.1: Topography for the ROCK experiments (m). a) standard topography, b) meridional profile at 110W and c) longitudinal profile at 40N.

ROCK-0 experiment, in other words, the standard topography for the Rocky Mountains in SPEEDY. Panel b and c are, respectively, the meridional profile at 110W and the longitudinal profile at 40N for each ROCK experiment.

By comparing ROCK experiments with modified orography and ROCK-0, the effectiveness of the orography in producing changes in the mean state of the Pacific jet stream is assessed.

3.2.2 Idealized tropical forcing (ENSO forcing)

To study the impact of the model bias on the response to external forcing, four sets of ENSO-like simulations are conducted. The SST pattern of an idealized ENSO anomaly, both positive (El Niño) and negative (La Niña), is defined in the El Niño 3.4 region (Equatorial Pacific Ocean, 5N-5S, 170W-120W): this anomaly is then superimposed to the climatological SST for all the orographic configurations of the ROCK experiments. The shape and magnitude of the idealized anomaly in the El Niño case are generated as follows:

- from HadSST3 data (1979 to 2008, see Kennedy et al. 2011[62]), all El Niño events are extracted detecting events for which the 5-month running mean of the monthly SST anomalies in the El Nino 3.4 region are greater than 0.5K for six consecutive months or more (for the El Niño 3.4 index, see Trenberth, 1997[108]).

- The SST composite of the above-defined events is computed over the El Niño 3.4 region. For each event, the (6) monthly anomalies are taken. The composite is made by the average of the considered monthly anomalies.

- A nine-grid-point smoothing is applied along the edges of the area.

- This idealized El Niño3.4 anomaly is finally superimposed on the climatological SST.

The red contours in Fig.3.2 show the area and the intensity of the selected idealized El Niño3.4 anomaly. Two sets of experiments are then designed, for both El Niño and La Niña phases. The first set of experiments is conducted with the idealized El Niño3.4 anomaly just described (a “standard intensity” El Niño), which has a maximum of about 1.2K (NINO experiments hereafter). The experiment with El Niño forcing and no orographic change is thus labelled NINO-0. The second set of experiments uses the same anomaly pattern, but doubled in magnitude (i.e. NINOx2 experiments). The experiment with twice El Niño forcing and no orographic change is named NINOx2-0. Following the same methodology, the La Niña and the La Niña with doubled idealized anomalies are obtained by reversing the sign of the El Niño experiments (defined as NINA and NINAx2 experiments). Similarly, the experiments with no orographic change, are labelled NINA-0 and NINAx2-0, respectively.
Since the ENSO signal is stronger during the late boreal winter, i.e., January-March (JFM) (Brönnimann 2007[23], King et al. 2021[63]), the analysis is limited to this season.
Similarly to the ROCK experiments, the NINO, NINOx2, NINA, and NINAx2 integrations are 200-year long. All the simulations start from an atmosphere at rest and in order to discard the spin-up of the model, the first year of each integration is excluded.
By comparing ENSO experiments (NINO, NINOx2, NINA, NINAx2) and the corresponding ROCK simulations it is possible to estimate the modulation of the ENSO signal due to the change of the model mean state.
This idealized configuration has strengths and limitations; on the one hand, the idealized SST forcing helps to understand the mechanism behind the interaction between the bias of the Pacific Jet stream and the ENSO response, isolating the source of the signal over the Central Pacific. On the other hand, the observed ENSO SST signal is characterized by anomalies outside the Niño3.4 region that might generate non-negligible signals and non-linear interactions with the signals coming from the Niño3.4 region.

3.3 Reanalysis and fully-fledged general circulation models

To provide an estimate of the SPEEDY biases in the ROCK and ENSO experiments the ECMWF ERA-Interim Reanalysis (1979-2018) is used. The El Niño signal is obtained by compositing the geopotential height field during the El Niño events (in the 1979-2018 period) identified with the Nino3.4 index. The reference for state-of-the-art general circulation models is the Coupled Model Intercomparison Project phase 6 (CMIP6, Eyring et al. 2016[42]): considering the atmosphere-only setup of the SPEEDY integrations, the focus is on the Atmospheric Model Intercomparison Project experiment (AMIP, Gates et al. 1998[44]). AMIP simulations are performed over the historical period 1979-2014, with observed sea surface temperature and sea-ice and observed greenhouse gases (GHGs) and stratospheric ozone mixing ratios and aerosol emissions. Because models have different resolutions, all the model outputs are interpolated to a 2.5°x2.5° regular lat-lon grid[1].

3.4 Metrics: Jet Indices

Considering the relevance for this study of the propagation of signals from the tropics to the extratropics, the position of the so-called "Rossby stationary Waveguide" is of key importance (Hoskins and Ambrizzi,1993[58]; Ambrizzi and Hoskins, 1997[4]). The Rossby stationary waveguide is strictly related to three parameters characterizing the jet stream: 1) the jet strength, 2) the latitudinal position of the jet maximum and 3) the jet width (Manola et al. 2013[78]). Therefore, in order to characterize the mean state of each ROCK simulation, three dynamical indices that define such properties of the jet stream are introduced. A Jet Strength index (JS), a Jet Latitude index (JL) and a Jet width index (JW). The two indices are calculated for the two Jet streams of the Northern Hemisphere, the Pacific Jet and the Atlantic jet. To distinguish the properties of the two Jets, a letter is added to the indices acronyms. The indices for the Pacific Jet are labelled with the letter P, leading to a Pacific Jet Strength index (PJS), Pacific Jet Latitude index (PJS) and Pacific Jet Width index (PJW). Similarly, the indices for the Atlantic Jet are labelled using the letter A. Atlantic Jet Strength index (AJS), Atlantic Jet Latitude index (AJS) and Atlantic Jet Width index (AJW). The indices are calculated as follows:

- the PJS index is the average of the 850 hPa zonal wind in a box spanning 110-170W and 30-60N, and it is used to measure the intensity of the Pacific jet stream;
- the PJL index is the average of the 850 hPa zonal wind in a box 110-170W and 45-60N minus the same average in a box 110-170W and 30-45N. The PJL index aims at

---

[1] List of CMIP6 models used: ACCESS-CM2, ACCESS-ESM1-5, BCC-CSM2-MR, BCC-ESM1, CAMS-CSM1-0, CanESM5, CAS-ESM2-0, CESM2, CESM2-FV2. CESM2-WACCM, CESM2-WACCM-FV2, CIESM, EC-Earth3, EC-Earth3-Veg, FGOALS-f3-L, FGOALS-g3, FIO-ESM-2-0, GFDL-ESM4, INM-CM4-8, INM-CM5-0, IPSL-CM6A-LR, MIROC6, MPI-ESM2-0, NorESM2-LM.

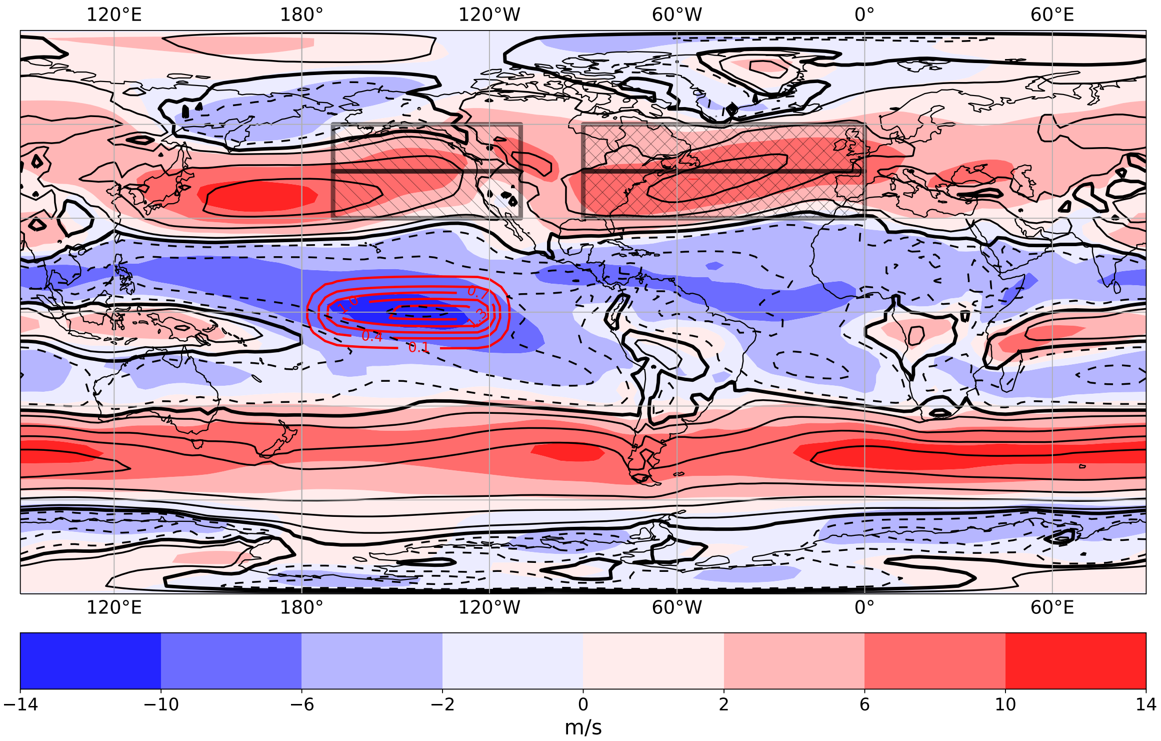

Figure 3.2: SPEEDY zonal wind at 850 hPa mean state for the winter season(DJF). Boxes indicate the regions where the PJ and AJ indices are calculated.

describing the latitudinal position (and therefore the associated meridional wind shear) of the Pacific jet stream.

- the PJW is estimated as the distance between the inflexion points of the meridional profile of the zonally averaged zonal wind at 850hPa, between 110W and 170W.

- the AJS index is the average of the 850 hPa zonal wind in a box spanning 90-0W and 30-60N, and it is used to measure the intensity of the Atlantic jet stream;

- the AJL index is the average of the 850 hPa zonal wind in a box 90-0W and 45-60N minus the same average in a box 90-0W and 30-45N. The AJL index aims at describing the latitudinal position (and therefore the associated meridional wind shear) of the Atlantic jet stream.

- he AJW is estimated as the distance between the inflexion points of the meridional profile of the zonally averaged zonal wind at 850hPa, between 90W and 0W.

3.4.1 Metrics: turning latitude

Rossby stationary waves can be produced following the onset of ENSO. The way Rossby waves propagate in a slowly varying flow following pathways that are similar to rays in optics

(Hoskins and Ambrizzi 1993[58]). These ‘rays’ are affected by variations in background wind, the thermal structure, and the orography of the Earth. Rossby stationary waves tend to be ‘refracted’ toward region with larger stationary wavenumber Ks, defined as follows:

$$K_s = \sqrt{k^2 + l^2} = \sqrt{\frac{\beta_M}{U_M}} \tag{3.2}$$

The subscript M indicates the Mercator projection on the sphere. The term β_M is $\cos\phi$ times the meridional gradient of the absolute vorticity on the sphere. ϕ is the latitude. Lines characterized by U=0 are called critical lines. Here the Rossby stationary wavenumber becomes infinite, and Rossby waves tend to be reflected after the absorption of a certain quantity of their wave activity and momentum. From the kinematic wave theory, given a Rossby stationary wave characterized by a fixed K_s, the zonal wavenumber k is constant along the Rossby wave path, so the meridional wavenumber l has to vary, and this change in l is the reason for the variation in the propagation direction. The propagation of the Rossby wave in the meridional direction is stopped when the wave reaches a latitude characterized by a meridional wavenumber equal to zero (l=0); the group velocity becomes purely zonal, so the wave is refracted back to lower latitudes. Latitudes characterized by l=0 are usually called “turning latitudes”. As described above, the presence of a zonal jet affects the propagation of Rossby waves. It is possible to generate some preferred paths or waveguides depending on the background flow. For example two typical waveguides are the westerly winds at the equator and in the upper troposphere. The intensity and the width of the midlatitude jet are two key properties to create an effective waveguide that can propagate the Rossby wave along the zonal direction (Manola et. al. 2013[78]).

The turning latitude can be computed from the meridional profile of K_s. Given a meridional profile of $K_s(\phi)$ and a stationary Rossby wave characterized by a zonal wavenumber n, the turning latitude is the latitude where the function $K_s(\phi)$ crosses the vertical line n=const. In our case, the meridional profile of the stationary wavenumber is calculated by zonally averaging the zonal wind over the Pacific sector (170W-110W) and considering only the Northern Hemisphere (10N-70N). The longitudinal size of the Pacific sector is comparable with the typical scale of quasi-stationary Rossby waves (Scaife et al. 2017[96]).

Chapter 4

ROCK experiments

This chapter illustrates the results of the ROCK experiments, showing all the changes in the mean state for the principal atmospheric variables.

4.1 Jet indices

The jet indices defined in chapter 3 are calculated for each ROCK experiment. Indices are calculated for the early winter (December, January and February, DJF) and late winter (January, February and March, JFM).

4.1.1 Pacific Jet

Figure 4.1a shows the PJS index and its standard deviation as a function of the change in the height of the Rocky Mountains. The effect of the increase of height of the mountains is a reduction of the strength of the zonal wind, the PJS index is progressively smaller, but here are no changes in the standard deviation depending on the Rocky Mountains height.
Figure 4.1b shows that the changes in the height of the Rocky Mountains have a moderate and non-linear impact on the values of the PJL index. While the latitude of the jet is slightly affected by the increase of the orography, the PJL index decreases linearly with lower orography: indeed, a larger negative value of the PJL index implies an equatorward displacement of the Pacific jet. Similarly to the PJS index, the standard deviation of the PJL index doesn't change among the experiments.
in figure 4.1c the PJW index is shown. The effect of orography on the width of the jet is clearly non-linear: a reduction of the height of the Rocky mountains is associated with a narrow jet, on the opposite, an increase of the orographic height doesn't affect the width of the jet. The standard deviation behaves simularly differently, though: a decrease in the height

of the mountains is associated with a decrease in the standard deviation of the PJW index. When the height is increased furter (ROCK = [+10, ... , +60]) the variability of the PJW index exhibits some fluctuations.

4.1.2 Atlantic jet

Fig.4.2 shows the indices of the Atlantic Jet. The effect of the orography on the Atlantic Jet is moderate. Fig.4.2a shows a small modulation of the strength of the jet depending on the height of the Rocky Mountains. The effect is in accordance with the behaviour of the Pacific Jet (Fig.4.1a), an increase in the height of the mountain is associated with a decrease in the strength of the jet, but the intensity of the effect is reduced. Fig.4.2b and Fig.4.2c show respectively the latitude and width indices of the Atlantic jet, there are no changes in both indices.

4.1.3 SPEEDY vs CMIP6

To understand how the Pacific jet stream and the Atlantic jet stream change in the ROCK experiments (e.g., from ROCK-60 to ROCK+60) and how these changes are related to the mean climate of state-of-the-art GCMs, the indices for the strength and latitudinal position of the two jets are calculated from the ROCK simulations and compared with the same indices computed from the CMIP6 simulations. Due to the negligible sensitivity of the PJW index to the orography, this particular index is not considered.

Figure 4.3 shows a scatter plot with the PJS index versus the PJL index for the CMIP6 (orange diamonds) and SPEEDY (black, blue and red dots) experiments, all compared to ERA-Interim (the black star). Figure 4.4 is the analogue, but for the Atlantic Jet.

In the Pacific Ocean, the vast majority of models show a relevant bias in the PJL index with respect to reanalysis, with a Pacific jet displaced poleward. On the other hand, PJS indices from CMIP6 models and ROCK experiments are scattered around the value of the reanalysis; the PJS values range from 4 to 6 (the reanalysis is about 5). The ROCK experiments cover approximately a fair amount of the CMIP6 model spread in terms of the PJS index; on the other hand, the PJL index covers only a small portion of the CMIP6 models.

The Atlantic ocean shows a very different picture. The reduced sensitivity to the height of the Rocky Mountains is reflected in both the AJS and AJL indices. All the ROCK experiments show an AJS index lower than that of ERA-Interim and the values cover only a small portion of the CMIP6 variability. The same is observed for the AJL index: ROCK experiments have a jet slightly shifted equatorward, which doesn't exhibit a substantial sensitivity to the height of the Rocky Mountains and its values cover only a minimal portion of that shown by the

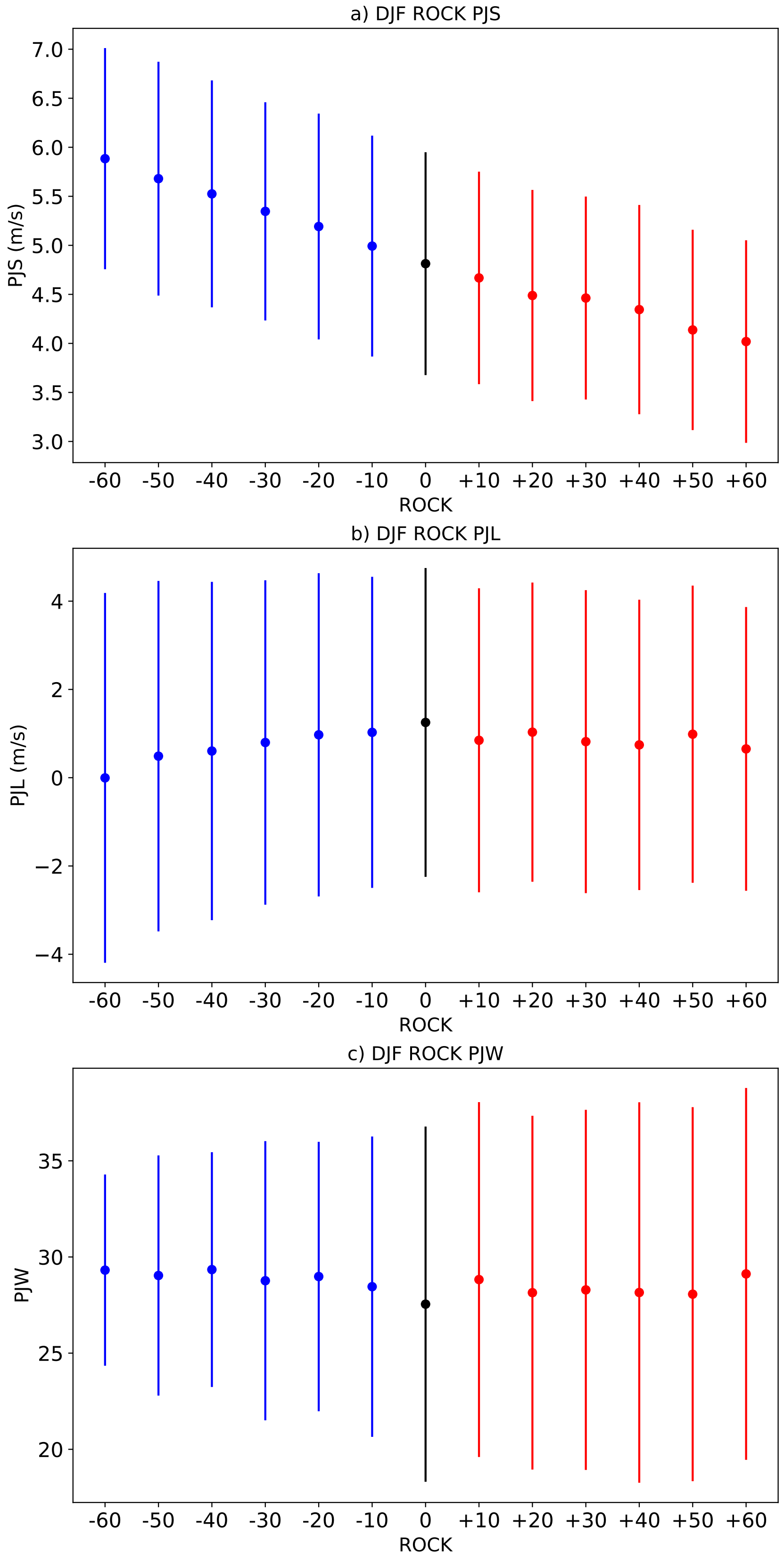

Figure 4.1: Winter season Pacific Jet indices. a) PJS index, b) PJL index, c) PJW index.

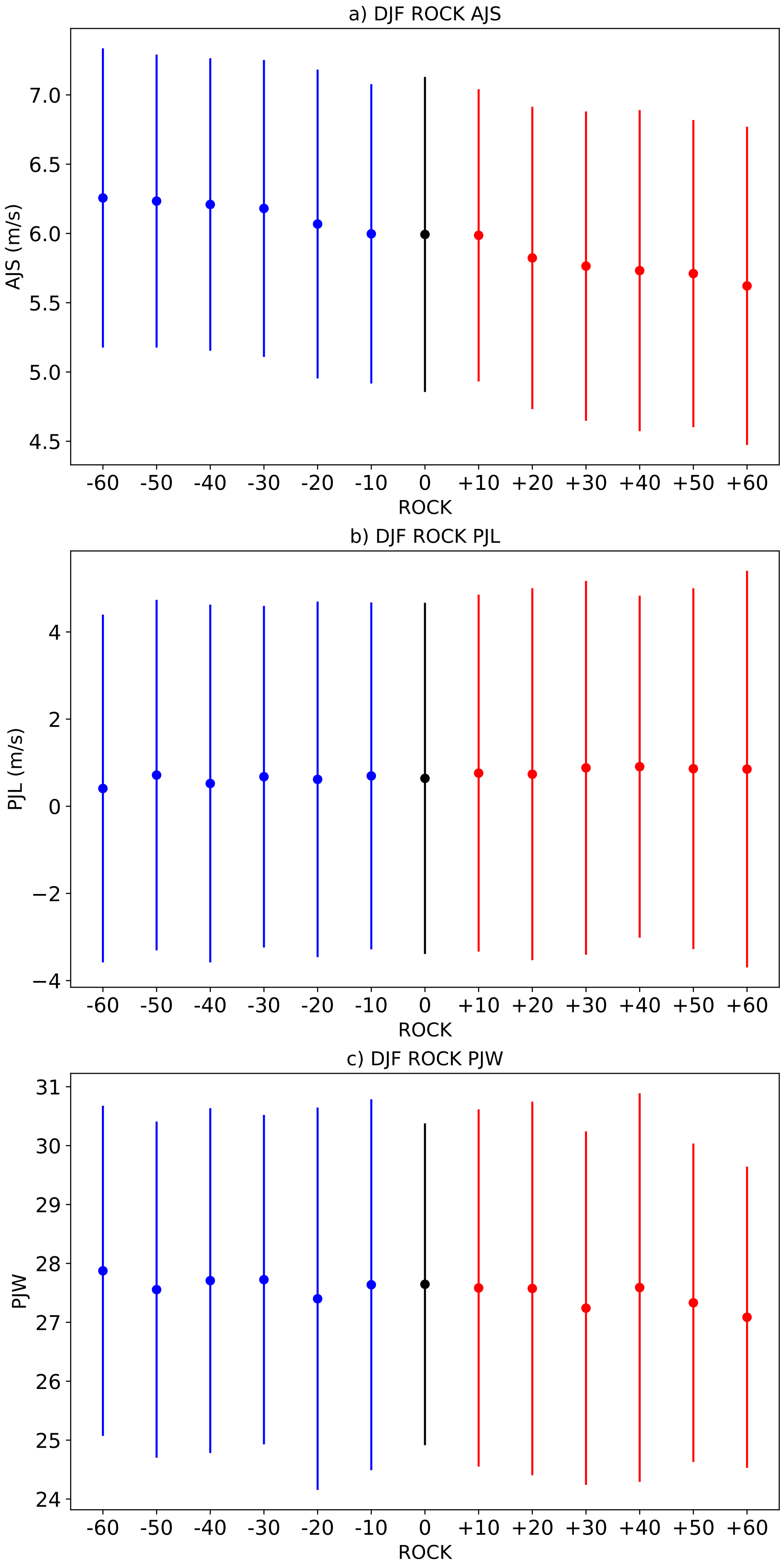

Figure 4.2: Winter season Atlantic Jet indices. a) AJS index, b) AJL index, c) AJW index

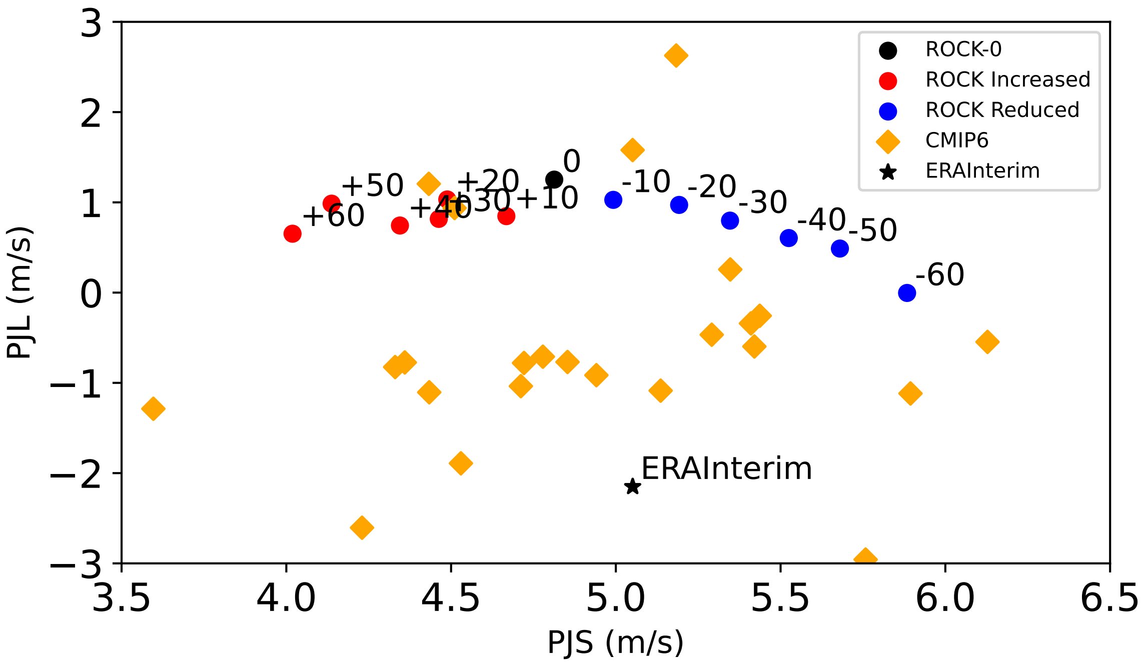

Figure 4.3: DJF PJL index vs PJS index. Orange diamonds are models from CMIP6, blue dots are ROCK experiments with reduced orography, red dots are ROCK experiments with increased orography, the black dot is the ROCK-0 experiment and the black star is ERA-Interim.

CMIP6 models.
The AJS and AJL indices are representative of the jet core and do not take into account the jet exit region over Europe, where the bias is different (see section3.1.3).

4.2 The Climatology

The effects of changes in the height of the Rocky Mountains on model climatology are examined in this section. The focus is on the model mean state.

4.2.1 The mean state

Zonal wind

Figures 4.5, 4.6 and 4.7 show the winter season (DJF) zonal wind at three different geopotential levels: 850 hPa, 300 hPa and 30 hPa. These levels represent, respectively, the lower troposphere, upper troposphere and lower stratosphere. Each figure is composed of three panels; panels a) and c) show the zonal wind, for the DJF season, as the difference between ROCK±60 and ROCK-0, while panel b reports the linear regression of the zonal wind to the

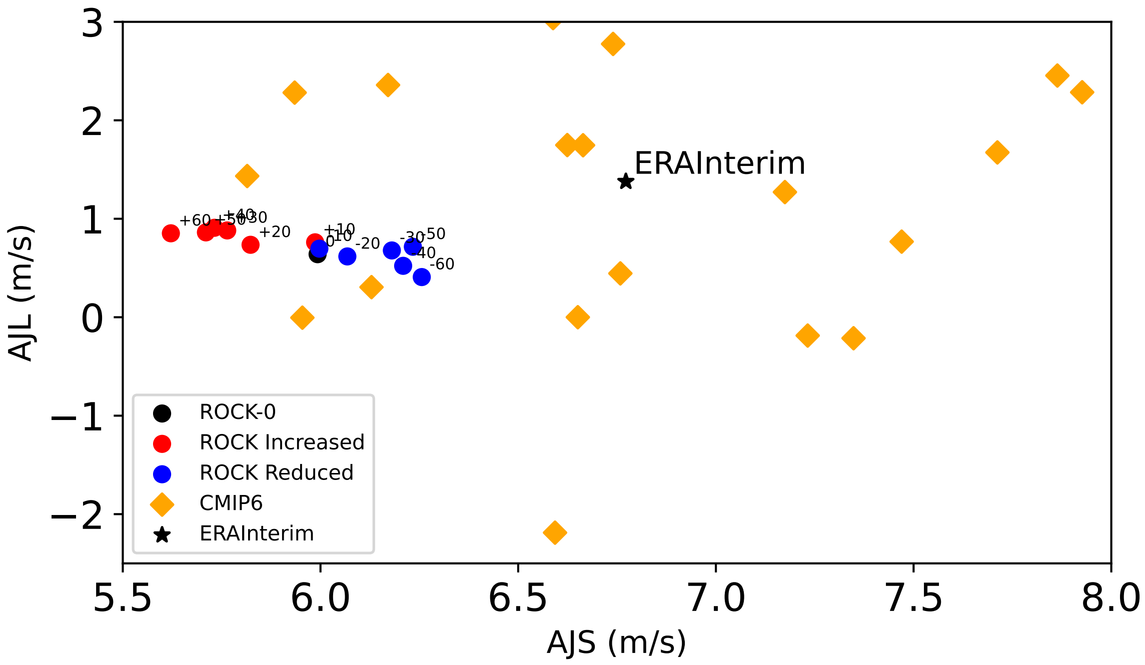

Figure 4.4: DJF AJL index vs AJS index. Orange diamonds are models from CMIP6, blue dots are ROCK experiments with reduced orography, red dots are ROCK experiments with increased orography, the black dot is the ROCK-0 experiment and the black star is ERA-Interim

PJS index across all the ROCK experiments. In panels b) of these figures, shades represent the regressions (all the average JFM fields from ROCK experiments are merged together into a single array and then the linear regression is calculated) and the black contours are the full field of the ROCK-0. The thicker line in panel b) is the zero level contour. For all the panels, stipplings mark the regions where the results are statistically significant using a two-tailed t-test and a significance level of 95%.

In Figure 4.5 (850 hPa) the main impact on the flow due to changes in the Rocky Mountains height is found over the North American continent and the North Pacific basin, with a secondary structure over the North Atlantic and Eurasia. As expected from Figure 4.3, the ROCK-60 experiment (Fig.4.5a) is characterized by a stronger jet. The signal in the zonal wind is maximum over the mountains, and it spreads mainly upstream up to the center of the Pacific Ocean. The ROCK+60 experiment (Fig.4.5c) shows an opposite behaviour, with the effect of the orography localized only on the region of the Rockies and downstream, over the North American continent.

The linear regression in Fig.4.5b shows the relation between the lower-tropospheric zonal wind and the PJS index: a stronger Pacific jet is associated with an intensified zonal wind over the Rocky Mountains in a latitude band between 30N and 50N. At latitudes below 30N, the effect of a stronger Pacific jet is the reinforcement of the trade winds. In a latitudinal band between 50N and 70N, the response of the zonal wind reverts; a stronger Pacific jet

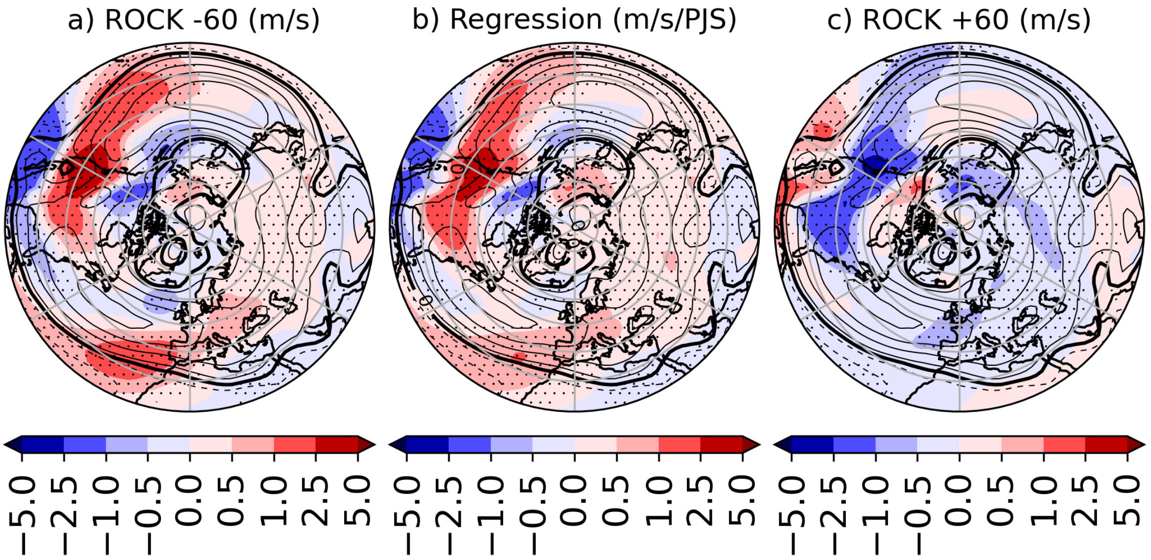

Figure 4.5: DJF 850 hPa zonal wind (m/s). (a,c) Differences between the modified orography experiments (ROCK-60 and ROCK+60) and ROCK-0 (shading). (b) linear regression of the zonal wind from all ROCK experiments on the PJS index. Contours are the full field from the ROCK-0 (the step of the contours is 2.5 m/s). Stippling shows regions where the values are statistically significant (two-tailed t-test, α=0.05).

weakens the zonal wind. Two smaller but significant signals are found over the tropical Atlantic Ocean (60W-0W) and in the mid-latitudes of the Euro-Asiatic sector; here, the zonal wind strengthens with a more intense Pacific jet.

Figure 4.6 shows the DJF zonal wind at 300 hPa. At this level, the orography induces larger anomalies than the lower troposphere, but, when the anomalies are compared to the mean state, the differences are proportionally smaller. The signal changes from local confinement to a wider spread around the globe. The experiment ROCK-60 (Fig.4.6a) is characterized by an intensification of the Pacific jet stream in the exit region over the Rocky mountains. The Atlantic jet stream is weaker in the entrance region (North American Continent) and stronger in the exit region over Europe. The experiment ROCK+60 (Fig.4.6c), as for the zonal wind at 850 hPa, shows an opposite behaviour with a weaker Pacific jet in the exit region and a stronger Atlantic jet in the entrance region.

From the regression (Fig.4.6b) on the PJS index it is possible to see the relationship between the lower and the upper troposphere; a stronger jet at lower levels is associated with a stronger jet at upper levels. The intensification of the jet has its maximum in the exit region of the Pacific jet and propagates upstream crossing the dateline. A stronger low-level Pacific jet is also associated with a stronger upper tropospheric Atlantic jet in the exit region. On the other hand, the Atlantic jet is weakened in the entrance region.

Fig.4.7 shows the DJF zonal wind at 30hPa (lower stratosphere and the topmost level of the SPEEDY model). In the stratosphere, the difference between experiments ROCK-60 and ROCK-0 (fig.4.7a) shows two distinct behaviours: at mid-latitudes, a strong signal is

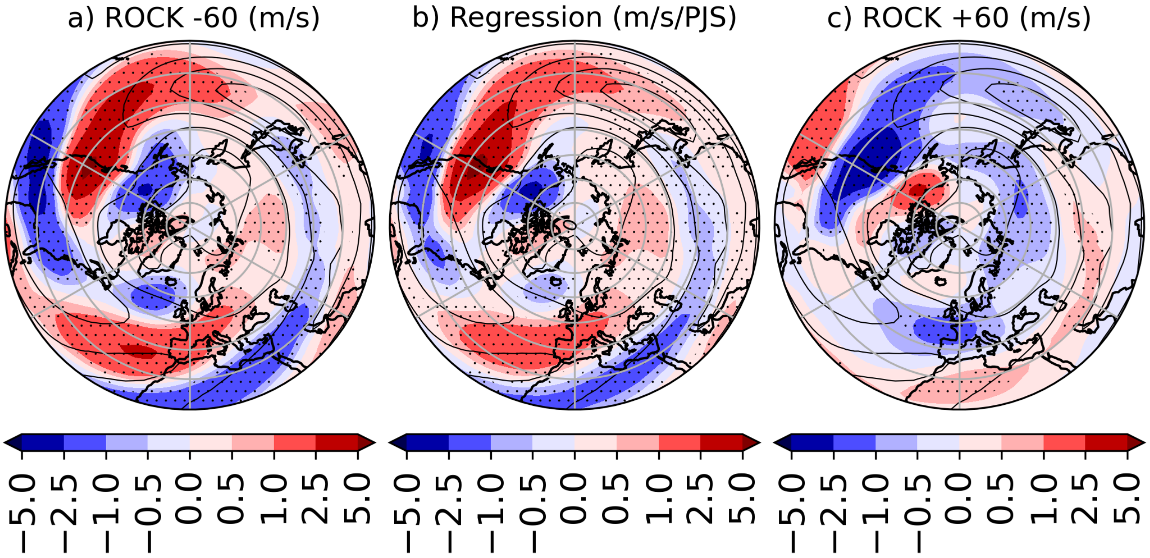

Figure 4.6: as Fig.4.5, but for 300 hPa zonal wind (m/s), the step of the contours is 10 m/s.

associated with a reduction of the intensity of the wind over the Rocky mountains and downstream. Over Asia and the Pacific ocean, the sign of the signal changes, from negative to positive, and the zonal wind is increased. At higher latitudes, near the pole, the effect of the reduction of the height of the mountains is characterized by a positive signal around 60W and a negative signal between 180E and 120E. Figure 4.7c shows the ROCK+60 experiment, the different behaviour between mid-latitudes and high-latitudes, observed in fig.4.5 and fig.4.6, is more evident, the sign of the response is the opposite with respect to that in the ROCK-60 experiment.

The regression between the PJS index and the zonal wind (Fig.4.7b) shows that a stronger jet at the lower troposphere is associated with a weaker wind in the lower stratosphere when the North American and North Atlantic sectors at mid-latitudes are considered. Conversely, the wind over Eastern Asia and Japan is reinforced. Moving to higher latitudes, a stronger tropospheric jet induces a reinforcement of the polar vortex in a range of longitudes going from 0 to 120 W, on the other hand, the polar vortex over the pacific ocean is weaker.

Figure 4.8 shows the latitude-height cross-section of the zonal wind. The experiment ROCK-60 (Fig.4.8a) shows that the effect of a reduction of the height of the Rocky Mountains is the intensification of the zonal wind inside a latitudinal band going from 25N to 50N; the effect propagates from the surface to 100 hPa. From about 400 hPa, at both sides (northward and southward) of the positive signal, the zonal wind is weaker. In the stratosphere, the effect of the orography changes the sign, at lower latitudes from the equator to about 25N, the zonal wind increases, at higher latitudes from 25N to 75N the zonal wind is weaker. Fig.4.8c shows the same pattern as Fig.4.8a for the experiment ROCk+60 minus ROCK-0, but, as expected, the sign of the difference is the opposite with respect to the ROCK-60 experiment.

The regression (Fig.4.8b) shows the link between the Pacific jet strength in the lower tropo-

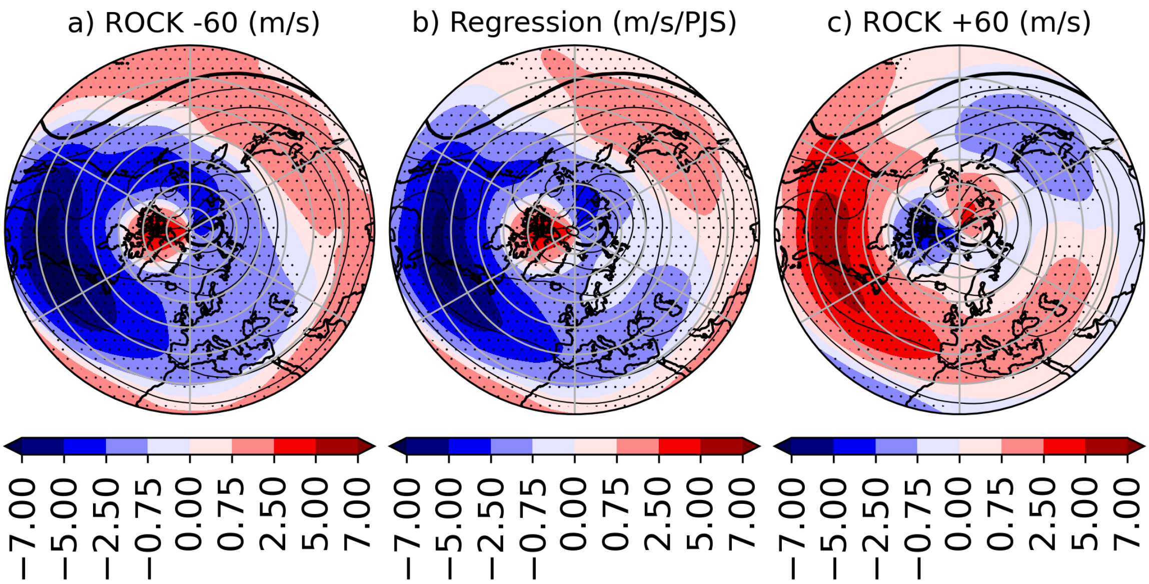

Figure 4.7: as Fig.4.5, but for 30 hPa zonal wind (m/s), the step of the contours is 10 m/s.

sphere and the zonal wind in the vertical column above the region of the orographic changes. The lower troposphere is characterized by a stronger wind with a stronger Pacific Jet. From 400 hPa the regression shows a stronger latitudinal dependence between the PJS index and the zonal wind and, lastly, in the stratosphere the behaviour of the wind changes completely with respect to the troposphere.

Meridional wind

Figure 4.9 shows the meridional component of the wind, calculated at 850 hPa, for the ROCK experiments. The Rocky Mountains divert the mean flow, as can be seen from the black contours in the figure, which refer to the ROCK-0 experiment. Upstream of the Rockies, at latitudes higher than 40N, a strong positive meridional component of the wind is associated with a northward displacement of the air parcels; at the same time, lower latitudes exhibit negative values for the meridional wind. The air parcels move northward and southward around the topography. Downstream of the Rockies, the effect is reversed, at higher latitudes, the meridional wind is negative, while at lower latitudes is positive. The Atlantic Ocean is dominated by positive values of the meridional component of the wind. Regions far away from the North American Continent show weak signal generated by the local orography. Other regions with strong meridional wind are the Hymalaia and eastern Asia. These regions are characterized by a strong negative meridional wind, especially over Japan.

The experiment ROCK-60 (Fig.4.9a) shows a reduction of the previously described effect. By reducing the orography, the meridional component of the wind, over the west coast of Alaska, Canada and the United states, is reduced; indeed, the figure shows a negative anomaly

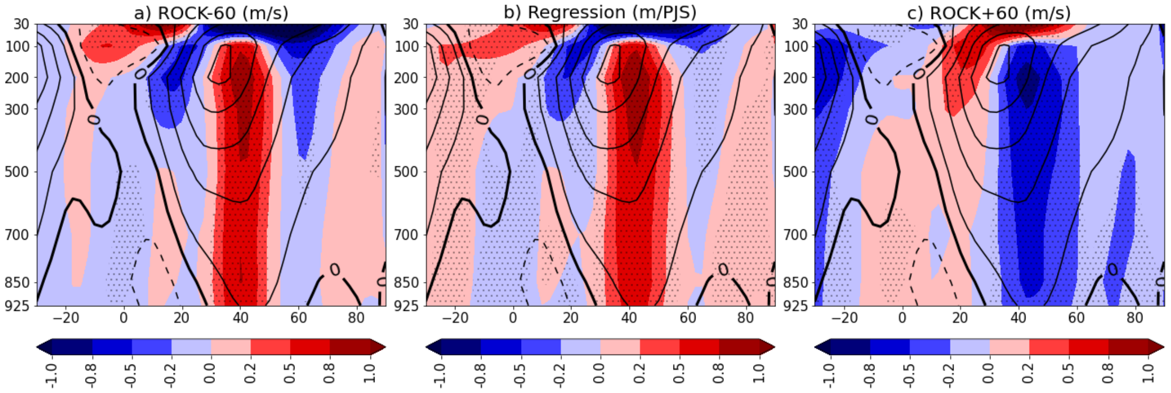

Figure 4.8: DJF zonal wind latitude-height cross-section (m/s). (a,c) Differences between the modified orography experiments (ROCK-60 and ROCK+60) and ROCK-0 (shading). (b) linear regression of the geopotential height from all ROCK experiments on the PJS index. Contours are the full field from the ROCK-0 (the step is 2.5 m/s). Stippling shows regions where the values are statistically significant (two-tailed t-test, α=0.05).

in these regions. A second negative anomaly can be found over the California Peninsula and the west coast of Mexico. Around 50N, upstream of the Rockies and over the ocean, a positive meridional wind anomaly is overimposed on the negative meridional wind from the control experiment. Downstream of the Rockies, over the North American continent and the Atlantic Ocean, the effect of the orography reduction is a weakening of the absolute value of the meridional wind; the region of southward motion over Canada is dumped by a positive anomaly and the poleward component of the wind over the Atlantic Ocean is reduced by a negative anomaly. Over Europe and North Africa, a positive anomaly dominates the response to orography. Fig.4.9c illustrates the ROCK+60 experiment and confirms (in reverse) the results of ROCK-60. In this case, the effect of increasing the orography is a strengthening of the ROCK-0 patterns. Interestingly, the signals of the experiments ROCK-60 and ROCK+60 are symmetric with respect to zero when considered close to the forcing region (the Rockies); but moving downstream, above the ocean, the experiment ROCK+60 has a signal with smaller absolute value compared to ROCK-60.

The regression of the meridional wind to the PJS index (Fig.4.9b) shows a (not unexpected) relation between meridional wind and zonal wind. Higher values of the PJS index are associated with a weakening of the meridional wind. Upstream of the Rockies, the response is characterized by a dipole with a negative anomaly at higher latitudes and a positive anomaly at lower latitudes. Above the continent and the Caribbean, the response is still a dipole, but the sign is reversed. The signal is positive at higher latitudes and negative at lower latitudes. Similarly, the signal over the Pacific ocean is weakened by a larger PJS index. The easternmost area with a clear correlation between the meridional wind and the PJS index is the western Europe where a positive meridional wind anomaly is associated with larger values of the PJS index. Figure4.10 shows the meridional component of the wind in the upper troposphere.

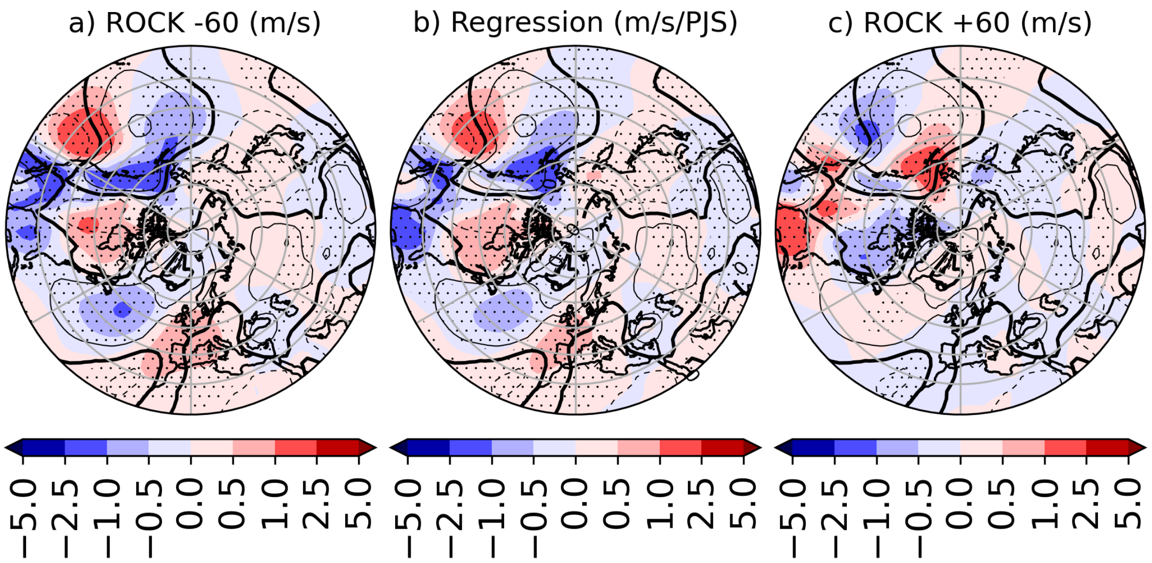

Figure 4.9: DJF 850 hPa meridional component of the wind (m/s). (a,c) Differences between the modified orography experiments (ROCK-60 and ROCK+60) and ROCK-0 (shading). (b) linear regression of the zonal wind from all ROCK experiments on the PJS index. Contours are the full field from the ROCK-0 (the step of the contour is 2.5 m/s). Stippling shows regions where the values are statistically significant (two-tailed t-test, α=0.05).

(300 hPa). At this level, the intensity of the wind is larger than in the lower troposphere, but the two patterns are quite similar. Above the Rocky Mountains, the control experiment is dominated by a negative component of the wind which elongates upstream and southward over the ocean. The sign of the meridional wind is reversed at higher latitudes. Downstream, a positive meridional wind characterizes the western North Atlantic Ocean; as for the negative wind over the continent, this positive pole elongates upstream and southward reaching the southern United States and Mexico. Eastern Atlantic Ocean and Europe are regions of negative meridional wind.

The effect of a reduction of the height of Rocky mountains (Fig.4.10a) is, as in the lower troposphere, a weakening of the absolute value of the meridional wind. In the proximity of the Rockies, the anomalies, generated by changes in the orography, take the shape of a quadrupole. The positive anomalies are in the SW and NE sectors, and the negative anomalies are in the SE and NW sectors. The western Atlantic Ocean is characterized by a negative meridional wind anomaly. Finally, the Eastern Atlantic Ocean and Europe are subject to a positive anomaly. The response in the upper troposphere (experiment ROCK+60, Fig.4.10c), is consistent with that of the lower troposphere.

The regression of the meridional wind to the PJS index (Fig.4.10b) confirms the results from lower levels of the atmosphere. But, conversely, a change of one unit of the PJS index (m/s) induces changes in the upper troposphere, downstream of the Rockies, that are five time larger than the changes in the lower troposphere. Upstream of the Rockies the effect is about the same.

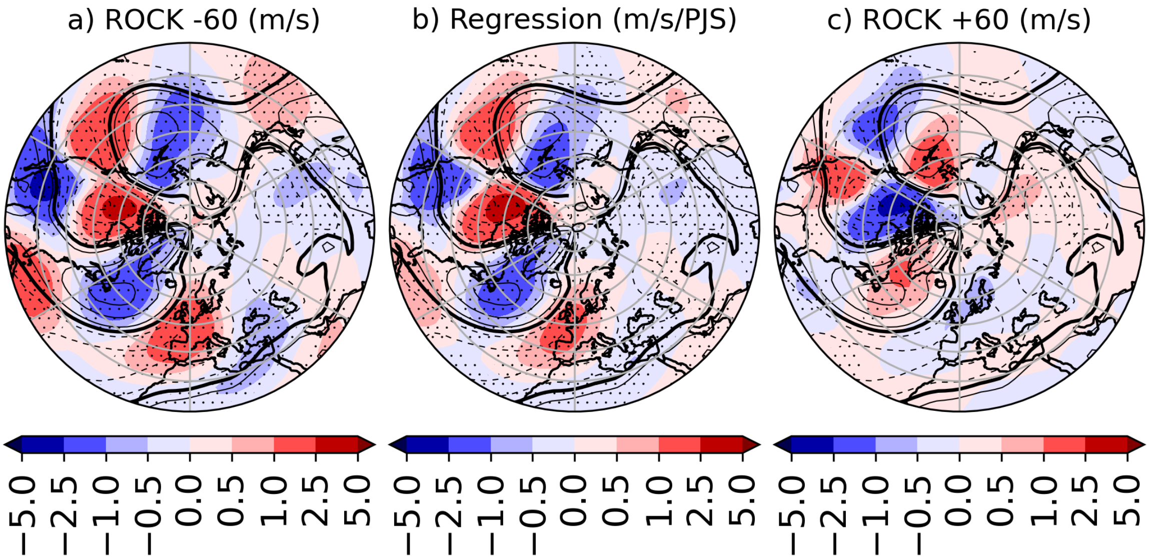

Figure 4.10: as Fig.4.9, but for meridional wind (m/s) at 300 hPa.

Geopotential height

Geopotential height in the troposphere (500 hPa, Fig.4.11) shows a response due to the orographic changes in two regions: the North American Continent (the region of the forcing) and the eastern North Atlantic. Figure 4.11a shows the response to a decrease in the height of the Rocky Mountains. Over North America, the difference in the geopotential height shows a dipolar signal characterized by a negative anomaly on the northward side of the mountain and a positive anomaly on the southern side. In the Eastern North Atlantic, the response shows a negative signal which elongates northward reaching the North Pole. A smaller positive signal is present over North Africa, southern Europe and the middle west. The response due to an increase in the height of the mountains (Fig.4.11c) is characterized by opposite anomalies.

The regression of the geopotential height on the PJS index (Fig.4.11b) summarizes these results, and shows the relation between the geopotential height and the zonal wind in the lower troposphere. When the zonal wind on the exit region of the jet increases in strength, the geopotential height in the Eastern North Pacific, at latitudes greater than 40N, the North Pole and the Eastern North Atlantic decreases in intensity. On the opposite, the geopotential height on the Eastern North Pacific, at lower latitudes, the region east of the Hudson Bay and the Mediterranean area, including North Africa and the Middle East, increase.

Figure 4.12 shows the geopotential height at 100 hPa, a layer closer to the stratosphere. At this level, the pattern of the response differs from lower levels. When the orography is reduced (Fig.4.12a), the principal signal is an increase in the geopotential height over North America with the maximum of the center of action around the Hudson Bay. A negative

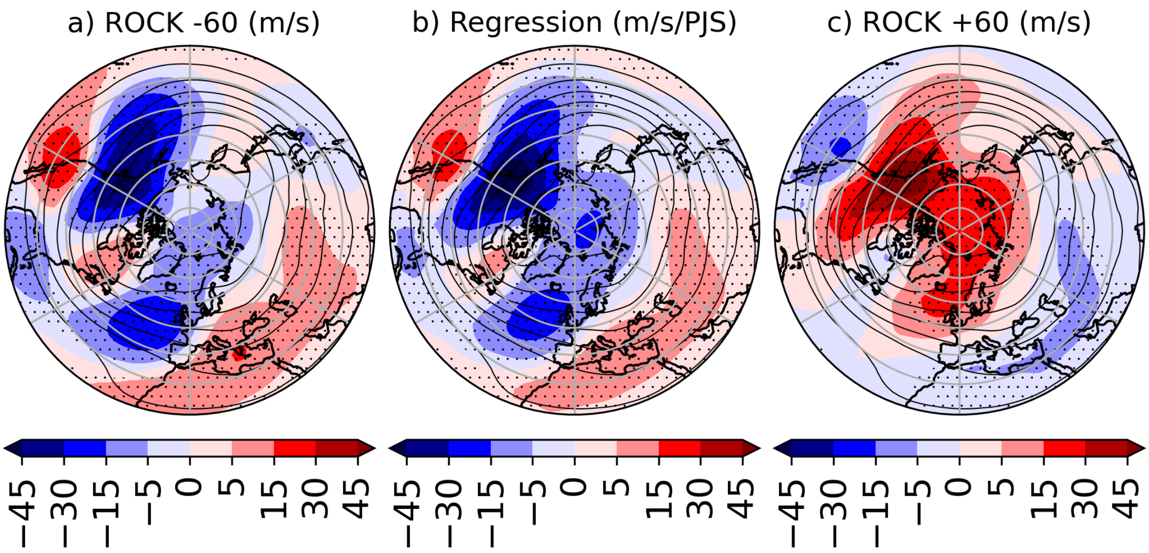

Figure 4.11: DJF 500 hPa geopotential height (m). (a,c) Differences between the modified orography experiments (ROCK-60 and ROCK+60) and ROCK-0 (shading). (b) linear regression of the zonal wind from all ROCK experiments on the PJS index. Contours are the full field from the ROCK-0 (the step of the contour is 100 m starting from 5100m). Stippling shows regions where the values are statistically significant (two-tailed t-test, α=0.05).

geopotential height anomaly is generated over the Pacific Ocean and it elongates upstream covering Asia. On the other hand, when orography is increased (Fig.4.12c)the signal is more confined. The response over North America is positive, but its magnitude is a little weaker, if compared with that of Figure 4.12a. Another positive anomaly can be found on the eastern boundary of Russia.

In summary, the regression of geopotential height on the PJS index (Fig.4.18b) points to a clear increase of the signal over North America and the Northern Atlantic with a stronger Pacific Jet. On the contrary, the signal over the Northern Pacific Ocean is weaker when the Pacific Jet strengthens.

Precipitation

The effects of changes in the height of the Rocky Mountains on the total precipitation can be seen in Figure4.13. Figure 4.13a, which refers to the experiment ROCK-60, shows a reduction of the total precipitation on the west coast of Alaska and Canada. In the latitudinal band between 40N and 50N, the total precipitation shows a small increase both over the ocean and over the North American continent. The region comprising Mexico and Florida is another region characterized by a decrease in precipitation. Figure 4.13c shows the effect of an increase of the orography on the total precipitation. The stronger signal is located over the Florida Peninsula where the precipitation has a marked increase in amplitude. Two other

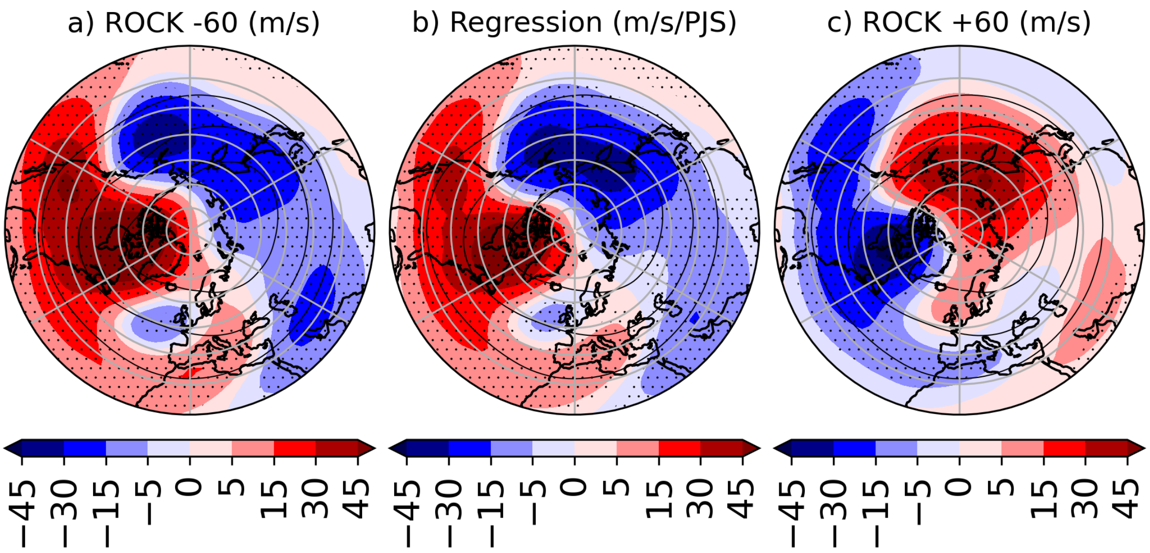

Figure 4.12: as Fig.4.11, but for 100 hPa geopotential height (m), the step of the contour is 500m starting from 15000m.

regions with an increase in precipitation are the Lower California peninsula and the western coast of Canada. The principal decrease in precipitation, at mid-latitude, is over the western part of the border between the United States and Canada.

As usual, a summary of the response, is given in panel (b) where the regression of the total precipitation on the PJS index (Fig4.13b) confirms the results of Figure 4.13a/c. With a stronger Pacific jet, over the North American continent, the total precipitation increases in a region of latitudes between 40N and 50N, over the Eastern Pacific Ocean, and between 40N and 60N over Canada. An opposite behaviour is found on the west coast of Canada, the Lower California peninsula and Florida. In these three regions, the stronger the jet the smaller the total precipitation. The largest signal is over Florida where the precipitation decreases by 1.5 mm/day for an increase of 1 m/s of the jet speed.

Temperature

Figure 4.14 shows the near surface air temperature of ROCK experiments. Experiment ROCK-60 (Fig.4.14) has a clear increase of the near surface air temperature over the Rocky Mountains. The warming is a direct consequence of the orography reduction. Alaska and the Caribbean are two regions characterized by a decrease of the near surface air temperature.

Figure 4.14 shows changes in the temperature for the experiment ROCK+60. When the height of the Rocky Mountains increases, the near surface air temperature decreases in the region of orographic changes. Contrarily, two warm anomalies appear over Alaska and the Caribbean. Results from ROCK+60 are about the opposite of that from ROCK-60.

The regression of the near surface air temperature to the PJS index shows a relation between

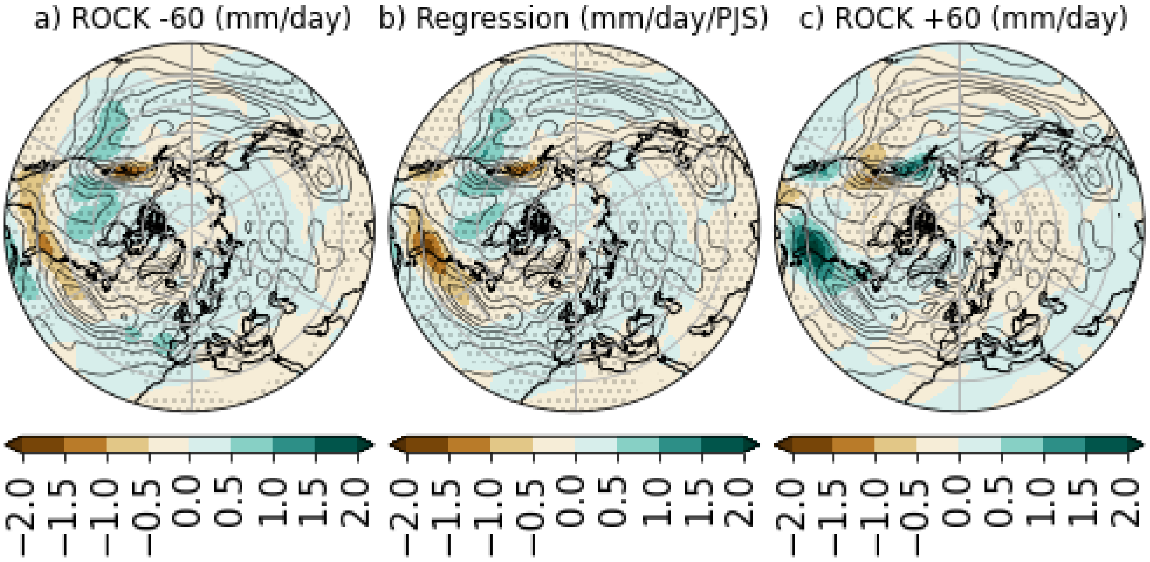

Figure 4.13: DJF total precipitation (mm/day). (a,c) Differences between the modified orography experiments (ROCK-60 and ROCK+60) and ROCK-0 (shading). (b) linear regression of the zonal wind from all ROCK experiments on the PJS index. Contours are the full field from the ROCK-0 (the step of the contour is 1 mm/day). Stippling shows regions where the values are statistically significant (two-tailed t-test, α=0.05).

the two quantities. A stronger wind in the Pacific Ocean induces a warm temperature anomaly over North America, with the exception of Alaska, where the temperature decreases. The Caribbean and the south-east of the United State are similar to Alaska, in these regions an increase of the zonal wind implies a decrease of the near surface air temperature. Figure 4.14 contains both the temperature difference directly originated from changes in orography and the temperature anomaly generated by different mean states. In order to isolate the effect of the mean state, the signal from the orography is removed. Figure 4.15b shows only the temperature anomaly due to changes in the mean state. A stronger Pacific Jet reduces the near surface temperature of all the North American continent and increases the temperature on the Europe. On the contrary, a weaker Pacific Jet Stream increases the temperature on the North America and decreases the temperature in Europe. By comparing figure 4.14b and figure 4.15b is clear that the temperature anomaly generated by changes in orography dominates over the North American mountain chains, with a signal that is 6K larger then the one generated by changes in the mean state.

Figure 4.16 shows the vertical cross-section for the temperature. Fig.4.16a shows signals due to a reduction of the orography, only the levels above 400 hPa are considered. From the Equator to 40N, the stratosphere undergoes a reduction in its temperature. From 40N to the pole, the temperature anomaly is positive and is located in both the upper troposphere and stratosphere. A small positive signal appears in the lower troposphere around 75N. The panel associated with the anomaly in temperature due to an increase in the height of the Rocky

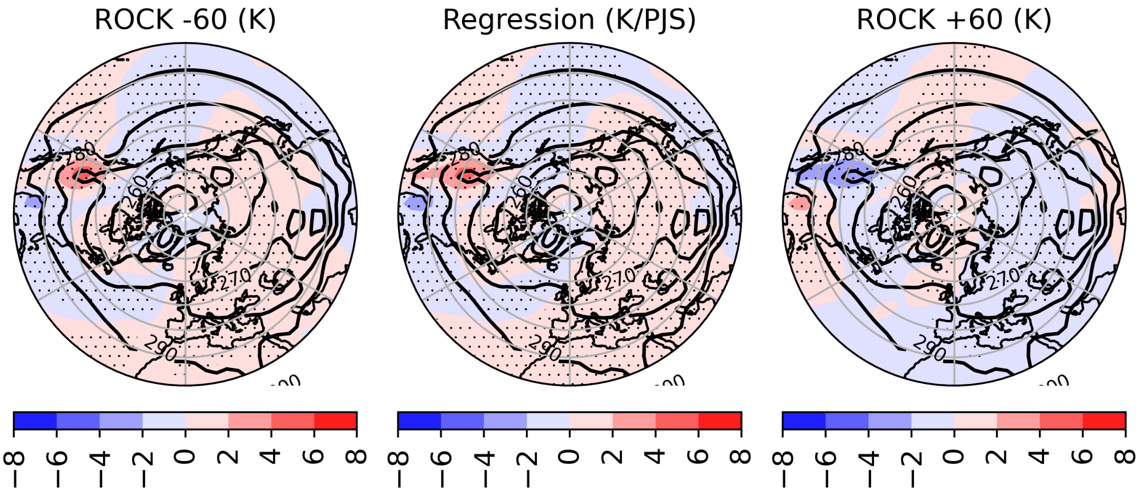
ROCK -60 (K)
Regression (K/PJS)
ROCK +60 (K)
280
260
270
290
−8
−6
−4
−2
0
2
4
6
8

Figure 4.14: DJF near surface air temperature (K). (a,c) Differences between the modified orography experiments (ROCK-60 and ROCK+60) and ROCK-0 (shading). (b) linear regression of the zonal wind from all ROCK experiments on the PJS index. Contours are the full field from the ROCK-0 (contours start from 250K and increase with a step of 10K). Stippling shows regions where the values are statistically significant (two-tailed t-test, α=0.05).

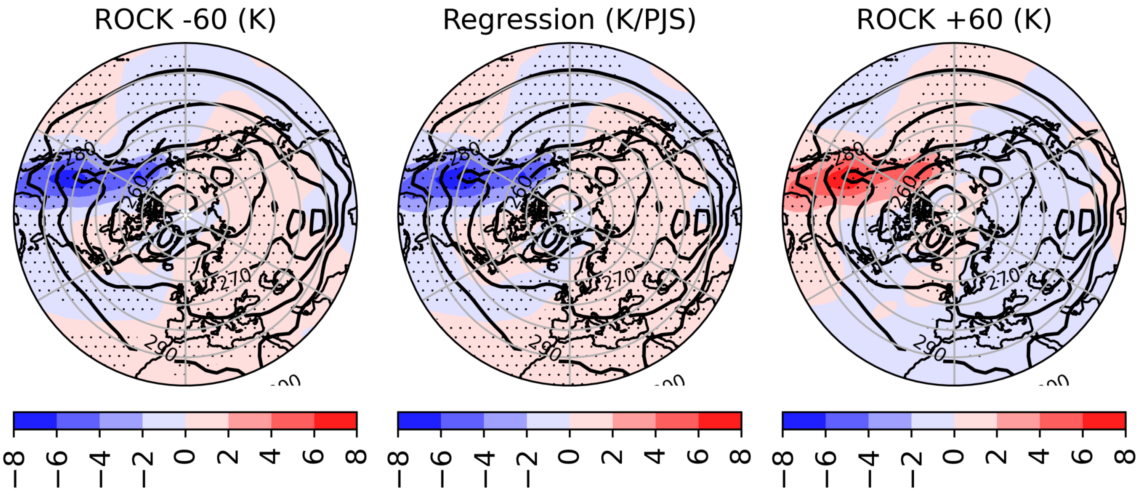
ROCK -60 (K)
Regression (K/PJS)
ROCK +60 (K)
280
260
270
290
−8
−6
−4
−2
0
2
4
6
8

Figure 4.15: as Fig.4.14 but without the temperature signal associated with changes in orography (i.e., height change multiplied by the reference lapse rate).

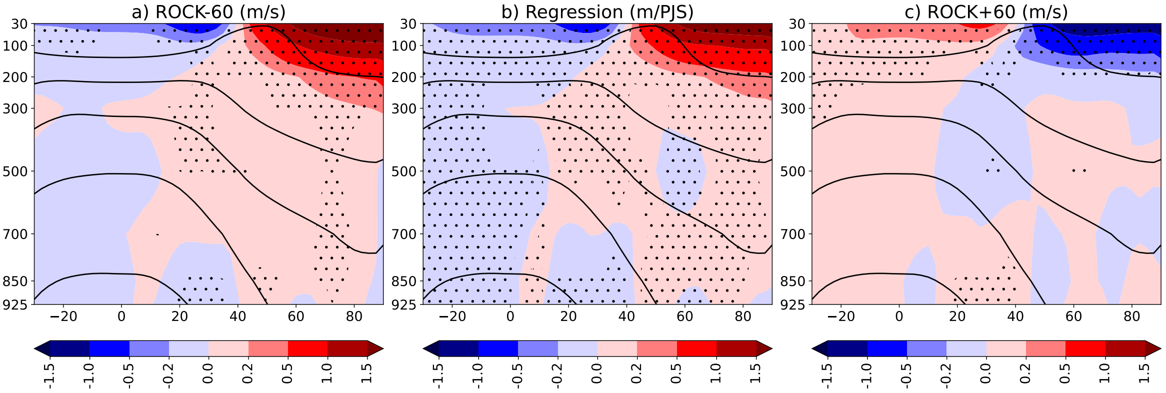

Figure 4.16: DJF zonal air temperature cross section (K). (a,c) Differences between the modified orography experiments (ROCK-60 and ROCK+60) and ROCK-0 (shading). (b) linear regression of the geopotential height from all ROCK experiments on the PJS index. Contours are the full field from the ROCK-0 (the step is K). Stippling shows regions where the values are statistically significant (two-tailed t-test, α=0.05).

Mountains, Fig4.16c, shows the absence of any signal in the lower troposphere. Conversely, the stratosphere shows a positive anomaly going from the Equator to 40N and a negative anomaly from 40N to the Northern Pole.

The regression of the temperature on the PJS index, Fig.4.16b, shows an increase of the stratospheric temperature with high values of the PJS index (i.e. stronger Pacific jet) at subtropical regions. The effect is reversed for higher latitudes where, with a stronger jet, the stratospheric temperature increases.

Eddy height

The Eddy height (or stationary waves) indicates the deviation from the zonal mean (or Eddy component) of the geopotential height:

$$Z^* = \overline{Z} - [\overline{Z}]. \tag{4.1}$$

The square brackets indicate the zonal average and the top line the time average.

Figure 4.17 shows the Eddy height at 500hPa. The black contours, obtained from the control run, show the typical pattern of Eddy height. The Anticyclonic region over the North American continent, from now on referred to as the Rocky ridge, shows the larger effect of the Rocky Mountains. Figure 4.17a shows a reduction of Eddy Height at high latitudes and an increase of the Eddy Height at lower latitudes, this can be interpreted as a southward shift of the Rocky ridge with a reduced height of the Rocky mountains. Figure 4.17c, the experiment with the height of the Rocky mountains increased, shows an opposite behaviour. The amplitude of the Rocky ridge increases at higher latitudes and decreases at lower latitudes.

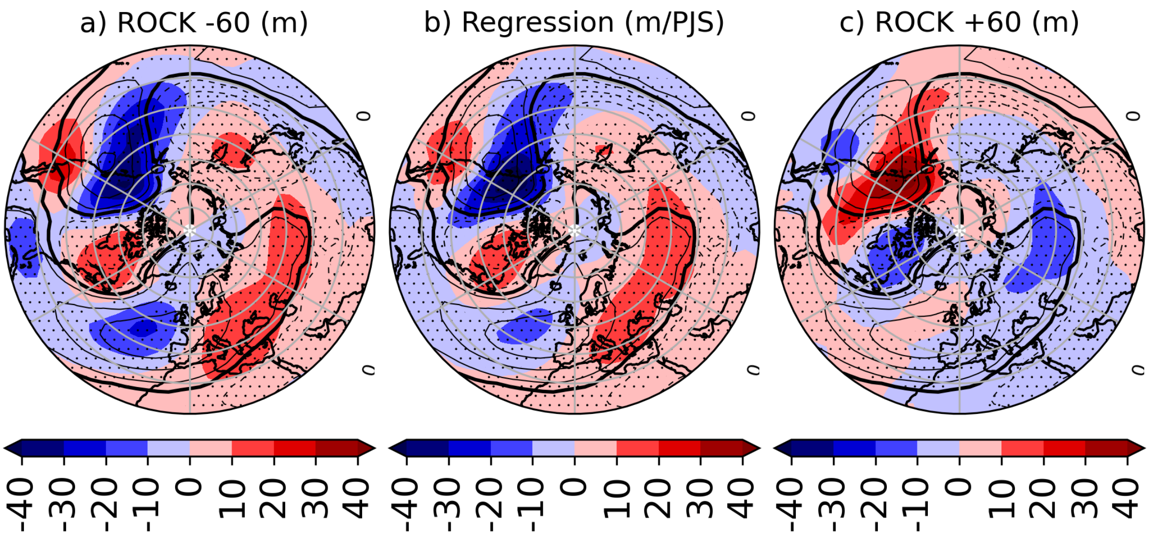

Figure 4.17: DJF eddy height (m) at 500hPa. (a,c) Differences between the modified orography experiments (ROCK-60 and ROCK+60) and ROCK-0 (shading). (b) linear regression of the geopotential height from all ROCK experiments on the PJS index. Contours are the full field from the ROCK-0 (the step is m/s). Stippling shows regions where the values are statistically significant (two-tailed t-test, α=0.05).

Moving eastward, the control experiment shows a negative center of action, over the Hudson Bay. The reduction of the height of the Rocky mountains decreases the intensity of the anticyclonic center of action. On the contrary, an increase of the height of the mountains leads to a stronger cyclonic region. Over the North Atlantic and the Euro-Asiatic sector the stationary wave pattern is characterized by a positive center of action, associated with the Azore high. Figure 4.17a shows a decrease of the intensity on the westward branch of the anticyclonic center of action and an increase on the eastward branch. This configuration can be associated with an eastward shift of the center of action from the ocean to the continent. The figure showing the experiment with increased height for the Rocky Mountains exhibits only a reduction of the intensity of the anticyclonic center of action on the Euro-Asiatic sector. In summary (Fig.4.17b, regression of the Eddy height on the PJS index), as the strength of the Pacific jet increases the Eddy height pattern changes as well. The Rocky Ridge is less anticyclonic at higher latitudes and more anticyclonic at lower latitudes. The cyclonic region on the Hudson bay becomes less cyclonic. The Azore high, shifting from west to east, reduces its intensity over the ocean and increases its intensity over the land.

The Eddy height for the upper troposphere, 100hPa, is shown in Figure 4.18. At this level, the stationary wave pattern starts its transition from wavenumber two to wavenumber one (Nigam and De Weaver, 2015[84]). The black contours of the figure show the Eddy height full field for the ROCK-0 experiment. Two positive anomalies are located over the Pacific and Atlantic oceans and two negative anomalies, one large and the other smaller, are located over the continents. The colours in Fig.4.18a show the response to a reduction of the height

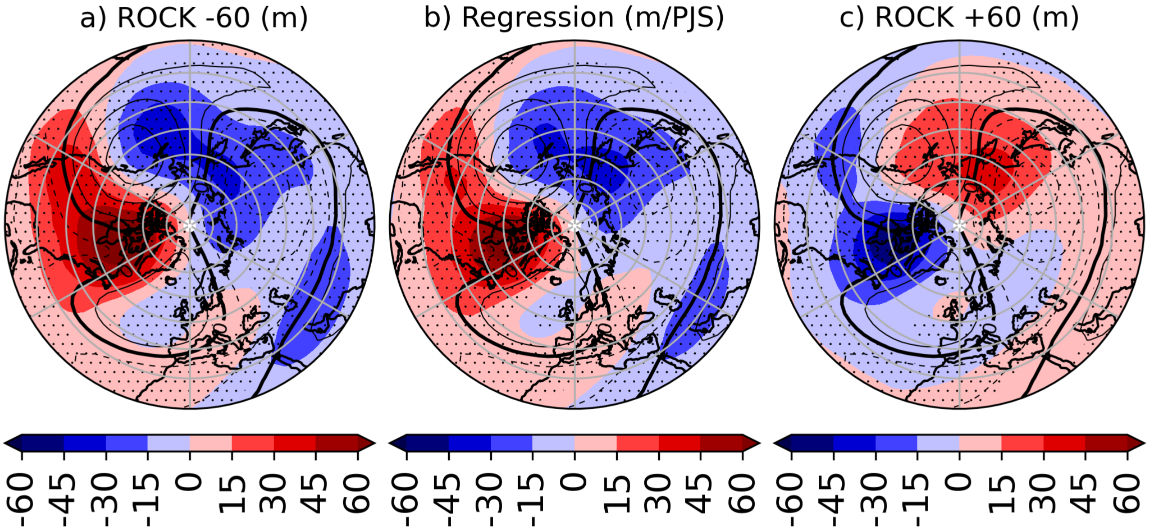

Figure 4.18: as Fig.4.17, but for eddy height at 100hPa (m).

of the Rocky Mountains. The cyclonic region over the North American region is overcome by the effect of the orography, the sign of the Eddy height changes becoming positive. At the same time, the positive signal over the Atlantic Ocean is slightly weaker. Over the Pacific Ocean and Asia, the reduction of the height of the Rocky mountain leads to a deepening of the cyclonic center of action over the continent and a reduction of the anticyclonic center of action over the ocean. Fig.4.18c shows the difference between ROCK+60 and ROCK-0. Increasing the height of the Rocky mountains the cyclonic center of action over North America deepens and becomes more defined. The anticyclonic center of action over the Pacific ocean shifts to the west and the center of action over Asia becomes a little weaker. Lastly, the anticyclonic center of action over the Atlantic Ocean does not change.

The linear regression of the experiments on the PJS index (Fig.4.18b) confirms the results. With a stronger Pacific jet stream, the low over North America disappears and the two signals over the oceans tend to merge together. On the other hand, the negative center of action over Asia becomes larger and moves eastward.

4.2.2 Rossby stationary wavenumber

The turning latitude of Rossby stationary waves (see 2 for the definition) can be computed from the meridional profile of Ks. Given a meridional profile of $K_s(\phi)$ and a stationary Rossby wave characterized by a zonal wavenumber n, the turning latitude is the latitude where the function $K_s(\phi)$ crosses the vertical line n=const. In our case, the meridional profile of the stationary wavenumber is calculated by zonally averaging the zonal wind over the Pacific sector (170W-110W) 604 and considering only the Northern Hemisphere (10N-70N). The longitudinal size of the 605 Pacific sector is comparable with the typical scale of quasi-

stationary Rossby waves 606 (Scaife et al. 2017[96]).
Figure 4.19 shows the meridional profile for each ROCK experiment and for the ERA-Interim: Red curves refer to ROCK experiments with increased Rocky Mountains height, blue curves refer to ROCK experiments with reduced height, the solid black line corresponds to the ROCK-0 experiment, while the dashed black line indicates the ERA-Interim reanalysis. For wavenumbers greater than 4 the ERA-Interim reanalysis shows a constantly lower turning latitude than ROCK experiments. For values between 3 and 4, the range of values computed from the ROCK experiments is comparable with the reanalysis values. Nonetheless, the meridional profile is different, and none of the SPEEDY experiments is able to represent the reanalysis profile well. For values lower than 3, the spread of the ROCK experiment is reduced and all the simulations satisfactorily follow the profile of ERA-Interim. The experiments with the higher Rocky Mountains, however, are more similar to the reanalysis than those with the Rocky Mountains decreased, possibly because the higher orographic barrier reduces the jet speed, and so it reduces the zonal wind model bias as well. Moreover, in Figure 4.3 it was shown that ERA-Interim has a lower value of the PJL index than the ROCK experiments. The bias in the latitudinal position of the jet stream is related to the bias in the meridional profile of the Rossby stationary wavenumber. Indeed, a jet at lower latitudes implies lower turning latitudes.

4.3 Summary and discussion

ROCK experiments show that, by changing the height of the Rocky Mountains, it is possible to modify substantially the mean state of the SPEEDY model over the North Pacific sector. Indeed, it is shown that changes in the speed of the Pacific jet simulated in the ROCK experiments cover the whole spectrum of the zonal wind-speed bias in state-of-the-art global climate models. In other words, the comparison with the values of the same Pacific Jet indices computed for the CMIP6 models indicates that the SPEEDY experiments are able to mimic the biases in the Pacific jet strength of CMIP6 models (Fig.4.3).
Not many authors have explored the impact of changes in models' orography. Generally, the most used approach is either the complete removal of the orography or the removal of a specific mountain chain (Held 1983[51], Broccoli e Manabe 1992[22],Wills 2015[124], Seager 2002[97], White et al. 2017[119],2018[120], Baldwin et al. 2021[9]). For example, a number of papers studied the role of the Tibetan plateau and the Mongolian mountains (Boos and Kuang 2010[17], Chiang et al. 2015[31], Shi et al. 2016[101], Kong and Chiang 2020[66]) in shaping the large-scale Northern Hemisphere atmospheric circulation. White et al. 2021[121] compared simulations with standard orography and simulations carried out removing completely all the orography. They found out that the orography reduces the mean

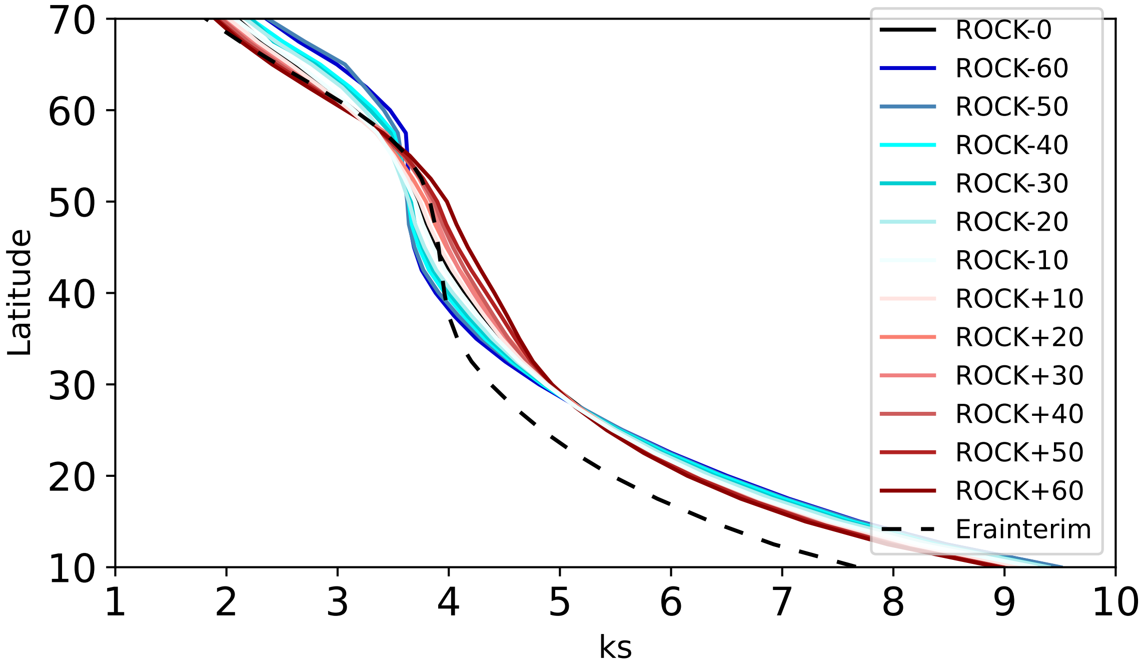

Figure 4.19: DJF meridional profile of Rossby stationary wavenumber at 300 hPa. Ks is calculated by averaging the zonal wind at 300 hPa over a region between 170-110W. The black dashed line represents ERA-Interim, the black line is the ROCK-0 simulation, reds are ROCK experiments with increased orography, and blues ROCK experiments with reduced orography.

zonal wind by 50-80% and, without the orography, the wintertime zonal wind of the Northern Hemisphere is comparable with the Southern Hemisphere winter jet. The resolved orography accounts for about 1/3 of the total slowdown of zonal wind. The ROCK experiments, which showed (e.g. Fig.4.1, Fig.4.5, 4.6 and 4.7) that the height of the Rocky Mountains linearly affects the zonal wind, are consistent with these results.

Results for the geopotential height and eddy height are in accordance with previous works (Seager 2002[97]). By reducing the orography of the Rockies, the trough over the eastern coast of North America is weakened, on the contrary, an increase of the height of the Rocky Mountains strengthens the trough (Fig.4.11, 4.12). The consequences are various. First there is a more zonal flow over North America with lower mountains (Fig.4.5, 4.6, 4.7). The second effect is the weakening of the northerlies over western North America (Fig.4.9,4.10) with associated warming (Fig.4.14). Moreover, the reduced southerlies over eastern North America and the Atlantic Ocean (Fig.4.9,4.10) imply a cooling (Fig.4.14). ROCK experiments also enrich the work of Seager 2002[97] showing that an increase of the orography induces changes in the mean state that are exactly the opposite of the effect of a reduction.

The interaction between wind and the mountains has a profound impact on the precipitation on the North American continent. The Rocky Mountains are located at the exit region of the Pacific Jet stream, and, due to the peculiar conformation of the mountain range, they act as a barrier for the incoming wind. In this way a wet region forms on the windward side of the mountains and a dry region on the leeward side. This effect is generated by the air coming from the ocean, rich in moisture, and forced to rise following the mountain range profile. The moisture condensates during the upward motion and this process generates the wet area on the windward side of the mountain. The air reaching the leeward side of the mountain, deprived of its moisture, is dry and unable to generate precipitations in the inland (Haurwitz and Austin 1944[1], Critchfield 1974[35], Trewartha and Horn 1980[109], Broccoli and Manabe 1992[22], Wills and Schneider 2015[124]). The orography maintains midlatitude dry zones west of troughs of orographically forced stationary Rossby waves. Results from Figure 4.13 show that a lower height of the mountains reduces the drought in continental North America, on the other hand, by increasing the orography, precipitation is reduced.

Chapter 5

ENSO sensitivity experiments

This chapter illustrates the results of the ENSO sensitivity experiments, showing how the Rocky Mountains orography affects the response to idealized El Niño and La Niña anomalies. Results from King et al. (2018[64]) demonstrate that the propagation of ENSO signals from the tropics to the extratropics is more intense during the late winter (January, February and March, JFM), therefore all the results, from the ENSO experiments are shown in the JFM season.

5.1 ENSO results

In order to show the response to an idealized ENSO in the Pacific-Western North American sector, the JFM 500 hPa geopotential height is considered (King et al. 2017[64], Feng et al. 2017[43], Alexander et al. 2008[3]).

Figure 5.1 shows the response to an idealized El Niño in the 500hPa geopotential height for the NINO-0 (Fig.5.1) and ERA-Interim (Fig.5.1a). In the Pacific and the North American sectors, the response in the geopotential height due to the idealized El Niño SST is in good agreement with observations (e.g., Horel and Wallace 1981[57], Bracco et al. 2007[20], Kucharski et al. 2007[67], Rodriguez-Fonseca et al. 2009[92], Kroger and Kucharski 2010[**?**], Bulíc et al. 2012[24], Wang 2017[117], Dogar et al. 2017[38], Mezzina et al. 2020[79]). The NINO-0 response shows a strong negative anomaly in the Pacific Ocean (120E-120W, 30-50N) and a positive anomaly over the North American continent (180-110W, 50-80N). These two anomalies, combined with the (weaker) negative anomaly over Mexico, constitute the typical Rossby wave train associated with ENSO. Another negative anomaly is found over Greenland.

The response to an idealized La Niña (NINA-0 experiment, Fig.5.2) shows a signal characterized by a positive anomaly over the Pacific Ocean, a negative anomaly over the North American continent and a positive anomaly over Mexico, consistent with the Rossby wave

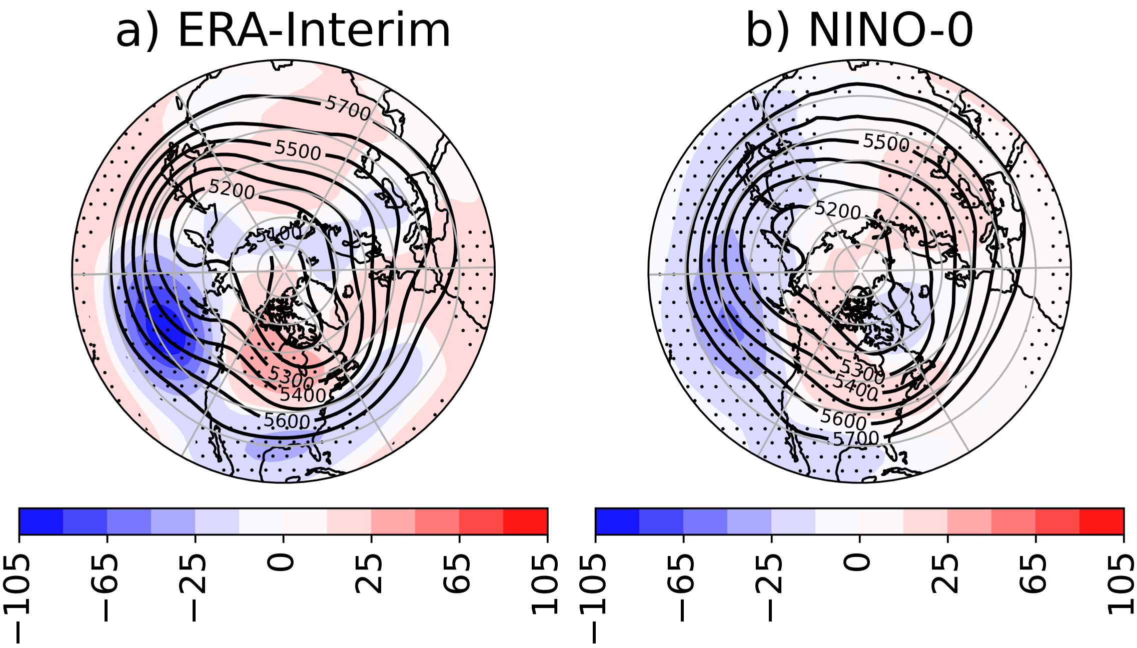

Figure 5.1: JFM response to El Niño in geopotential height at 500 hPa for ERA-Interim (a) and SPEEDY (NINO-0 minus ROCK-0,b). Contours are the respective climatological geopotential height and colours are the responses to El Niño. Stippling shows regions where the signals are statistically significant (two tailed t-test, α=0.05)

train for La Niña. The NINA-0 experiment also shows a significant positive signal over the Atlantic Ocean.

Overall the NINO-0 run shows a westward displaced Rossby wave train and weaker positive pole when compared to ERA-Interim. It is worth noting that the observed North Atlantic pole of the Rossby wave train is missing in the NINO-0 experiment, suggesting a weaker atmospheric bridge between the two basins in SPEEDY. However, over Europe and the Middle East, the reanalysis and the NINO-0 experiment show similar patterns; both show a positive anomaly of about 10m. Conversely, Eastern Asia and Japan are regions where the NINO-0 experiment and ERA-Interim are more in contrast: in the NINO-0 experiment, the negative anomaly in the Pacific Ocean elongates westward till reaching Japan and the coasts of Asia, while in ERA-Interim a positive anomaly over Asia and Japan is observed. Considering the idealized framework of the NINO experiments, a discrepancy between SPEEDY and ERA-Interim is expected. Nonetheless, the overall response is in satisfactory agreement with respect to the reanalysis.

The NINA-0 experiment, compared with ERA-Interim, shows an overall weaker signal with respect to ERA-Interim (Fig.5.2). In SPEEDY, the Rossby wave train, starting from the Pacific Ocean and crossing the North American continent is roughly the half of the signal observed in the reanalysis. The only exception is the positive pole over Mexico, which is comparable with ERA-Interim. The positive centre of action on the Pacific Ocean is shifted

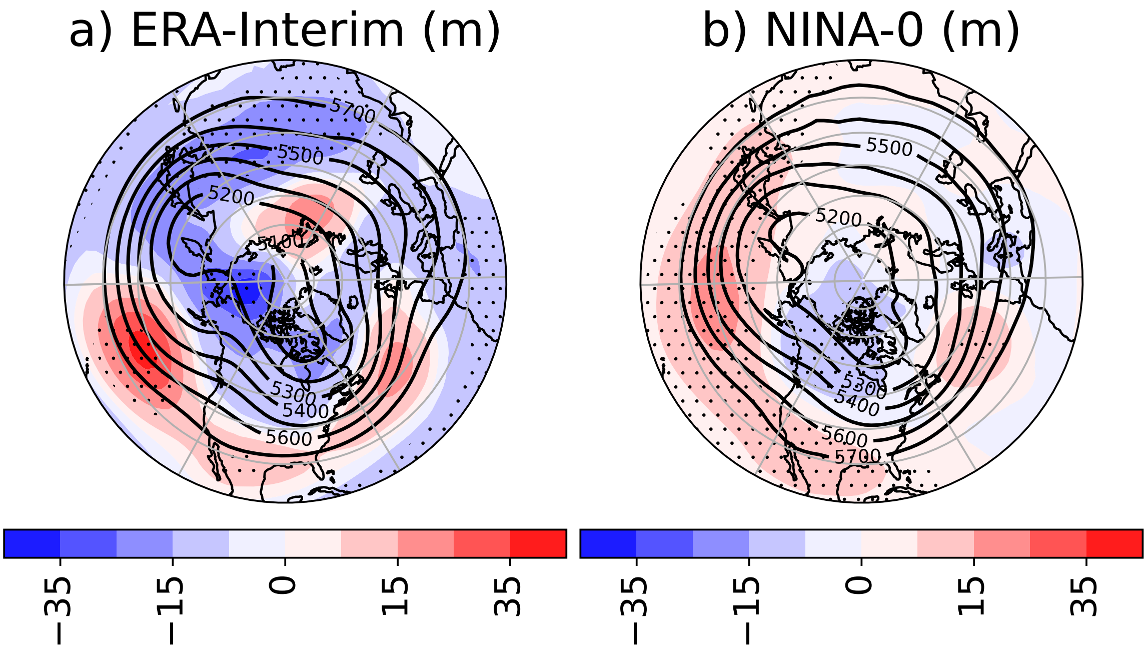

Figure 5.2: JFM response to La Niña in geopotential height at 500 hPa for ERA-Interim (a) and SPEEDY (NINA-0 minus ROCK-0, shadings) and ERA-Interim (contours). Contours are the climatological geopotential height and colours are the responses to El Niño. Stippling shows regions where the SPEEDY signals are statistically significant (two-tailed t-test, α=0.05).

to the west with respect to the reanalysis and covers all the ocean up to Japan.

The asymmetry of the signals between El Niño and La Niña are caused by the different impact that imposing a warm or cold SST anomaly on the climatological SST might have. Indeed, small warm SST anomalies over the tropical western Pacific can enhance convection and induce large rainfall anomalies. Conversely, for cold SST anomalies over the tropical eastern Pacific, strong SST anomalies are required to induce the convective anomalies (Timmermann et al. 2018[107]).

In order to better highlight the effect of the mean state on ENSO response, all the results are presented as the difference between the ENSO sensitivity experiment and the relative ROCK baseline counterpart (for example, NINO-0 minus ROCK-0; NINO-60 minus ROCK-60 ; NINO+60 minus ROCK+60 . . . and so on).

5.1.1 ENSO response: teleconnection

To study the relationship between the model bias and the ENSO response in the different NINO (NINA) and NINOx2 (NINAx2) experiments, the properties of the geopotential height dipole over the Pacific Ocean and North America (i.e., the ENSO Rossby wave train) are investigated.

This is done, for each experiment, by looking at the geographical position of the maximum

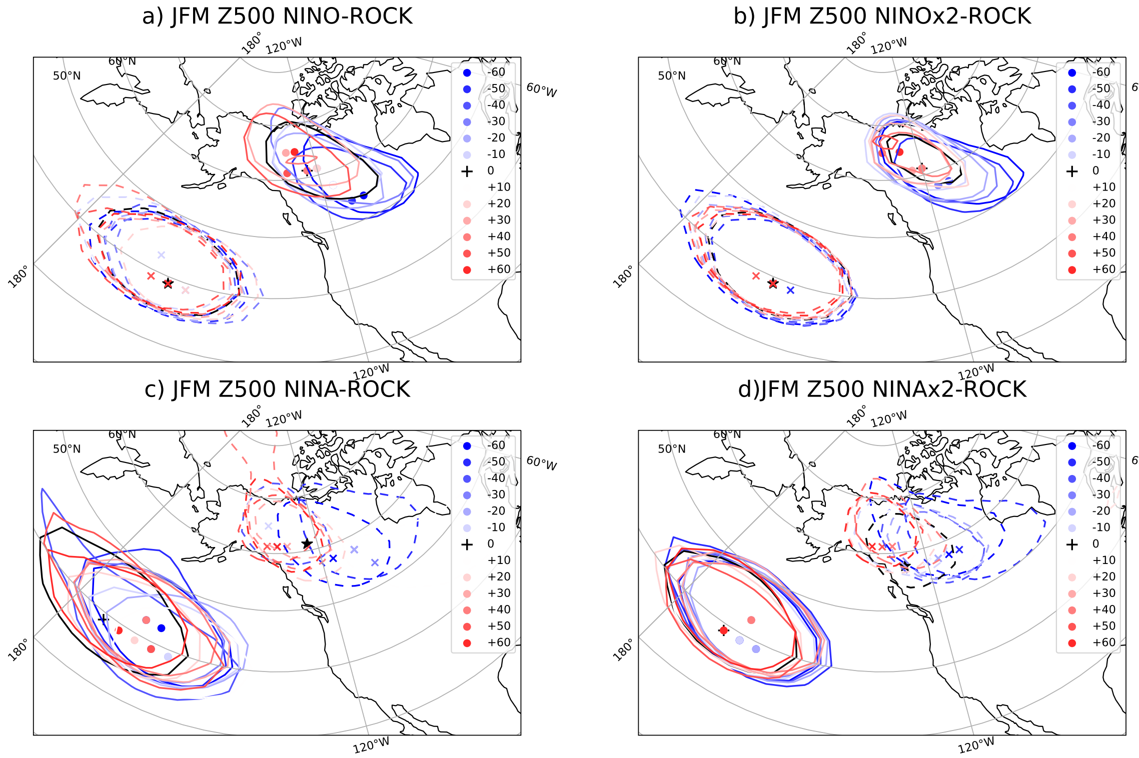

Figure 5.3: JFM dipole response to ENSO in the geopotential height at 500 hPa for (a) for NINO-ROCK experiments (b) for NINOx2-ROCK experiments, (c) for NINA-ROCK experiments, and (d) for NINAx2-ROCK experiments. Only one contour for the North Pacific anomaly and only one for North America anomaly are drawn. Contours are chosen arbitrarily in order to highlight displacement of the anomaly. Dots show the positions of the maximum positive response and crosses the position of the minimum negative response. The value for the anomaly over the North American continent for the NINA experiments is about -9m, while the same for NINO reaches 15m. Similarly, NINAx2 shows a maximum signal of about -17m, while NINOx2 gets up to 30m.

(minimum) over the North America and the North Pacific poles (i.e., in the case of an El Niño response anomaly, this corresponds to a positive pole over North America and a negative pole over the North Pacific). Results are shown in Fig.5.3, while the position of the signal over the ocean is weakly affected by orographic changes, the position of the signal over North America (see dots for El Niño and crosses for La Niña) migrates along a south-east/north-west axis as long as the height of the Rockies is increased.

Although a significant change is seen for the position, the intensity of the ENSO Rossby wave train is not affected by the height of orography. The magnitude of the signal doubles when the intensity of the forcing is doubled (e.g., NINO vs NINOx2). On the other hand, a strong nonlinearity in the ENSO teleconnection is observed when NINO and NINA experiments are compared. The El Niño signal is almost twice the intensity of its La Niña counterpart.

A graphical summary of these results is provided by Fig.5.4, where the latitude, longitude, and intensity of the maximum (minimum) of the geopotential height at 500hPa over North

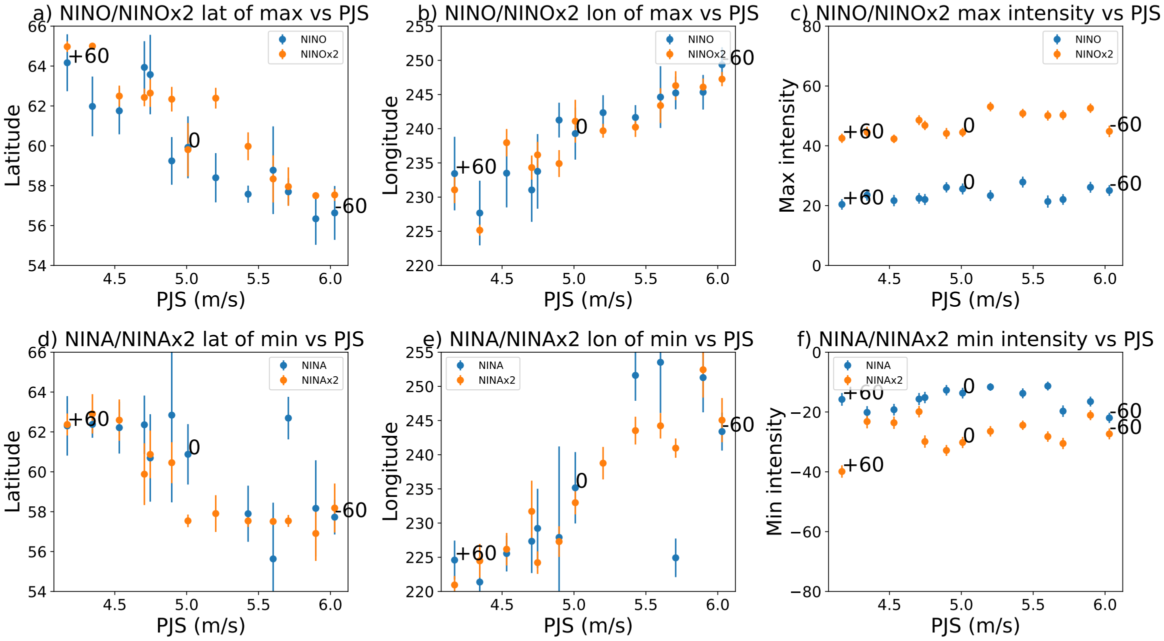

Figure 5.4: JFM 500 hPa geopotential height response to NINO, NINA, NINOx2, and NINAx2 for all ROCK experiments. (a) NINO and NINOx2 latitude of the maximum of the response. (b) NINO and NINOx2 longitude of the maximum of the response. (c) NINO and NINOx2 geopotential height intensity of the maximum of the response. (d,e,f) are the same as (a,b,c) but for the minimum of the response in NINA and NINAx2 experiments. In all the panels the mean is represented by a dot and the standard deviation by the vertical bars.

America for all the idealized ENSO NINO (NINA) and NINOx2 (NINAx2) experiments are shown.

In order to provide an estimate of the uncertainty in the position of the maxima/minima over the North America region due to internal variability, a bootstrap method is used. From the 200-year simulation, 130 JFM seasons (63% of the data, as suggested by Efron and Tibshirani 1993[105],1994[40]) are randomly chosen and averaged. Then the position of the maxima/minima of the geopotential height at 500 hPa in the box [45N-70N, 150W-90W] is computed. The sampling is repeated 3000 times. In this way, it is possible to estimate the uncertainty of the position of the maximum/minimum, denoted in the figure by the extension of the bars, which shows the standard deviation of the bootstrap sample. By increasing the intensity of the Pacific jet (i.e. by reducing the height of the Rockies) the center of action of the response over North America moves from north-west to south-east (Fig.5.4a,b,d,e). On the other hand, the intensity of the North American response does not change as the intensity of the Pacific jet increases (Fig.5.4c,f). Results are consistent for all sets of NINO, NINOx2, NINA and NINAx2 experiments. However, a minor difference can be noted: the standard deviation of the position (for both the longitude and latitude) of the positive PNA pole decreases when the intensity of the idealised El Niño anomaly is doubled. This suggests that, not surprisingly, a stronger forcing provides a larger signal-to-noise ratio.

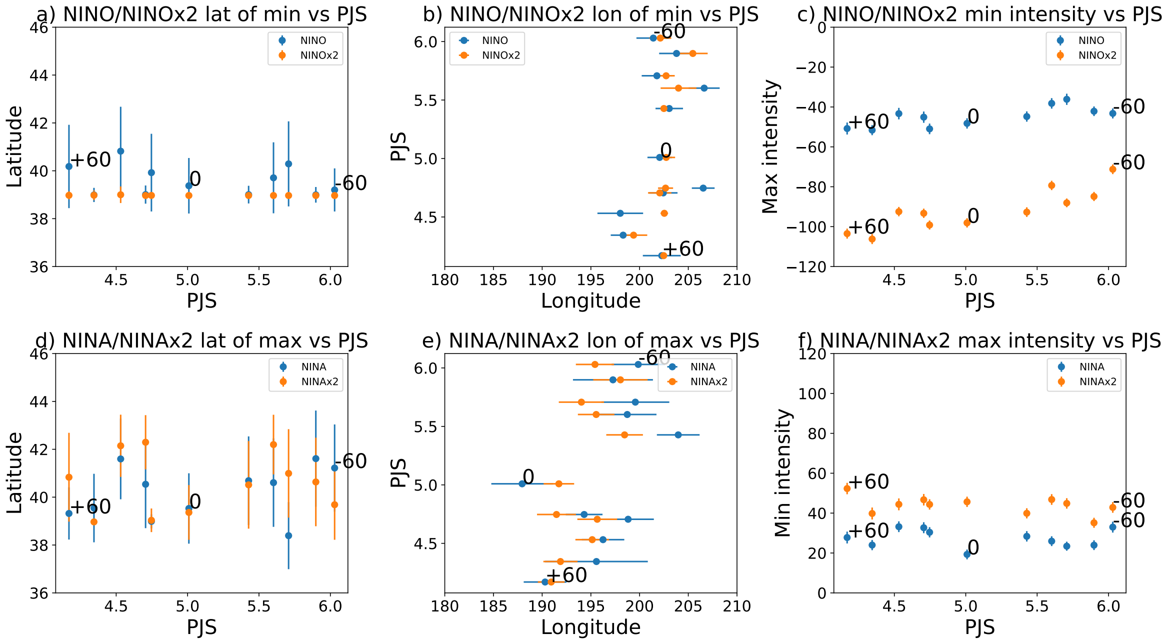

Figure 5.5: JFM 500 hPa geopotential height response to NINO, NINA, NINOx2, and NINAx2 for all ROCK experiments as a function of the PJS index calculated at 850 hPa. (a) NINO and NINOx2 latitude of the maximum of the response. (b) NINO and NINOx2 longitude of the maximum of the response. NINO and NINOx2 geopotential height intensity of the minimum of the response. (d,e,f) are the same as (a,b,c) but for the maximum of the response in NINA and NINAx2 experiments. In all the panels the mean is represented by a dot and the standard deviation by the bars.

The same bootstrap approach is applied to the signal over the Pacific Ocean (Fig.5.5). When looking at the position of the pole over the ocean of the ENSO Rossby wave train, it is found that there is no significant shift in its latitudinal and longitudinal position and the intensity of the anomaly doesn't change.

5.2 ENSO response: impacts

To better assess the sensitivity of the ENSO-induced teleconnection patterns to the model mean state, the responses of near-surface air temperature and total precipitation are analyzed (Fig.5.6 Almost the same patterns - but with doubled amplitude - are obtained from NINOx2 experiments (5.7). Conversely, NINA and NINAx2 experiments show approximately opposite impacts (5.8 and 5.9).

The Northern Hemisphere near-surface air temperature response (Fig.5.6a,c) shows that El Niño has wide but moderate impacts all over the Northern Hemisphere, with near-surface air temperature changes not larger than +/- 0.5K. The only region where El Niño has a stronger signal is Western North America. A clear warm signal is present over Alaska and Canada,

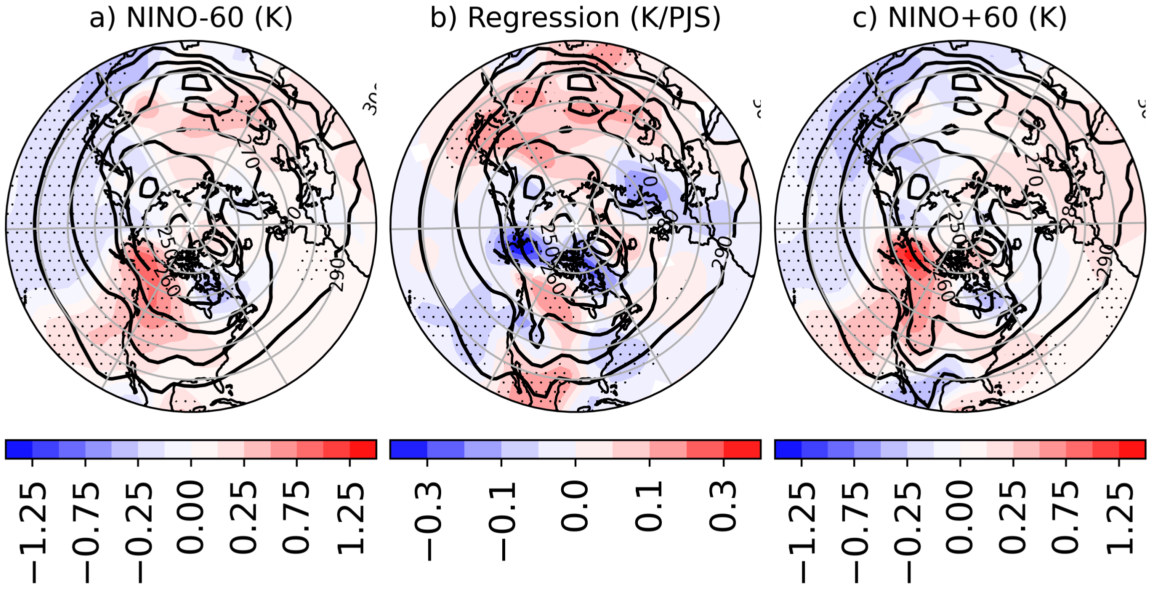
a) NINO-60 (K)
b) Regression (K/PJS)
c) NINO+60 (K)
250
260
270
280
290
−1.25
−0.75
−0.25
0.00
0.25
0.75
1.25
−0.3
−0.1
0.0
0.1
0.3
−1.25
−0.75
−0.25
0.00
0.25
0.75
1.25

Figure 5.6: JFM near surface air temperature response in NINO experiments (NINO - ROCK). (b) Linear regression between the near surface air temperature and the PJS index. (a,c) Two examples of the changes in the response to El Niño (NINO-60 and NINO+60). Stipplings show regions where the values are significant (FDR, $a_{global} = 0.20$, Wilks, 2006[123]). Contours show the near surface air temperature of the relative baseline experiments: (a) ROCK-60 , (b) ROCK-0 and (c) ROCK+60.

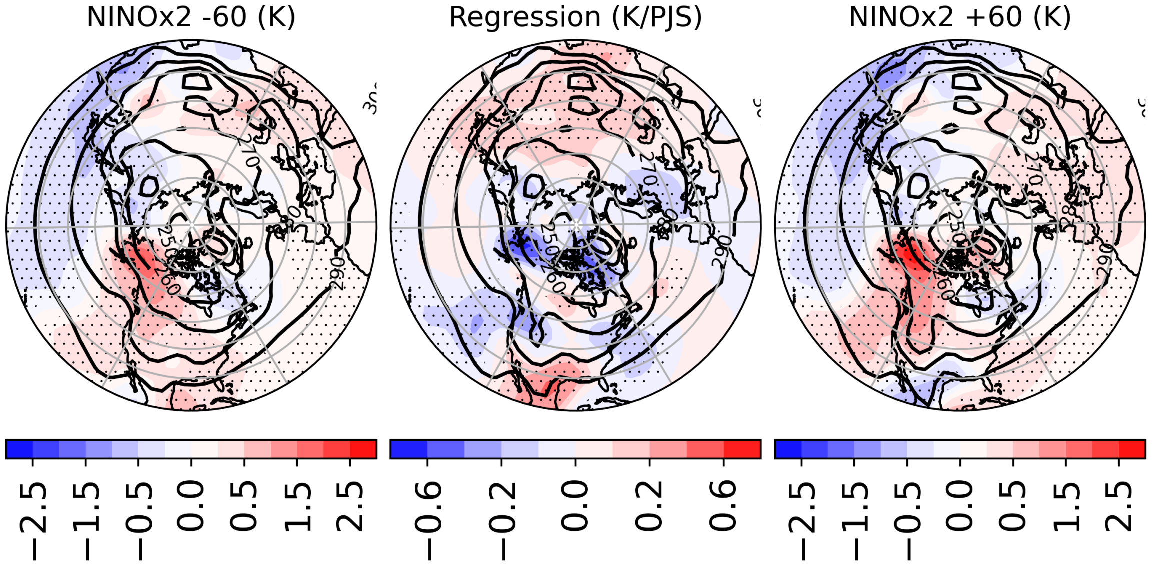
NINOx2 -60 (K)
Regression (K/PJS)
NINOx2 +60 (K)
250
260
270
280
290
−2.5
−1.5
−0.5
0.0
0.5
1.5
2.5
−0.6
−0.2
0.0
0.2
0.6
−2.5
−1.5
−0.5
0.0
0.5
1.5
2.5

Figure 5.7: as Fig.5.6 but for the NINOx2 experiments.

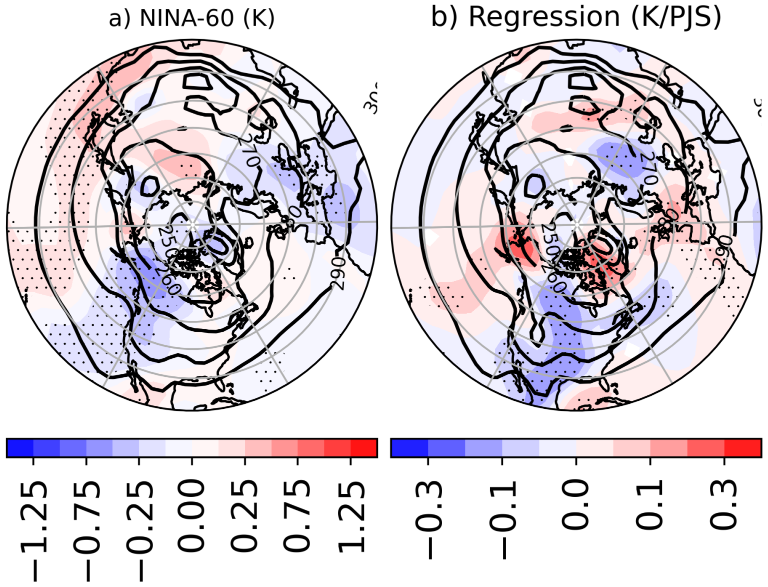
a) NINA-60 (K)
b) Regression (K/PJS)
c) NINA +60 (K)
270
250
260
290
280
−1.25 −0.75 −0.25 0.00 0.25 0.75 1.25
−0.3 −0.1 0.0 0.1 0.3
−1.25 −0.75 −0.25 0.00 0.25 0.75 1.25

Figure 5.8: as Fig.5.6 but for the NINA experiments.

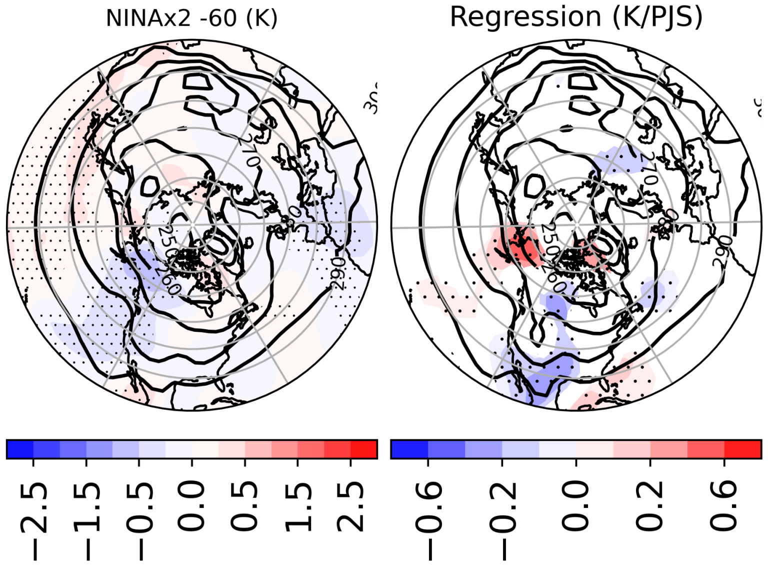
NINAx2 -60 (K)
Regression (K/PJS)
NINAx2 +60 (K)
270
250
260
290
280
−2.5 −1.5 −0.5 0.0 0.5 1.5 2.5
−0.6 −0.2 0.0 0.2 0.6
−2.5 −1.5 −0.5 0.0 0.5 1.5 2.5

Figure 5.9: as Fig.5.6 but for the NINAx2 experiments.

where the near-surface air temperature increases by 1.25K. The same anomaly, reduced in intensity, also extends southward over the West coast of the United States. While experiments with the increased orography (Fig.5.6c) show a negative temperature anomaly over Mexico, those with reduced orography (Fig.5.6a) are characterized by a neutral or positive response. Another clear signal is located over Japan: a cold anomaly spreads downstream, from the Asian East coast to the Pacific Ocean. On the other hand, the signal over Europe, North Africa, and the Arabian Peninsula (a warm anomaly unaffected by changes of the mean state) is weak and becomes statistically significant only in the NINOx2 experiments (Fig.5.7a,c).

The linear regression shown in Fig.5.6b, which shows the relationship between the ENSO near-surface air temperature response and the PJS Index, highlights the role of the changes in the mean state in modifying the ENSO temperature fingerprint. The response over Western Alaska is weakened when the PJS index increases, implying that a stronger jet tends to suppress the warm signal there. Similarly, in Mexico, the cold signal of the response decreases as the PJS index increases, but the sign changes when the PJS index exceeds a threshold value. On the contrary, the positive signal over Canada is enhanced by a stronger Pacific jet. The response over Asia resembles the one over Mexico, but only the responses over Japan and the Middle East seem to be significantly affected by the mean state, and both become colder when the intensity of the jet stream over the Pacific Ocean decreases. To summarize, larger PJS indices (i.e., for stronger jet speeds) strengthen the zonal flow. This leads to a more zonal configuration of the Rossby wave train to the idealized ENSO-like SST anomaly and a reduction of the meridional advection. As a consequence, a reduction in the intensity of the temperature anomaly is observed. The temperature anomaly reduces over most of the Northern Hemisphere. Two minor exceptions, where the temperature anomaly is enhanced, are Canada and the region east of the Caspian Sea.

Figure 5.10 shows the total precipitation response for NINO experiments. As expected, the pattern of precipitation anomaly produced by NINO experiments shows a marked signal over tropical regions. The total precipitation shows the typical equatorial El Niño signal, with an increase in the eastern and central Equatorial Pacific (not shown), while it decreases in tropical and subtropical regions approximately corresponding to the downward branch of the Hadley cell.

A positive rainfall response is also located near the California coast and the Aleutian region, extending further upstream in the Pacific Ocean. A second positive rainfall response is in the Gulf of Mexico, Florida, and Caribbean region, whose signal also extends over Mexico and reaches the eastern tropical Pacific. On the other hand, El Niño favours a decrease in precipitation over India, Southeast Asia, and Japan.

The regression of the total precipitation on the PJS index (Fig.5.10b) shows modulation of the signal following a change in the mean state over multiple regions: the most relevant signal is a dipolar anomaly that involves Caribbeans and Mexico. Over the Caribbean, the total precipitation decreases when the PJS index increases, with NINO experiments showing a

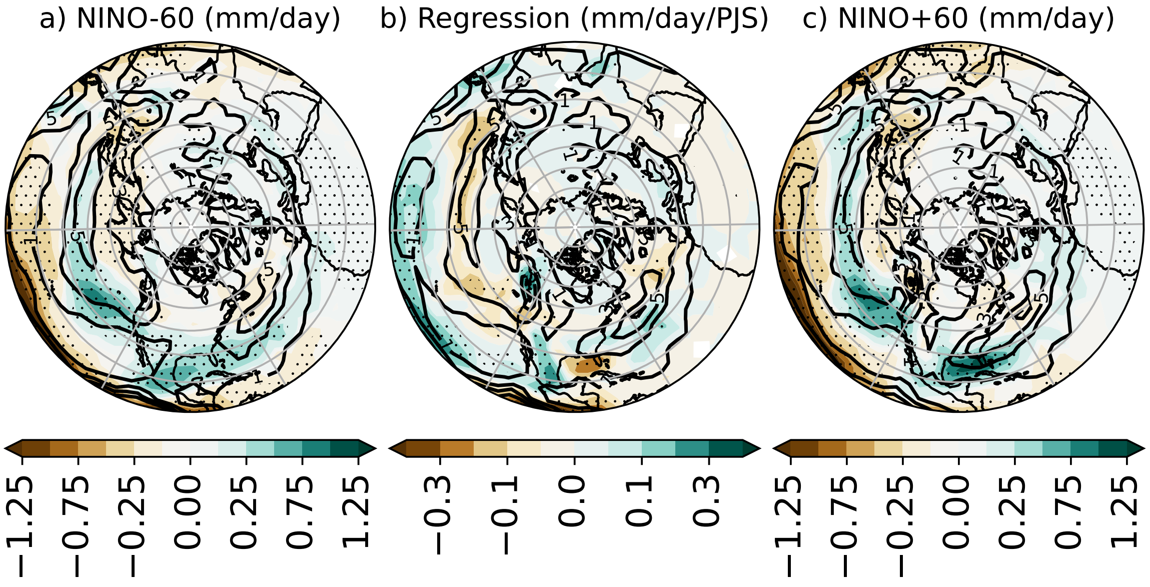
a) NINO-60 (mm/day)
b) Regression (mm/day/PJS)
c) NINO+60 (mm/day)
−1.25 −0.75 −0.25 0.00 0.25 0.75 1.25
−0.3 −0.1 0.0 0.1 0.3
−1.25 −0.75 −0.25 0.00 0.25 0.75 1.25

Figure 5.10: JFM total prexipitation response in NINO experiments (NINO - ROCK). (b) Linear regression between the total precipitation and the PJS index. (a,c) Two examples of the changes in the response to El Niño (NINO-60 and NINO+60). Stipplings show regions where the values are significant (FDR, $a_{global} = 0.20$, Wilks, 2006[123]). Contours show the total precipitation of the relative baseline experiments: (a) ROCK-60 , (b) ROCK-0 and (c) ROCK+60.

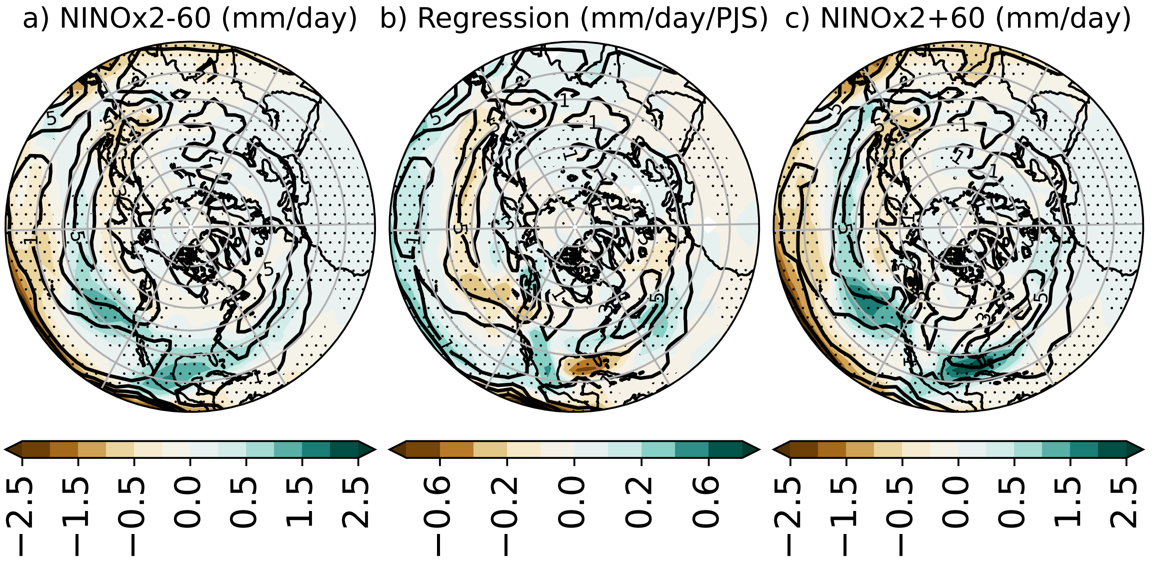
a) NINOx2-60 (mm/day)
b) Regression (mm/day/PJS)
c) NINOx2+60 (mm/day)
−2.5 −1.5 −0.5 0.0 0.5 1.5 2.5
−0.6 −0.2 0.0 0.2 0.6
−2.5 −1.5 −0.5 0.0 0.5 1.5 2.5

Figure 5.11: as Fig.5.10 but for NINOx2 experiments.

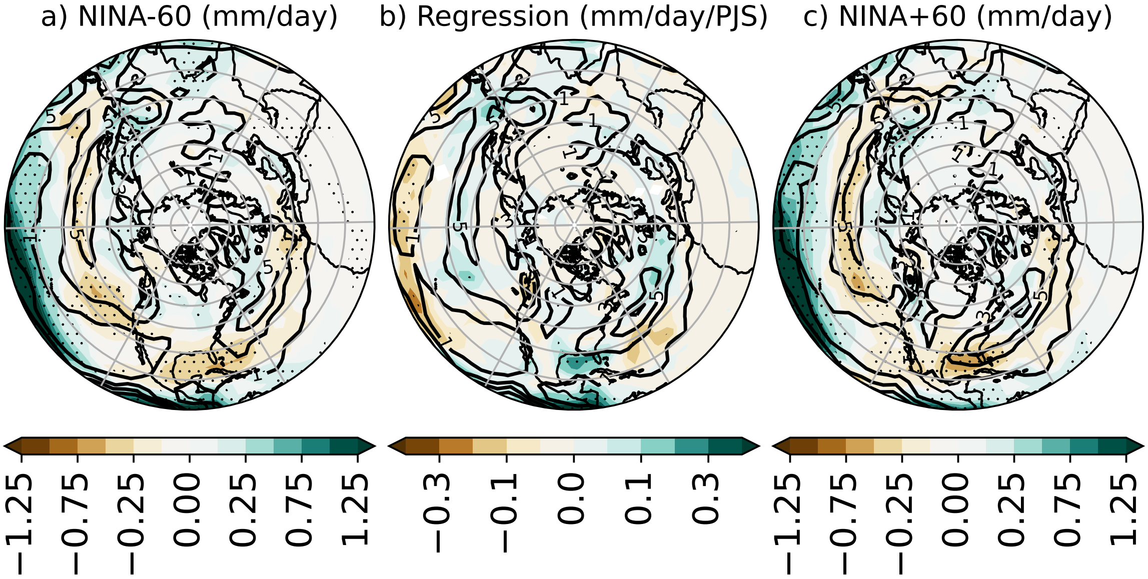
a) NINA-60 (mm/day)
b) Regression (mm/day/PJS)
c) NINA+60 (mm/day)
−1.25
−0.75
−0.25
0.00
0.25
0.75
1.25
−0.3
−0.1
0.0
0.1
0.3
−1.25
−0.75
−0.25
0.00
0.25
0.75
1.25

Figure 5.12: as Fig.5.10 but for NINA experiments.

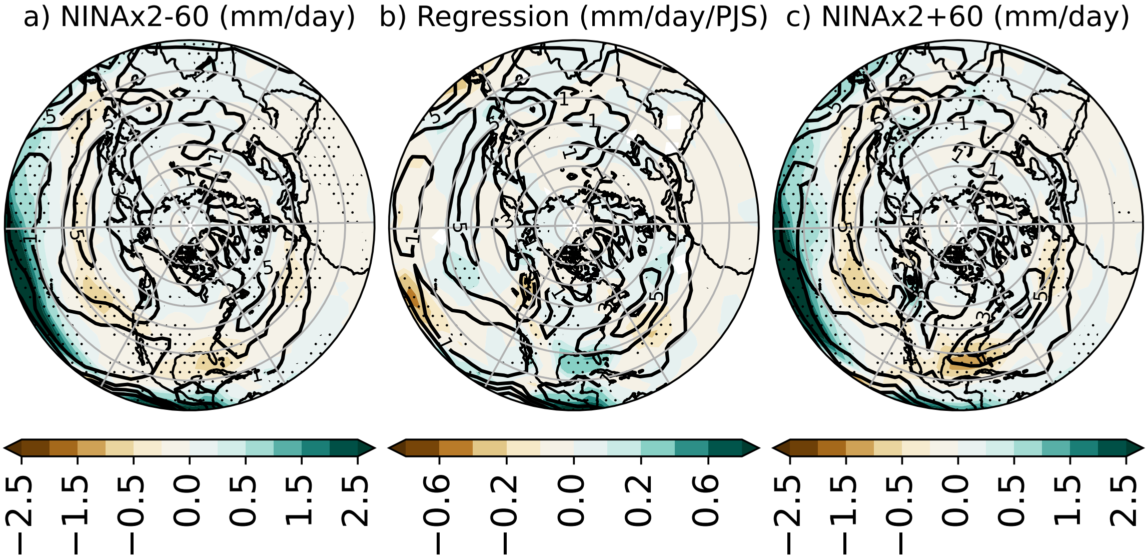
a) NINAx2-60 (mm/day)
b) Regression (mm/day/PJS)
c) NINAx2+60 (mm/day)
−2.5
−1.5
−0.5
0.0
0.5
1.5
2.5
−0.6
−0.2
0.0
0.2
0.6
−2.5
−1.5
−0.5
0.0
0.5
1.5
2.5

Figure 5.13: as Fig.5.10 but for NINAx2 experiments.

stronger relationship between the signal and the PJS index. Conversely, the total precipitation over Mexico increases with the PJS index.

Similarly, the tropical Pacific is strongly affected by the Pacific Jet stream intensity, and the total precipitation regression shows an increase in the precipitation greater than 0.30 mm/day/m/s. The response on the west coast of Canada on the border with Alaska shows an increase of the precipitation associated with an increase of the Pacific Jet intensity, while an opposite signal is observed over the Aleutian low.

5.2.1 ENSO response: Rossby waves propagation and the Rossby stationary wavenumber.

In this subsection we show the sensitivity of the meridional profile of the Rossby stationary wavenumber to ENSO idealised forcing. The results should be compared to those of ROCK experiments, discussed in subsection 4.2.2 (see Fig.4.19, which for sake of comparison is reported here as well in Fig.5.14).

Figure 5.15 shows the meridional profile of the Rossby stationary wavenumber for each NINO experiment and for the ERA-Interim: Red curves refer to NINO experiments with increased Rocky Mountains height, blue curves refer to NINO experiments with reduced height, the solid black line corresponds to the NINO-0 experiment, while the dashed black line to the ERA-Interim reanalysis.

The introduction of an idealized El Niño SST anomaly induces a change of zonal wind with the consequence of a different latitudinal profile of the Rossby wave number. All the curves of NINO experiments are displaced towards higher values of the Rossby wave number. The effect is larger at mid-latitudes for latitude values between 30N and 60N. Here, the meridional profile starts to develop a proper waveguide (the profile has a relative maximum, Hoskins and Ambrizzi, 1993[58]; Ambrizzi and Hoskins, 1995[5]). Outside of this latitudinal band, the displacement is still visible but with a smaller amplitude. Experiments with increased orography display a more defined waveguide structure, showing a more pronounced relative maximum.

The effect of a stronger forcing (NINOx2, Fig.5.16) is the formation of a well-defined waveguide for latitudes between 30N and 60N. A reduction of the height of the Rocky Mountains is less effective on the modulation of the Rossby wavenumber around 50N. At this latitude, corresponding to the maximum of k_s, the spread of blue curves is smaller than that of the red ones.

La Niña experiments (NINA, Fig.5.17) show a flattening of the Rossby wavenumber profile; the distance between different curves, corresponding to different orographic heights, reduces. The experiments with increased orographi are more affected by La Niña, the profile changes more when compered with the reduced orography experiment. The effect is amplified for

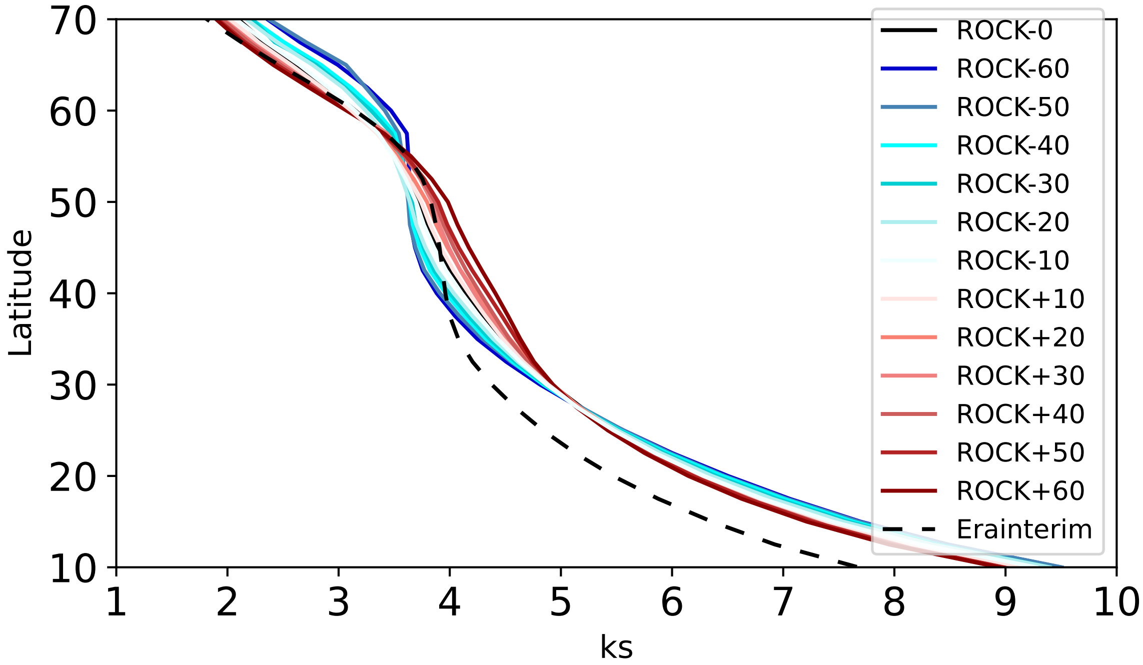

Figure 5.14: DJF meridional profile of Rossby stationary wavenumber at 300 hPa. Ks is calculated by averaging the zonal wind at 300 hPa over a region between 170-110W. The black dashed line represents ERA-Interim, the black line is the ROCK-0 simulation, reds are ROCK experiments with increased orography, and blues ROCK experiments with reduced orography. Same as Fig.16.1.

NINAx2 experiments (Fig.5.18).

It is evident how the turning latitude associated with wavenumbers between 3 and 5, which corresponds to the typical Rossby signal generated by ENSO (Li et al 2020[72]) changes with the height of the Rocky Mountains and consequently with the speed and the position of the Pacific jet. Experiments characterized by a more intense jet stream over the Pacific Ocean (blue lines) show equatorward turning latitudes; experiments with a weaker jet stream show poleward turning latitudes. The changes of the turning latitude values across ROCK experiments are consistent with the observed changes of the position of the ENSO-induced Rossby wave train over North America in NINO/NINA experiments (Fig.5.3); a stronger jet modifies the propagation of Rossby waves reducing the values of the turning latitude and thus inducing a southward shift of the signal in geopotential height. On the other hand, a weaker jet leads to a poleward turning latitude and a consequent poleward shift of the Rossby wave train.

5.3 Summary and discussion

The idealized ENSO sensitivity experiments show that the midlatitude leading response to

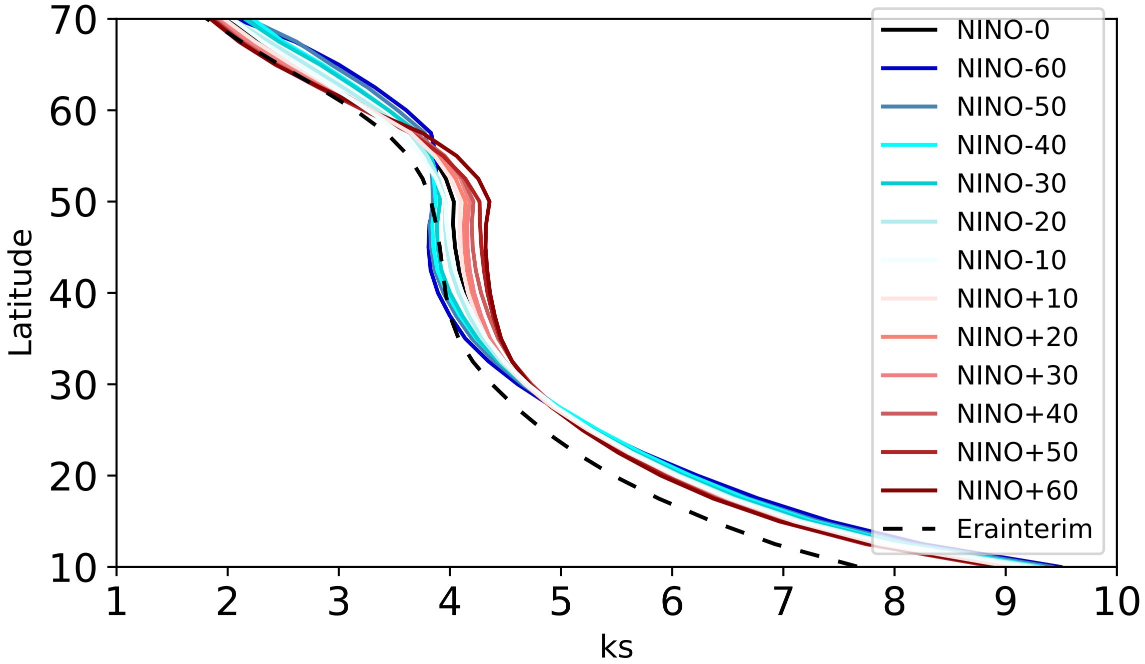

Figure 5.15: JFM meridional profile of Rossby stationary wavenumber at 300 hPa. Ks is calculated by averaging the zonal wind at 300 hPa over a region between 170-110W. The black dashed line represents ERA-Interim, the black line is the ROCK-0 simulation, reds are ROCK experiments with increased orography, and blues ROCK experiments with reduced orography.

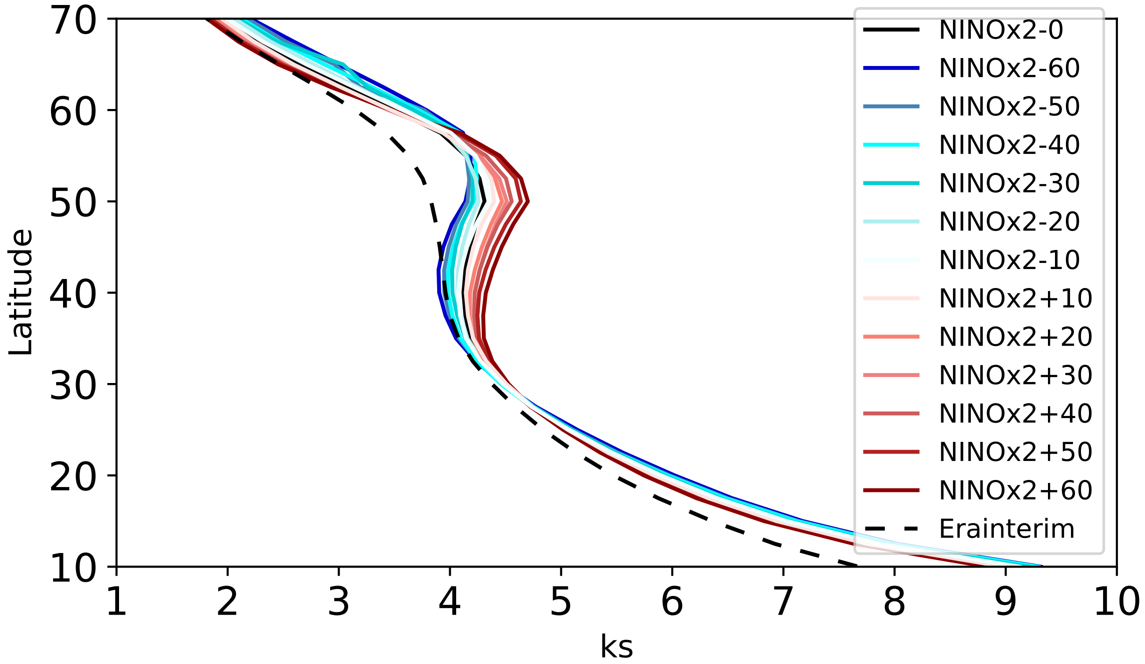

Figure 5.16: as Fig.5.15 but for the NINOx2 experiments.

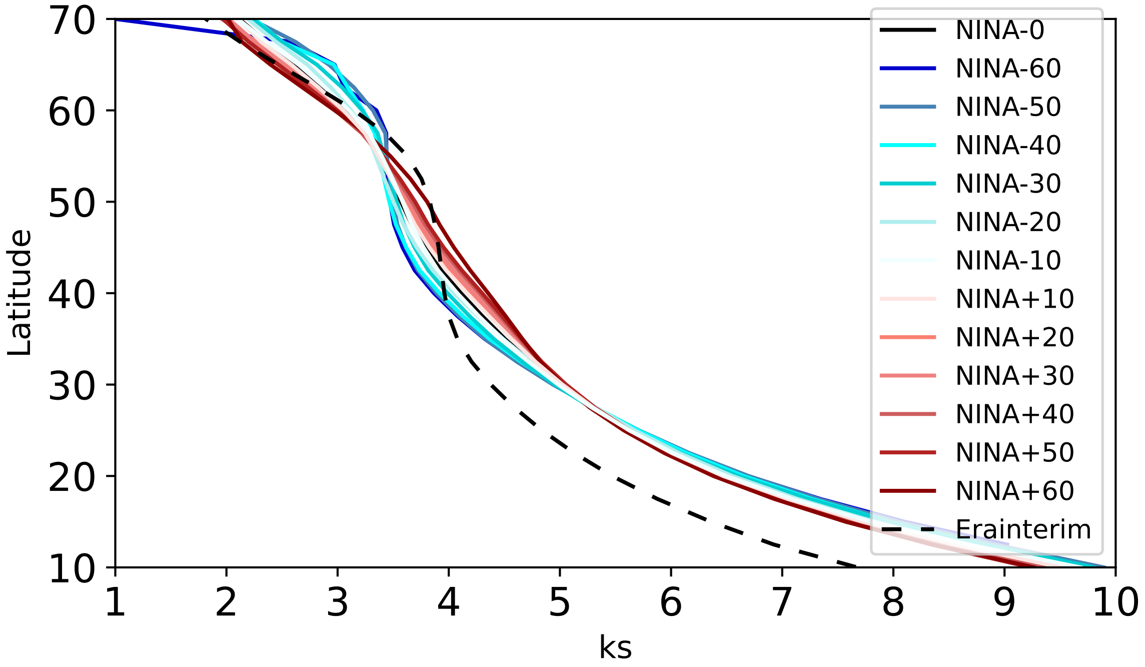

Figure 5.17: as Fig.5.15 but for the NINA experiments.

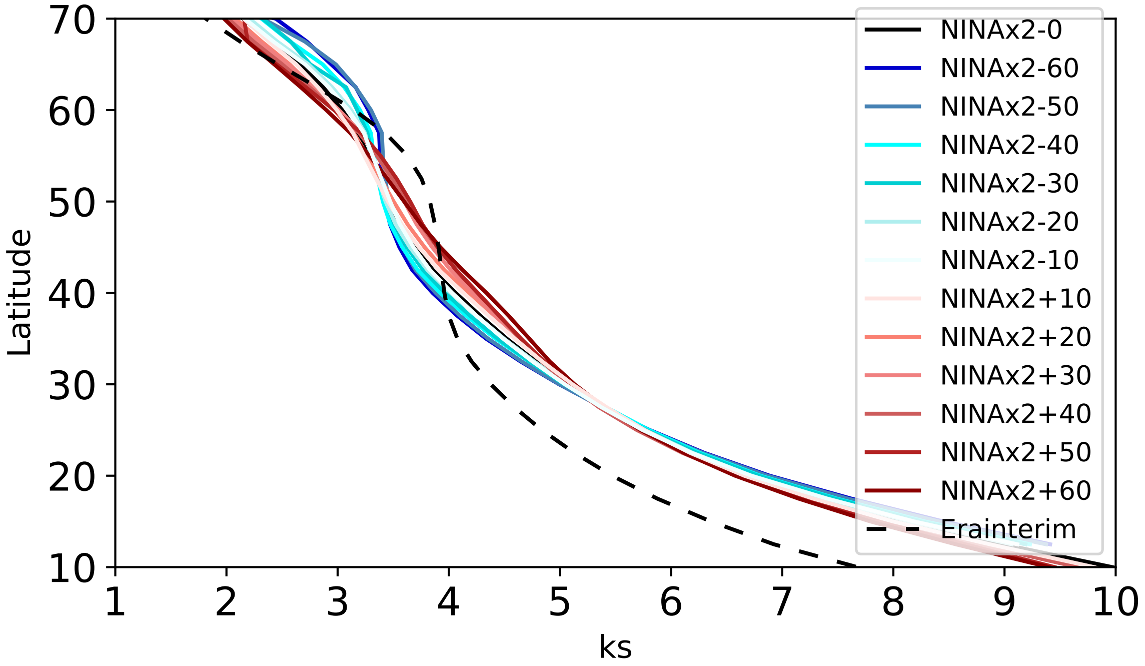

Figure 5.18: as Fig.5.15 but for the NINAx2 experiments.

El Niño is a geopotential height anomaly over the North Pacific and North America, stronger during the late winter and reminiscent of the PNA pattern (King et al. 2018[64]). In the ENSO experiments, the Rossby wave train in response to a tropical El-Niño-like forcing is clearly affected by changes in the mean state. When the Pacific jet is stronger (i.e., when the Rocky Mountains height is reduced), the positive geopotential height response center over Canada and Alaska migrates from north-west to south-east. The position of the center of action of the 500 hPa geopotential height response of the idealized El Niño experiments moves about 4° southward and about 10° longitude eastward following an increase of the jet speed of about 1 m/s. For idealized La Niña experiments, the position of the center of action moves about 2° southward and 14° longitude eastward with an increase of the jet speed of about 1 m/s. Responses to the double intensity idealized El Niño and La Niña experiments are roughly the same as the regular intensity experiments.

The idealized ENSO experiments are similar to experiments carried out in previous works. In particular, Dogar et al. 2017[38] (here on D17) performed four ENSO experiments using the SPEEDY model: two El Niño and two La Niña experiments with regular and doubled intensity respectively.They used an SST anomaly imposed on the climatology, only in the tropical region (50S-50N). Given the very similar structure of this and D17 experiments, a direct comparison is possible. Despite the differences in the ENSO forcing (full Tropical Pacific in D17 and Niño3.4 region in this work), the near-surface temperature in D17 four ENSO experiments is similar. The west coast of the North American continent shows the typical positive (negative) signal related to an El Niño (La Niña) event. The intensities of the near-surface temperature anomalies are comparable to our NINO-0(NINA-0) and NINOx2-0(NINAx2-0) experiments. In D17 the responses in near-surface temperature extend over the Hudson Bay, while in our experiments the anomalies are confined in the west of Hudson Bay. These differences highlight the importance of the SST in the Tropical Pacific outside of the Niño3.4 region. The Extratropical North Pacific Ocean shows a very consistent response in the two works. The spatial pattern and intensity of the total precipitation response found in our experiments match well D17 results.

The schematic shown in Figure 5.19 summarises the mechanism behind the modulation of the ENSO signal by orography over North America. An increased orography (panel a) reduces the intensity of the Pacific jet in the exit region over the continent. The reduction of the zonal component of the wind is associated with an increased meridional component of the wind and more advection of warm air from the tropics to mid-latitudes. This can be interpreted as the air having not enough kinetic energy to go over the orographic barrier, and being deviated poleward. Lastly, the high-pressure anomaly (due to El Niño) is displaced to the North-West. On the other hand, a reduced orography (panel b) increases the jet strength in the exit region and reduces the meridional component of the wind, resulting in a more zonal jet. Consequently, the meridional advection is reduced so that less warm air reaches the higher latitudes. The positive center of action over the continent migrates to the South-East.

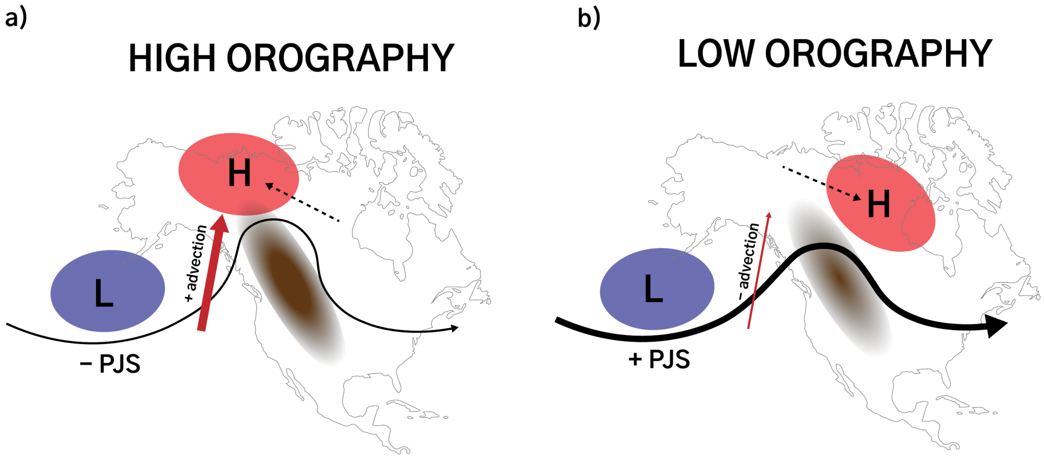

Figure 5.19: Schematic representation of the impact of the orography on the ENSO response.

The results and the interpretation of the link between the ENSO response over the North American continent and the atmospheric mean state (i.e. the zonal wind) proposed in this work are supported by Benassi et al. (2021[11]). They explore the impact of low-frequency SST variability over the extratropical Pacific on the El Niño teleconnection, concluding that different values of the zonal wind in the jet exit region over North America can modulate the response to ENSO. As in this study, they found that a weaker jet leads to a more poleward ENSO wave train.

Similarly, it has been shown that the position and intensity of the ENSO centre of action in the geopotential height at 500 hPa over the Pacific do not change with different mean states: this confirms the work of Tyrell and Karpechko (2021[110]), who found that changes in the model zonal wind bias do not affect the ENSO signal in the Aleutian Low.

Chapter 6

Conclusions

6.1 Summary of the main conclusions

This work aims at investigating the role of the mean atmospheric state, and in particular the North Pacific zonal flow mean state, in modulating the atmospheric response to ENSO and its impacts on temperature and total precipitation. A set of experiments is designed and realized in order to modify the mean state of the SPEEDY intermediate complexity general circulation model via progressively increasing or decreasing the height of the Rocky Mountains. Each experiment is forced with the same idealized ENSO SST anomaly. Finally, linear Rossby waves propagation theory is used to interpret the results. The following conclusions have been drawn:

- ROCK experiments proved that, by changing the height of the Rocky Mountains, the mean state of the model over the North Pacific sector changes as well. The speed of the Pacific jet changes in strength comparably to the zonal wind-speed bias of state-of-the-art global climate models. Pacific Jet indices computed for the CMIP6 models indicate that the ROCK experiments are able to mimic the bias in the Pacific jet strength of CMIP6 models.

- In the NINO and NINA experiments, the Rossby wave train in response to a tropical El-Niño-like and La Niña-like forcing is clearly affected by changes in the mean state. A stronger Pacific jet (i.e., when the Rocky Mountains height is reduced) corresponds to a geopotential height response center over Canada and Alaska shifted from north-west to south-east. Responses to the double intensity idealized El Niño and La Niña experiments are roughly the same as the regular intensity experiments.

- The observed sensitivity of the ENSO-induced Rossby wave train can be interpreted in terms of linear Rossby Wave propagation theory. Experiments with a stronger jet over the North Pacific are characterized by an average turning latitude, for wavenumbers from 3 to 5, located at lower latitudes than experiments with a weaker jet. The difference in the turning latitudes directly influences the direction of propagation of Rossby waves: experiments with a weaker jet show that the Rossby Wave train is shifted westward and northward, while experiments with a stronger jet tend to confine Rossby waves to lower latitudes.

6.2 Future perspectives

Several open questions concerning the role of the mean state in teleconnection remain. Some insights for future research are reported here:

- The altitude of the Rocky Mountains proved to be a good tuning parameter for the pacific jet speed, but there are other ways to change the mean flow. For example, different SST patterns may affect the mean climate. For instance, a good experiment could evaluate changes in the mean state on the North Atlantic Ocean altering the meridional gradient of the SST on the East coast of the North American continent. The idea is to alter the baroclinicity in the western North Atlantic and alter the storm track, inducing, in the end, a modulation of the Jet stream in the Atlantic. With different jets over the Atlantic Ocean it is possible to introduce an SST forcing like the Atlantic Multidecadal Variability (AMV) and see how the atlantic mean state affects the response to such anomalies.

- Biases in tropical convection are also contributing to biases in the Pacific jet. It would be useful to perform additional experiments that modify drastically the tropical Pacific convection. For example, a zonally symmetric climatological SST pattern (e.g. zonal mean) can be used to completely remove the Walker circulation and see how this influences the Pacific Jet properties. Then, the difference of the observed climatological SST with the zonally symmetric SST can be multiplied for an opportune coefficient. This SST field can be used as an anomaly to force the zonally symmetric SST pattern. In this way, by changing the value of the parameter it is possible to reintroduce the Walker circulation with different strengths. Coefficients from 0 to 1 represent a Walker circulation weaker than the climatological one, and values greater than 1 are for increased Walker circulation. Finally, the idealized El Niño (and La Niña) anomaly can be imposed to make experiments similar to the ENSO one.

- A third useful setup for a future work can consider the subgrid parameterization of orography. Several works explored the effect of parameterizations on the biases of the state-of-the-art general circulation models (Wallace et al., 1983[116]; Richter et al., 2010[90]; Sigmond and Scinocca, 2010[102]; Sandu et al., 2016[94]; Lindvall et al., 2017[**?**]; Van Niekerk et al.,2018[113]). These works separate the effects of the resolved orography from the subgrid parameterization. The results shows that, subgrid parameterization affects both the atmospheric zonal mean wind (Sandu et al.,2016[94]) as well as the stationary waves (Sandu et al., 2019[95]), and the effects are comparable, if not larger, with resolved orography. In recent years, the representation of such subgrid processes improved, although biases still exist (Sandu et al., 2019[95]). It would be of relevant scientific importance to understand how small changes in the parameterization can affect the atmospheric mean state. For example, it is possible to explore the role of orographic drag by changing the opportune parameterization. In SPEEDY the orographic drag parameterization consists of a single coefficient that can be easily changed.

The examples above are only a small portion of the possible experiments. Due to the complex nature of a GCM there are countless “tuning parameters” that can be used to modulate the mean state and the bias of the model. The SPEEDY model proved to be a good, fast and cheap test bed for performing this type of experiment.

Acronyms

AGCM Atmospheric General Circulation Model.

AJL Atlantic Jet Latitude.

AJS Atlantic Jet Strength.

AJW Atlantic Jet Width.

AMIP Atmospheric Model Intercomparison Project.

AMV Atlantic Multidecadal Variability.

CMIP Coupled Model Intercomparison Project.

D17 Dogar et al., 2017[38].

DECK Diagnostic Evaluation and Characterization of Klima experiments.

DJF December, January and February, winter season.

ECMWF European Centre for Medium-Range Weather Forecasts.

EMIC Earth system Model of Intermediate Complexity.

ENSO El Niño Southern Oscillation.

ERA ECMWF Re-Analysis.

FDR False discovery rate.

GCM General Circulation Model.

ICTP International Center for Theoretical Physics.

JFM January, February and March, Late winter season.

MSS MoiSt Static energy.

NINA Idealized La NIña experiments.

NINAx2 Double intensity idealized La Niña experiment.

NINO Idealized El Niño experiments.

NINOx2 Double intensity idealized El Niño intensity.

PBL Planetary Boundary Layer.

PJL Pacific Jet Latitude.

PJS Pacific Jet Strength.

PJW Pacific Jet Width.

PNA Pacific North America.

PV Potential Vorticity.

ROCK Modified orography experiments.

SIC Sea Ice Concentration.

SLP Sea Level Pressure.

SPEEDY Simplified Parameterization PrimitivE Equations DYnamics.

SST Sea Surface Temperature.

TCN Top of CoNvection.

WCRP World Climate Research Programme.

WPWP West Pacific Warm Pool.

Bibliography

[1] L. C. W. B . Clifrtatology. bernhard haurwitz and james m. austin. pp. xi + 410. map and plates. (new york and london: Mcgraw-hill company, inc. 1944.). *Quarterly Journal of the Royal Meteorological Society*, 71(309-310):443–444, 1945.

[2] C. Donald Ahrens. *Meteorology today : an introduction to weather, climate, and the environment*. Eighth edition. Belmont, CA : Thomson/Brooks/Cole, [2007] ©2007, [2007]. Includes bibliographical references (page R1-R2) and index.

[3] Michael Alexander and James Scott. The role of ekman ocean heat transport in the northern hemisphere response to enso. *Journal of Climate - J CLIMATE*, 21:5688–5707, 11 2008.

[4] Tércio Ambrizzi and Brian J Hoskins. Stationary rossby-wave propagation in a baroclinic atmosphere. *Quarterly Journal of the Royal Meteorological Society*, 123(540):919–928, 1997.

[5] Tércio Ambrizzi, Brian J. Hoskins, and Huang-Hsiung Hsu. Rossby wave propagation and teleconnection patterns in the austral winter. *Journal of Atmospheric Sciences*, 52(21):3661 – 3672, 1995.

[6] Javier Amezcua, Eugenia Kalnay, and Paul D. Williams. The effects of the raw filter on the climatology and forecast skill of the speedy model. *Monthly Weather Review*, 139(2):608 – 619, 2011.

[7] James A Anstey, Paolo Davini, Lesley J Gray, Tim J Woollings, Neal Butchart, Chiara Cagnazzo, Bo Christiansen, Steven C Hardiman, Scott M Osprey, and Shuting Yang. Multi-model analysis of northern hemisphere winter blocking: Model biases and the role of resolution. *Journal of Geophysical Research: Atmospheres*, 118(10):3956–3971, 2013.

[8] Akio Arakawa. Numerical simulation of large-scale atmospheric motions. *Numerical solution of field problems in continuum physics*, 2:24–40, 1970.

[9] J. Baldwin, A. Atwood, G. Vecchi, and D. Battisti. Outsize influence of central american orography on global climate. *AGU Adv.*, 2021.

[10] Rondrotiana Barimalala, Annalisa Bracco, and Fred Kucharski. The representation of the south tropical atlantic teleconnection to the indian ocean in the ar4 coupled models. *Climate dynamics*, 38(5-6):1147–1166, 2012.

[11] Marianna Benassi, Giovanni Conti, Silvio Gualdi, Paolo Ruggieri, Stefano Materia, Javier García-Serrano, Froila M. Palmeiro, Lauriane Batté, and Constantin Ardilouze. El niño teleconnection to the euro-mediterranean late-winter: the role of extratropical pacific modulation. *Climate Dynamics*, May 2021.

[12] Julie Berckmans, Tim Woollings, Marie-Estelle Demory, Pier-Luigi Vidale, and Malcolm Roberts. Atmospheric blocking in a high resolution climate model: influences of mean state, orography and eddy forcing. *Atmospheric Science Letters*, 14(1):34–40, 2013.

[13] J. BJERKNES. Atmospheric teleconnections from the equatorial pacific. *Monthly Weather Review*, 97(3):163 – 172, 1969.

[14] Ileana Bladé. The influence of midlatitude ocean–atmosphere coupling on the low-frequency variability of a gcm. part ii: Interannual variability induced by tropical sst forcing. *Journal of climate*, 12(1):21–45, 1999.

[15] Ileana Bladé, Matthew Newman, Michael A Alexander, and James D Scott. The late fall extratropical response to enso: Sensitivity to coupling and convection in the tropical west pacific. *Journal of climate*, 21(23):6101–6118, 2008.

[16] B. Bolin. On the influence of the earth's orography on the general character of the westerlies. *Tellus*, 2(3):184–195, 1950.

[17] William R. Boos and Zhiming Kuang. Dominant control of the south asian monsoon by orographic insulation versus plateau heating. *Nature*, 463(7278):218–222, Jan 2010.

[18] William Bourke. A multi-level spectral model. i. formulation and hemispheric integrations. *Monthly Weather Review*, 102(10):687–701, 1974.

[19] Annalisa Bracco, Fred Kucharski, Rameshan Kallummal, and Franco Molteni. Internal variability, external forcing and climate trends in multi-decadal agcm ensembles. *Climate Dynamics*, 23:659–678, 11 2004.

[20] Annalisa Bracco, Fred Kucharski, Franco Molteni, Wilco Hazeleger, and Camiel Severijns. A recipe for simulating the interannual variability of the asian summer monsoon and its relation with enso. *Climate Dynamics*, 28(5):441–460, Apr 2007.

[21] David James Brayshaw, Brian Hoskins, and Michael Blackburn. The basic ingredients of the north atlantic storm track. part i: Land–sea contrast and orography. *Journal of the Atmospheric Sciences*, 66(9):2539–2558, 2009.

[22] A. J. Broccoli and S. Manabe. The effects of orography on midlatitude northern hemisphere dry climates. *Journal of Climate*, 5(11):1181 – 1201, 1992.

[23] S. Brönnimann. Impact of el niño–southern oscillation on european climate. *Reviews of Geophysics*, 45(3), 2007.

[24] Ivana Herceg Bulić, Čedo Branković, and Fred Kucharski. Winter enso teleconnections in a warmer climate. *Climate dynamics*, 38(7):1593–1613, 2012.

[25] Edmund K. M. Chang. Diabatic and orographic forcing of northern winter stationary waves and storm tracks. *Journal of Climate*, 22(3):670 – 688, 2009.

[26] J. G. Charney. On a physical basis for numerical prediction of large-scale motions in the atmosphere. *Journal of Atmospheric Sciences*, 6(6):372 – 385, 1949.

[27] J. G. Charney and A. Eliassen. A numerical method for predicting the perturbations of the middle latitude westerlies. *Tellus*, 1(2):38–54, 1949.

[28] J. G. CHARNEY, R. FJÖRTOFT, and J. Von NEUMANN. Numerical integration of the barotropic vorticity equation. *Tellus*, 2(4):237–254, 1950.

[29] Jule G Charney and Philip G Drazin. Propagation of planetary-scale disturbances from the lower into the upper atmosphere. In *The Atmosphere—A Challenge*, pages 295–321. Springer, 1990.

[30] Hoffman H. N. Cheung and Wen Zhou. Implications of ural blocking for east asian winter climate in cmip5 gcms. part ii. *Journal of Climate*, 28(6):2217–2233, 2022/01/28/ 2015. Full publication date: 15 March 2015.

[31] John C.H. Chiang, Inez Y. Fung, Chi-Hua Wu, Yanjun Cai, Jacob P. Edman, Yuwei Liu, Jesse A. Day, Tripti Bhattacharya, Yugarshi Mondal, and Clothilde A. Labrousse. Role of seasonal transitions and westerly jets in east asian paleoclimate. *Quaternary Science Reviews*, 108:111–129, 2015.

[32] M. Claussen, L. Mysak, A. Weaver, M. Crucifix, T. Fichefet, M.-F. Loutre, S. Weber, J. Alcamo, V. Alexeev, A. Berger, R. Calov, A. Ganopolski, H. Goosse, G. Lohmann, F. Lunkeit, I. Mokhov, V. Petoukhov, P. Stone, and Z. Wang. Earth system models of intermediate complexity: closing the gap in the spectrum of climate system models. *Climate Dynamics*, 18(7):579–586, Mar 2002.

[33] National Research Council. *Carbon Dioxide and Climate: A Scientific Assessment*. The National Academies Press, Washington, DC, 1979.

[34] Curt Covey, Krishna Achutarao, Ulrich Cubasch, P. Jones, Steven Lambert, Michael Mann, Thomas Phillips, and Karl Taylor. An overview of results from the coupled model intercomparison project. *Global and Planetary Change*, 37:103–133, 06 2003.

[35] H.J. Critchfield. *General Climatology*. Prentice-Hall of India, 1979.

[36] Aiguo Dai and T. M. L. Wigley. Global patterns of enso-induced precipitation. *Geophysical Research Letters*, 27(9):1283–1286, 2000.

[37] D. P. Dee, S. M. Uppala, A. J. Simmons, P. Berrisford, P. Poli, S. Kobayashi, U. Andrae, M. A. Balmaseda, G. Balsamo, P. Bauer, P. Bechtold, A. C. M. Beljaars, L. van de Berg, J. Bidlot, N. Bormann, C. Delsol, R. Dragani, M. Fuentes, A. J. Geer, L. Haimberger, S. B. Healy, H. Hersbach, E. V. Hólm, L. Isaksen, P. Kållberg, M. Köhler, M. Matricardi, A. P. McNally, B. M. Monge-Sanz, J.-J. Morcrette, B.-K. Park, C. Peubey, P. de Rosnay, C. Tavolato, J.-N. Thépaut, and F. Vitart. The era-interim reanalysis: configuration and performance of the data assimilation system. *Quarterly Journal of the Royal Meteorological Society*, 137(656):553–597, 2011.

[38] Muhammad Mubashar Dogar, Fred Kucharski, and Syed Azharuddin. Study of the global and regional climatic impacts of enso magnitude using speedy agcm. *Journal of Earth System Science*, 126(2):30, Mar 2017.

[39] Carsten Eden, Richard J Greatbatch, and Claus W Böning. Adiabatically correcting an eddy-permitting model using large-scale hydrographic data: Application to the gulf stream and the north atlantic current. *Journal of Physical Oceanography*, 34(4):701–719, 2004.

[40] Bradley Efron and Robert J Tibshirani. *An introduction to the bootstrap*. CRC press, 1994.

[41] Arnt Eliassen. On the transfer of energy in stationary mountain waves. *Geophy. Publ.*, 22:1–23, 1960.

[42] V. Eyring, S. Bony, G. A. Meehl, C. A. Senior, B. Stevens, R. J. Stouffer, and K. E. Taylor. Overview of the coupled model intercomparison project phase 6 (cmip6) experimental design and organization. *Geoscientific Model Development*, 9(5):1937–1958, 2016.

[43] Juan Feng, Wen Chen, and Yanjie Li. Asymmetry of the winter extra-tropical teleconnections in the northern hemisphere associated with two types of enso. *Climate Dynamics*, 48(7):2135–2151, Apr 2017.

[44] W. Lawrence Gates, James S. Boyle, Curt Covey, Clyde G. Dease, Charles M. Doutriaux, Robert S. Drach, Michael Fiorino, Peter J. Gleckler, Justin J. Hnilo, Susan M. Marlais, Thomas J. Phillips, Gerald L. Potter, Benjamin D. Santer, Kenneth R. Sperber, Karl E. Taylor, and Dean N. Williams. An overview of the results of the atmospheric model intercomparison project (amip i). *Bulletin of the American Meteorological Society*, 80(1):29 – 56, 1999.

[45] Alexander Gershunov and Daniel R. Cayan. Heavy daily precipitation frequency over the contiguous united states: Sources of climatic variability and seasonal predictability. *Journal of Climate*, 16(16):2752 – 2765, 2003.

[46] Abdel Hannachi, Elizabeth A Barnes, and Tim Woollings. Behaviour of the winter north atlantic eddy-driven jet stream in the cmip3 integrations. *Climate dynamics*, 41(3-4):995–1007, 2013.

[47] J. Hansen, I. Fung, A. Lacis, D. Rind, S. Lebedeff, R. Ruedy, G. Russell, and P. Stone. Global climate changes as forecast by goddard institute for space studies three-dimensional model. *J. Geophys. Res.*, 93:9341–9364, 1988.

[48] J. Hansen, G. Russell, D. Rind, P. Stone, A. Lacis, S. Lebedeff, R. Ruedy, and L. Travis. Efficient three-dimensional global models for climate studies: Models i and ii. *Mon. Weather Rev.*, 111:609–662, 1983.

[49] Dennis L. Hartmann. Chapter 4 - the energy balance of the surface. In Dennis L. Hartmann, editor, *Global Physical Climatology (Second Edition)*, pages 95–130. Elsevier, Boston, second edition edition, 2016.

[50] B. J. Harvey, P. Cook, L. C. Shaffrey, and R. Schiemann. The response of the northern hemisphere storm tracks and jet streams to climate change in the cmip3, cmip5, and cmip6 climate models. *Journal of Geophysical Research: Atmospheres*, 125(23):e2020JD032701, 2020. e2020JD032701 2020JD032701.

[51] Isaac Held. Stationary and quasi-stationary eddies in the extratropical troposphere: theory. 01 2001.

[52] Isaac M. Held. The gap between simulation and understanding in climate modeling. *Bulletin of the American Meteorological Society*, 86(11):1609 – 1614, 2005.

[53] Isaac M. Held and Max J. Suarez. A proposal for the intercomparison of the dynamical cores of atmospheric general circulation models. *Bulletin of the American Meteorological Society*, 75(10):1825 – 1830, 1994.

[54] Isaac M. Held, Mingfang Ting, and Hailan Wang. Northern winter stationary waves: Theory and modeling. *Journal of Climate*, 15(16):2125 – 2144, 2002.

[55] Ivana Herceg-Bulić, Bianca Mezzina, Fred Kucharski, Paolo Ruggieri, and Martin P. King. Wintertime enso influence on late spring european climate: the stratospheric response and the role of north atlantic sst. *International Journal of Climatology*, 37(S1):87–108, 2017.

[56] Tomoyoshi Hirota, John W. Pomeroy, R. J. Granger, and Charles Maulé. An extension of the force-restore method to estimating soil temperature at depth and evaluation for frozen soils under snow. *Journal of Geophysical Research*, 107:4767, 2002.

[57] John D. Horel and John M. Wallace. Planetary-scale atmospheric phenomena associated with the southern oscillation. *Monthly Weather Review*, 109(4):813 – 829, 1981.

[58] Brian J Hoskins and Tercio Ambrizzi. Rossby wave propagation on a realistic longitudinally varying flow. *Journal of Atmospheric Sciences*, 50(12):1661–1671, 1993.

[59] Brian J Hoskins and David J Karoly. The steady linear response of a spherical atmosphere to thermal and orographic forcing. *Journal of Atmospheric Sciences*, 38(6):1179–1196, 1981.

[60] S. P. E. Keeley, R. T. Sutton, and L. C. Shaffrey. The impact of north atlantic sea surface temperature errors on the simulation of north atlantic european region climate. *Quarterly Journal of the Royal Meteorological Society*, 138(668):1774–1783, 2012.

[61] Charles D. Keeling. Is carbon dioxide from fossil fuel changing man's environment? *Proceedings of the American Philosophical Society*, 114(1):10–17, 2022/01/27/ 1970. Full publication date: Feb. 16, 1970.

[62] J. J. Kennedy, N. A. Rayner, R. O. Smith, D. E. Parker, and M. Saunby. Reassessing biases and other uncertainties in sea surface temperature observations measured in situ since 1850: 2. biases and homogenization. *Journal of Geophysical Research: Atmospheres*, 116(D14), 2011.

[63] M. P. King, C. Li, and S. Sobolowski. Resampling of enso teleconnections: accounting for cold-season evolution reduces uncertainty in the north atlantic. *Weather and Climate Dynamics*, 2(3):759–776, 2021.

[64] Martin P. King, Ivana Herceg-Bulić, Fred Kucharski, and Noel Keenlyside. Interannual tropical pacific sea surface temperature anomalies teleconnection to northern hemisphere atmosphere in november. *Climate Dynamics*, 50(5):1881–1899, Mar 2018.

[65] Martin P. King, Fred Kucharski, and Franco Molteni. The roles of external forcings and internal variabilities in the northern hemisphere atmospheric circulation change from the 1960s to the 1990s. *Journal of Climate*, 23(23):6200 – 6220, 2010.

[66] Wenwen Kong and John CH Chiang. Southward shift of westerlies intensifies the east asian early summer rainband following el niño. *Geophysical Research Letters*, 47(17):e2020GL088631, 2020.

[67] Fred Kucharski, A Bracco, JH Yoo, and F Molteni. Low-frequency variability of the indian monsoon–enso relationship and the tropical atlantic: The “weakening” of the 1980s and 1990s. *Journal of Climate*, 20(16):4255–4266, 2007.

[68] Fred Kucharski, Franco Molteni, and Annalisa Bracco. Decadal interactions between the western tropical pacific and the north atlantic oscillation. *Climate dynamics*, 26(1):79–91, 2006.

[69] Fred Kucharski, Franco Molteni, and Annalisa Bracco. Decadal interactions between the western tropical pacific and the north atlantic oscillation. *Climate Dynamics*, 26:79–91, 01 2006.

[70] Fred Kucharski, Ning Zeng, and Eugenia Kalnay. A further assessment of vegetation feedback on decadal sahel rainfall variability. *Climate dynamics*, 40(5-6):1453–1466, 2013.

[71] Ngar-Cheung Lau. Interactions between global sst anomalies and the midlatitude atmospheric circulation. *Bulletin of the American Meteorological Society*, 78(1):21–34, 1997.

[72] Ronald K. K. Li, Tim Woollings, Christopher O’Reilly, and Adam A. Scaife. Effect of the North Pacific Tropospheric Waveguide on the Fidelity of Model El Niño Teleconnections. *Journal of Climate*, 33(12):5223–5237, June 2020.

[73] Hosmay Lopez and Ben P. Kirtman. Enso influence over the pacific north american sector: uncertainty due to atmospheric internal variability. *Climate Dynamics*, 52(9):6149–6172, May 2019.

[74] Syukuro Manabe and Kirk Bryan. Climate calculations with a combined ocean-atmosphere model. *Journal of Atmospheric Sciences*, 26(4):786 – 789, 1969.

[75] SYUKURO MANABE, JOSEPH SMAGORINSKY, and ROBERT F. STRICKLER. Simulated climatology of a general circulation model with a hydrologic cycle. *Monthly Weather Review*, 93(12):769 – 798, 1965.

[76] Syukuro Manabe and Theodore B. Terpstra. The effects of mountains on the general circulation of the atmosphere as identified by numerical experiments. *Journal of Atmospheric Sciences*, 31(1):3 – 42, 1974.

[77] Julia V Manganello and Bohua Huang. The influence of systematic errors in the southeast pacific on enso variability and prediction in a coupled gcm. *Climate Dynamics*, 32(7):1015–1034, 2009.

[78] Iris Manola, Frank Selten, Hylke de Vries, and Wilco Hazeleger. “waveguidability” of idealized jets. *Journal of Geophysical Research: Atmospheres*, 118(18):10,432–10,440, 2013.

[79] Bianca Mezzina, Javier García-Serrano, Ileana Bladé, and Fred Kucharski. Dynamics of the enso teleconnection and nao variability in the north atlantic–european late winter. *Journal of Climate*, 33(3):907 – 923, 2020.

[80] Yale Mintz. Very long-term global integration of the primitive equations of atmospheric motion : An experiment in climate simulation. 1968.

[81] F. Molteni. Atmospheric simulations using a gcm with simplified physical parametrizations. i: model climatology and variability in multi-decadal experiments. *Climate Dynamics*, 20(2):175–191, Jan 2003.

[82] Franco Molteni, Laura Ferranti, TN Palmer, and Pedro Viterbo. A dynamical interpretation of the global response to equatorial pacific sst anomalies. *Journal of climate*, 6(5):777–795, 1993.

[83] Franco Molteni, Martin P King, Fred Kucharski, and David M Straus. Planetary-scale variability in the northern winter and the impact of land–sea thermal contrast. *Climate dynamics*, 37(1-2):151–170, 2011.

[84] S. Nigam and E. DeWeaver. Dynamical meteorology | stationary waves (orographic and thermally forced). In Gerald R. North, John Pyle, and Fuqing Zhang, editors, *Encyclopedia of Atmospheric Sciences (Second Edition)*, pages 431–445. Academic Press, Oxford, second edition edition, 2015.

[85] E. G. Nisbet. Philander s. g. 1990. el niño, la niña, and the southern oscillation. ix 293 pp. san diego, new york, berkeley, boston, london, sydney, tokyo, toronto: Academic press (harcourt brace jovanovich). price £42.50 (hard covers). isbn 0 12 553235 0. international geophysics series vol. 46. *Geological Magazine*, 127(5):478–478, 1990.

[86] Timothy N Palmer. A nonlinear dynamical perspective on climate prediction. *Journal of Climate*, 12(2):575–591, 1999.

[87] Norman A Phillips. The general circulation of the atmosphere: A numerical experiment. *Quarterly Journal of the Royal Meteorological Society*, 82(352):123–164, 1956.

[88] David A Randall, Richard A Wood, Sandrine Bony, Robert Colman, Thierry Fichefet, John Fyfe, Vladimir Kattsov, Andrew Pitman, Jagadish Shukla, Jayaraman Srinivasan, et al. Climate models and their evaluation. In *Climate change 2007: The physical science basis. Contribution of Working Group I to the Fourth Assessment Report of the IPCC (FAR)*, pages 589–662. Cambridge University Press, 2007.

[89] Ingo Richter, Swadhin K Behera, Takeshi Doi, Bunmei Taguchi, Yukio Masumoto, and Shang-Ping Xie. What controls equatorial atlantic winds in boreal spring? *Climate dynamics*, 43(11):3091–3104, 2014.

[90] Jadwiga H. Richter, Fabrizio Sassi, and Rolando R. Garcia. Toward a physically based gravity wave source parameterization in a general circulation model. *Journal of the Atmospheric Sciences*, 67(1):136 – 156, 2010.

[91] Andre J. Robert. The integration of a low order spectral form of the primitive meteorological equations. *Journal of the Meteorological Society of Japan. Ser. II*, 44(5):237–245, 1966.

[92] Belén Rodríguez-Fonseca, Irene Polo, Javier García-Serrano, Teresa Losada, Elsa Mohino, Carlos Roberto Mechoso, and Fred Kucharski. Are atlantic niños enhancing pacific enso events in recent decades? *Geophysical Research Letters*, 36(20), 2009.

[93] P Ruggieri, F Kucharski, R Buizza, and MHP Ambaum. The transient atmospheric response to a reduction of sea-ice cover in the barents and kara seas. *Quarterly Journal of the Royal Meteorological Society*, 143(704):1632–1640, 2017.

[94] Irina Sandu, Peter Bechtold, Anton Beljaars, Alessio Bozzo, Felix Pithan, Theodore G. Shepherd, and Ayrton Zadra. Impacts of parameterized orographic drag on the northern hemisphere winter circulation. *Journal of advances in modeling earth systems*, 8(1):196–211, Mar 2016. 27668040[pmid].

[95] Irina Sandu, Annelize van Niekerk, Theodore G. Shepherd, Simon B. Vosper, Ayrton Zadra, Julio Bacmeister, Anton Beljaars, Andrew R. Brown, Andreas Dörnbrack, Norman McFarlane, Felix Pithan, and Gunilla Svensson. Impacts of orography on large-scale atmospheric circulation. *npj Climate and Atmospheric Science*, 2(1):10, May 2019.

[96] Adam A. Scaife, Ruth E. Comer, Nick J. Dunstone, Jeff R. Knight, Doug M. Smith, Craig MacLachlan, Nicola Martin, K. Andrew Peterson, Dan Rowlands, Edward B. Carroll, Stephen Belcher, and Julia Slingo. Tropical rainfall, rossby waves and regional winter climate predictions. *Quarterly Journal of the Royal Meteorological Society*, 143(702):1–11, 2017.

[97] R. Seager, D. S. Battisti, J. Yin, N. Gordon, N. Naik, A. C. Clement, and M. A. Cane. Is the gulf stream responsible for europe's mild winters? *Quarterly Journal of the Royal Meteorological Society*, 128(586):2563–2586, 2002.

[98] Rich Seager, Nili Harnik, WA Robinson, Yochanan Kushnir, Mingfang Ting, H-P Huang, and Jennifer Velez. Mechanisms of enso-forcing of hemispherically symmetric precipitation variability. *Quarterly Journal of the Royal Meteorological Society: A journal of the atmospheric sciences, applied meteorology and physical oceanography*, 131(608):1501–1527, 2005.

[99] Richard Seager, Yochanan Kushnir, Celine Herweijer, Naomi Naik, and Jennifer Velez. Modeling of tropical forcing of persistent droughts and pluvials over western north america: 1856–2000. *Journal of Climate*, 18(19):4065 – 4088, 2005.

[100] L. C. Shaffrey, I. Stevens, W. A. Norton, M. J. Roberts, P. L. Vidale, J. D. Harle, A. Jrrar, D. P. Stevens, M. J. Woodage, M. E. Demory, J. Donners, D. B. Clark, A. Clayton, J. W. Cole, S. S. Wilson, W. M. Connolley, T. M. Davies, A. M. Iwi, T. C. Johns, J. C. King, A. L. New, J. M. Slingo, A. Slingo, L. Steenman-Clark, and G. M. Martin. U.k. higem: The new u.k. high-resolution global environment model—model description and basic evaluation. *Journal of Climate*, 22(8):1861 – 1896, 2009.

[101] Danian Shi, Wenjin Zhao, Simon L Klemperer, Zhenhan Wu, James Mechie, Jianyu Shi, Guangqi Xue, and Heping Su. West–east transition from underplating to steep subduction in the india–tibet collision zone revealed by receiver-function profiles. *Earth and Planetary Science Letters*, 452:171–177, 2016.

[102] Michael Sigmond and John F. Scinocca. The influence of the basic state on the northern hemisphere circulation response to climate change. *Journal of Climate*, 23(6):1434 – 1446, 2010.

[103] JOSEPH SMAGORINSKY, SYUKURO MANABE, and J. LEITH HOLLOWAY. Numerical results from a nine-level general circulation model of the atmosphere. *Monthly Weather Review*, 93(12):727 – 768, 1965.

[104] David M. Straus and J. Shukla. Does enso force the pna? *Journal of Climate*, 15(17):2340 – 2358, 2002.

[105] Robert J Tibshirani and Bradley Efron. An introduction to the bootstrap. *Monographs on statistics and applied probability*, 57:1–436, 1993.

[106] M. Tiedtke. Representation of clouds in large-scale models. *Monthly Weather Review*, 121(11):3040 – 3061, 1993.

[107] Axel Timmermann, Soon-Il An, Jong-Seong Kug, Fei-Fei Jin, Wenju Cai, Antonietta Capotondi, Kim M. Cobb, Matthieu Lengaigne, Michael J. McPhaden, Malte F. Stuecker, Karl Stein, Andrew T. Wittenberg, Kyung-Sook Yun, Tobias Bayr, Han-Ching Chen, Yoshimitsu Chikamoto, Boris Dewitte, Dietmar Dommenget, Pamela Grothe, Eric Guilyardi, Yoo-Geun Ham, Michiya Hayashi, Sarah Ineson, Daehyun Kang, Sunyong Kim, WonMoo Kim, June-Yi Lee, Tim Li, Jing-Jia Luo, Shayne McGregor, Yann Planton, Scott Power, Harun Rashid, Hong-Li Ren, Agus Santoso, Ken Takahashi, Alexander Todd, Guomin Wang, Guojian Wang, Ruihuang Xie, Woo-Hyun Yang, Sang-Wook Yeh, Jinho Yoon, Elke Zeller, and Xuebin Zhang. El niño–southern oscillation complexity. *Nature*, 559(7715):535–545, Jul 2018.

[108] Kevin E. Trenberth. The definition of el niño. *Bulletin of the American Meteorological Society*, 78(12):2771 – 2778, 1997.

[109] G. Trewartha and L.H. Horn. *An Introduction to Climate*. McGraw-Hill series in geography. McGraw-Hill, 1971.

[110] N. L. Tyrrell and A. Yu. Karpechko. Minimal impact of model biases on northern hemisphere el niño–southern oscillation teleconnections. *Weather and Climate Dynamics*, 2(3):913–925, 2021.

[111] Uwe Ulbrich, Gregor C Leckebusch, and Joaquim G Pinto. Extra-tropical cyclones in the present and future climate: a review. *Theoretical and Applied Climatology*, 96(1):117–131, 2009.

[112] Paul J. Valdes and Brian J. Hoskins. Linear stationary wave simulations of the time-mean climatological flow. *Journal of Atmospheric Sciences*, 46(16):2509 – 2527, 1989.

[113] Annelize van Niekerk, Irina Sandu, and Simon B. Vosper. The circulation response to resolved versus parametrized orographic drag over complex mountain terrains. *Journal of Advances in Modeling Earth Systems*, 10(10):2527–2547, 2018.

[114] Pedro Viterbo and Anton C. M. Beljaars. An improved land surface parameterization scheme in the ecmwf model and its validation. *Journal of Climate*, 8(11):2716 – 2748, 1995.

[115] John M. Wallace and David S. Gutzler. Teleconnections in the geopotential height field during the northern hemisphere winter. *Monthly Weather Review*, 109(4):784 – 812, 1981.

[116] John M. Wallace, Stefano Tibaldi, and Adrian J. Simmons. Reduction of systematic forecast errors in the ecmwf model through the introduction of an envelope orography. *Quarterly Journal of the Royal Meteorological Society*, 109(462):683–717, 1983.

[117] Chunzai Wang, Clara Deser, Jin-Yi Yu, Pedro DiNezio, and Amy Clement. *El Niño and Southern Oscillation (ENSO): A Review*, pages 85–106. Springer Netherlands, Dordrecht, 2017.

[118] Darryn W. Waugh and Lorenzo M. Polvani. *Stratospheric Polar Vortices*, pages 43–57. American Geophysical Union (AGU), 2010.

[119] R. H. White, D. S. Battisti, and G. H. Roe. Mongolian mountains matter most: Impacts of the latitude and height of asian orography on pacific wintertime atmospheric circulation. *J. Climate*, 30:4065–4082, 2017.

[120] R. H. White, D. S. Battisti, and A. Sheshadri. Orography and the boreal winter stratosphere: The importance of the mongolian mountains. *Geophys. Res. Lett.*, 45:2088–2096, 2018.

[121] RH White, JM Wallace, and DS Battisti. Revisiting the role of mountains in the northern hemisphere winter atmospheric circulation. *Journal of the Atmospheric Sciences*, 2021.

[122] T. M. L. Wigley and M. E. Schlesinger. Analytical solution for the effect of increasing co2 on global mean temperature. *Nature*, 315(6021):649–652, Jun 1985.

[123] D. S. Wilks. On “field significance” and the false discovery rate. *Journal of Applied Meteorology and Climatology*, 45(9):1181 – 1189, 2006.

[124] Robert C. Wills and Tapio Schneider. Stationary eddies and the zonal asymmetry of net precipitation and ocean freshwater forcing. *Journal of Climate*, 28(13):5115 – 5133, 2015.

[125] Tim Woollings, Abdel Hannachi, and Brian Hoskins. Variability of the north atlantic eddy-driven jet stream. *Quarterly Journal of the Royal Meteorological Society*, 136(649):856–868, 2010.

[126] Giuseppe Zappa, Len C. Shaffrey, Kevin I. Hodges, Phil G. Sansom, and David B. Stephenson. A multimodel assessment of future projections of north atlantic and european extratropical cyclones in the cmip5 climate models. *Journal of Climate*, 26(16):5846 – 5862, 2013.

[127] Stephen E. Zebiak and Mark A. Cane. A model el nintilde–southern oscillation. *Monthly Weather Review*, 115(10):2262 – 2278, 1987.